Updated DIRAC spectrometer at CERN PS : of ππ and πK atoms

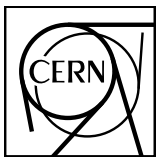

CERN-PH-EP-2015-147
12 June 2015

B. Adeva [a], L. Afanasyev [b], Y. Allkofer [c], C. Amsler [d], A. Anani
V. Brekhovskikh [g], Gh. Caragheorgheopol [f], T. Cechak [h], M. Ch
Ciocarlan [f], S. Constantinescu [f], C. Detraz [j], P. Doskarova [h], D. Drijard [j], A. Dudarev [b], M.
Duma [f], D. Dumitriu [f], D. Fluerasu [f], A. Gorin [g], O. Gorchakov [b], K. Gritsay [b], C. Guaraldo [k], M.
Gugiu [f], M. Hansroul [j], Z. Hons [l], S. Horikawa [c], Y. Iwashita [m], V. Karpukhin [b], J. Kluson [h],
M. Kobayashi [n], V. Kruglov [b], L. Kruglova [b], A. Kulikov [b], E. Kulish [b], A. Kuptsov [b],
A. Lamberto [e], A. Lanaro [o], R. Lednicky [p], C. Mariñas [a], J. Martincik [h], L. Nemenov [b,j],
M. Nikitin [b], K. Okada [q], V. Olchevskii [b], M. Pentia [f], A. Penzo [r], M. Plo [a], P. Prusa [h],
G. F. Rappazzo [e], A. Romero Vidal [k], A. Ryazantsev [g], V. Rykalin [g], J. Saborido [a], J. Schacher [d],
A. Sidorov [g], J. Smolik [h], F. Takeutchi [q], L. Tauscher [s], T. Trojek [h], S. Trusov [t],
O. Ullaland [j], T. Urban [h], T. Vrba [h], V. Yazkov [t], Y. Yoshimura [n], M. Zhabitsky [b], P. Zrelov [b]

[a] *Santiago de Compostela University, Spain*
[b] *JINR, Dubna, Russia*
[c] *Zurich University, Switzerland*
[d] *Albert Einstein Center for Fundamental Physics, Laboratory of High Energy Physics, Bern, Switzerland*
[e] *INFN, Sezione di Trieste and Messina University, Messina, Italy*
[f] *IFIN-HH, National Institute for Physics and Nuclear Engineering, Bucharest, Romania*
[g] *IHEP, Protvino, Russia*
[h] *Czech Technical University in Prague, Czech Republic*
[i] *Tokyo Metropolitan University, Japan*
[j] *CERN, Geneva, Switzerland*
[k] *INFN, Laboratori Nazionali di Frascati, Frascati, Italy*
[l] *Nuclear Physics Institute ASCR, Rez, Czech Republic*
[m] *Kyoto University, Kyoto, Japan*
[n] *KEK, Tsukuba, Japan*
[o] *University of Wisconsin, Madison, USA*
[p] *Institute of Physics ASCR, Prague, Czech Republic*
[q] *Kyoto Sangyo University, Kyoto, Japan*
[r] *INFN, Sezione di Trieste, Trieste, Italy*
[s] *Basel University, Switzerland*
[t] *Skobeltsin Institute for Nuclear Physics of Moscow State University, Moscow, Russia*

Abstract

The DIRAC spectrometer installed at CERN PS was redesigned and upgraded in order to study simultaneously $A_{\pi\pi}$ and $A_{\pi K}$ atoms, namely the bound states of $\pi^+\pi^-$, and π^+K^-, π^-K^+ mesons. The detector system which is able to accept a high intensity beam such as 2 - 6 × 10^{11} primary protons per second, the electronics and the data-acquisition system adapted to handle very large amount of data actually allowed to identify successfully π, K, p, e and μ and to give the possibility to select π-π and π-K pairs in the off-line analysis. The setup's capability of giving a high resolution in the reconstruction of the relative momentum in the pair-CMS Q gave the possibility to analyze the distributions of its components, in order to identify the signal from pairs originating from hadronic atoms, and to measure their lifetimes in the ground state and π-π and π-K s-wave scattering lengths. The setup also allowed to study long-lived excited states of π-π atoms.

1. Introduction

The objective of the DIRAC experiment at the CERN Proton Synchrotron was a study of the hydrogen-like atom pionium formed by π^+ and π^- mesons ($A_{2\pi}$). The second stage of this experiment, whose experimental setup is reported in detail in this article, aims at a further study of a new hadronic atom formed by π^+K^- and π^-K^+ meson pairs ($A_{\pi K}$) [ADE03A] in addition to the continued study of $A_{2\pi}$.

The aim of the experiment is to measure the lifetimes of these hadronic atoms, which are determined by the charge exchange amplitude $\pi^+\pi^- \to \pi^0\pi^0$ and $\pi^+K^-, \pi^-K^+ \to \pi^0\overline{K}^0$ very close to the threshold. The precise measurement of $A_{2\pi}$ and $A_{\pi K}$ lifetimes will enable to determine the combination of s-wave pion-pion $|a_0 - a_2|$ and pion-kaon $|a_{1/2} - a_{3/2}|$ scattering lengths (with isospin 0, 2 and 1/2, 3/2, respectively) in a model-independent way. The scattering lengths are evaluated in the framework of QCD with the effective Lagrangians of Chiral Perturbation Theory (ChPT). So the lifetime measurements would provide a crucial test for the understanding of chiral symmetry breaking in QCD including processes with strange quarks.

The study of $A_{2\pi}$ includes also the observation of the long-live states of this atom (metastable states with nonzero orbital momentum) aiming at studying a possibility to measure the energy splitting (Lamb shift; of the order of 0.5 eV) between ns and np states of pionium. This observation will open a possibility to measure another combination of pion scattering lengths $2a_0 + a_2$ and thus to get both lengths separately in a model-independent way.

Hadronic atoms $A_{2\pi}$ and $A_{\pi K}$ are produced in proton–nucleus interactions at 24 GeV. After production, these relativistic atoms may either decay due to the strong interaction into a pair of neutral mesons or interact electromagnetically with the target material and finally break-up (be ionized) into the characteristic charged meson pairs (''atomic'' pairs) available for detection. These pairs have a low relative momentum in their centre of mass system ($Q < 3$ MeV/c) and a very small opening angle (< 3 mrad) The lifetime measurement is sensitive to the target material, and a Nickel foil of 100 μm was selected [ADE03A]. The choice of such a foil was also dictated by the needs to minimize the multiple scattering in the target and thus to provide a good resolution of the magnetic spectrometer, as good as about 0.5 MeV/c in terms of relative momentum of the split up pairs. This is essential in order to be able to detect the ''atomic'' pair signal superimposed over the substantial background of ''free'' pairs produced in inclusive proton–nucleus interactions.

At the first stage of the experiment in 2001-2003 about 21200 events of pionium breakup have been identified. The most precise value of the $\pi^+\pi^-$ atom lifetime has been measured as

$$\tau = \left(3.15^{+0.20}_{-0.19}\Big|_{\text{stat}}\ ^{+0.20}_{-0.18}\Big|_{\text{syst}}\right)\times 10^{-15}\,\text{s}.$$

From this value, the difference of s-wave ππ scattering lengths with isospin 0 and 2 has been extracted as [ADE11]:

$$|a_0 - a_2| = \left(0.2533\ ^{+0.0080}_{-0.0078}\Big|_{\text{stat}}\ ^{+0.0078}_{-0.0073}\Big|_{\text{syst}}\right) M_{\pi^+}^{-1}$$

In 2008 – 2010, the statistics has been enriched, more than doubled, to confirm the above results. It gave us the possibility to reduce the statistical uncertainty from 3.1% to 2.2%, and the total uncertainty including systematic errors from 4.3% to 3.0%.

Data have been taken for πK atomic pairs since 2007. The results of the analysis of these data will become available soon. A preliminary lifetime of

$$\tau = \left(2.5\,^{+3.0}_{-1.8}\right) \times 10^{-15}\ s$$

has been already reported [ADE14].

Also the result of the attempted observation of the $A_{\pi\pi}$ excited state is now under investigation and will be published soon.

2. General layout and the principal updates

The DIRAC setup [ADE03B] was originally designed to detect $\pi^+\pi^-$ pairs with small relative momenta. It was a double arm magnetic spectrometer with two identical arms symmetrically located with respect to the secondary particle beam. It became operational in 1998.

In order to observe $A_{\pi K}$ (of both signs) in addition, and yet to continue the measurement of $A_{2\pi}$ lifetime, the detector setup was upgraded. The setup, sometimes called DIRAC II, retains the symmetric geometry.

In this paper, the modifications are mainly discussed. The readers are invited to refer to the previous paper [ADE03B] to find the detail about the "unchanged" or rather "common" parts of the spectrometer. The upgraded DIRAC setup [KUP09] became ready in the end of 2006 and has been collecting data since 2007.

The isometric view of the new setup is shown in Fig. 2.1. A scheme of the setup with typical trajectories for π^+K^- and π^-K^+ from $A_{\pi K}$ breakup is shown in Fig. 2.2. Since the momenta of the two mesons originating from the breakup of the πK-atoms are very small in their center-of-mass system, they have similar velocities in the laboratory system, and hence kaons are less deflected than pions.

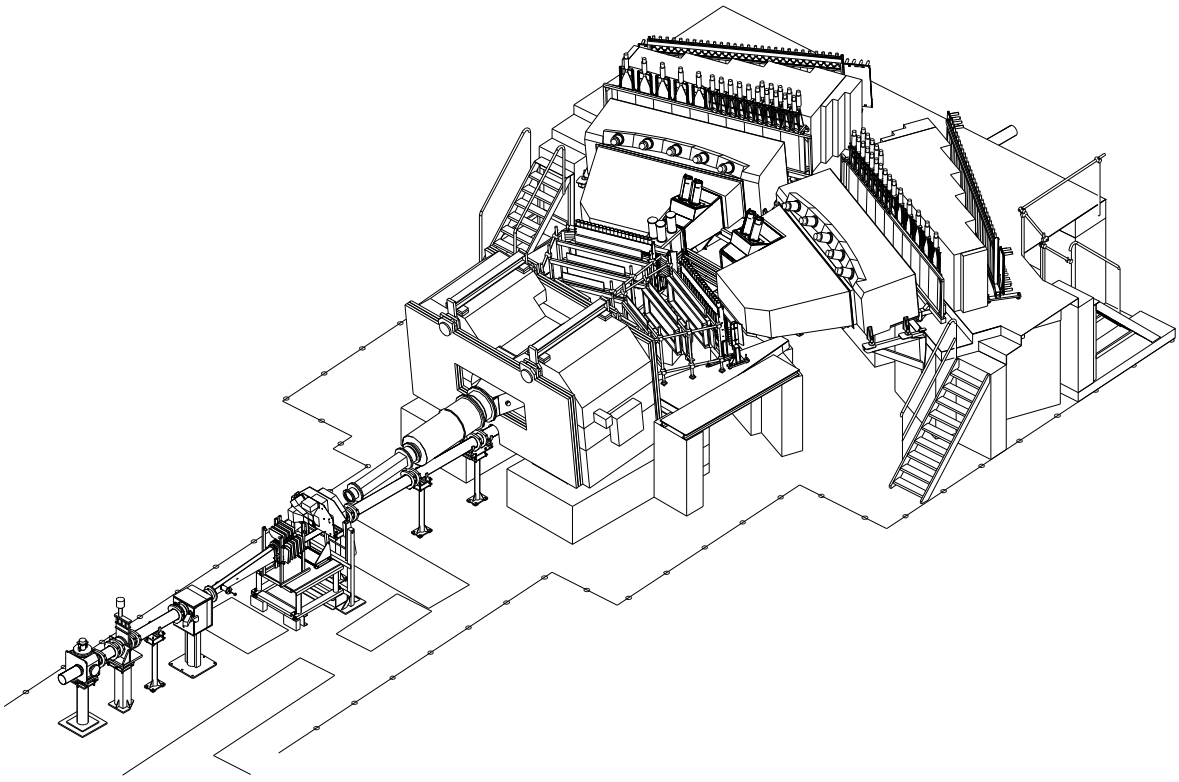

Fig. 2.1 Isometric view of the new setup. The contour on the floor with marks of 1 m is the external radiation shielding. The internal contours are marks of the local shieldings.

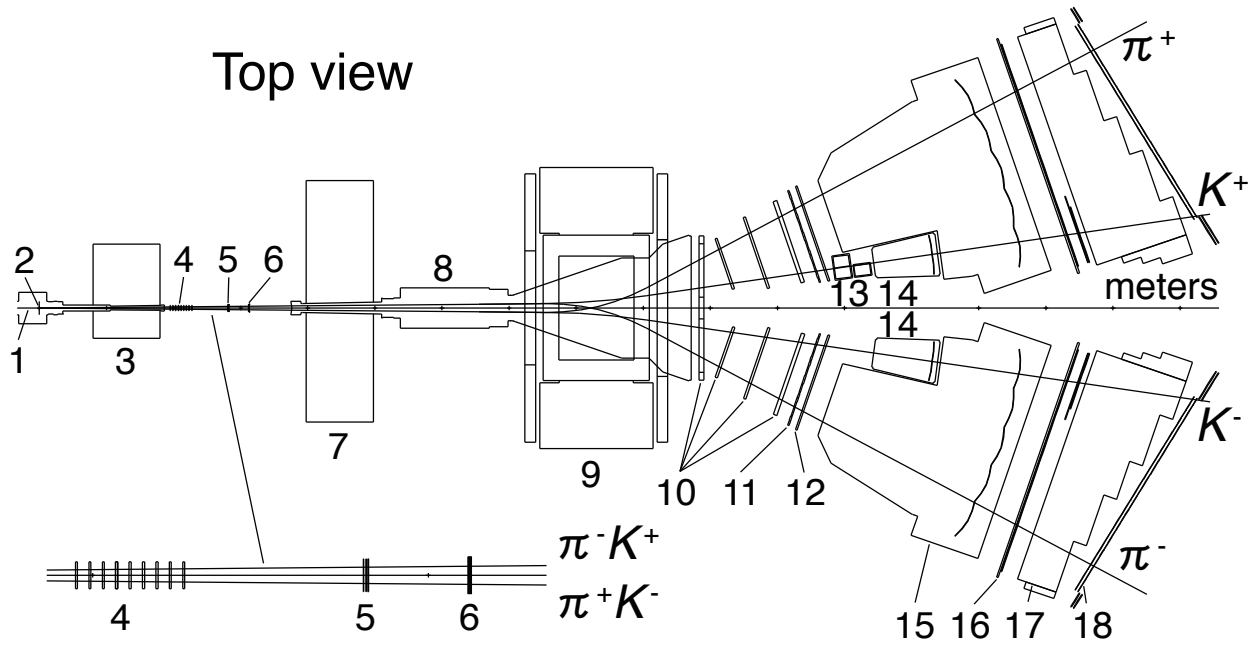

Fig. 2.2 Scheme of the updated two-arm spectrometer (top view). 1– proton beam, 2– target, 3– shield, 4– microdrift chambers, 5– scintillation fiber detector, 6– scintillation ionization hodoscope, 7– shield, 8– vacuum, 9– spectrometer magnet, 10– drift chambers, 11– vertical scintillation hodoscopes, 12– horizontal scintillation hodoscopes, 13– aerogel Cerenkov detectors, 14– C4F10 Cerenkov detectors, 15– N_2 Cerenkov detectors, 16– preshowers, 17– absorbers, 18– muon scintillation hodoscopes. The solid lines crossing the spectrometer arms correspond to typical $\pi^{\pm}$-and $K^{\pm}$-trajectories from the ionization of πK-atoms in the production target.

In order to detect π^+K^- "atomic" pairs one needs to discriminate pions from kaons in the negative arm. The detection of π^-K^+ pairs is more complex as in this case, in addition to π^+, a large admixture of protons to positive kaons is also expected. The implementation of new detectors and trigger schemes should not, however, affect the detection efficiency of $\pi^+\pi^-$ atomic pairs, as this class of events still constitutes the bulk of the collected data.

The setup upgrading includes:

- *Additional iron shielding (Fig. 2.2 shield 3) near the target station with collimators for the primary and secondary beams instead of using a wide tube common to both beams. The existing iron shielding, close to the spectrometer magnet, which determines the aperture of the secondary beam was kept unchanged (shield 7 in Fig. 2.2). The additional shielding allows essentially to decrease the background counting rates of upstream detectors by a factor of 1.08.*
- *A new detector - Microdrift Chambers (MDC) – installed in the air gap of the secondary particle channel in place of the Microstrip Gas Chambers (MSGC). The MDC measures particle coordinates using 18 identical planes: X, Y and U. The sensitive area of the MDC is close to 80 × 80 mm² and the space resolution for single hits is about 40 μm.*
- *The SFD new detector with the fiber diameter of 0.28 mm instead of 0.5 mm in the original detector was implemented for X and Y projections.*
- *The front-end electronics for the existing Drift Chambers (DC) downstream of the spectrometer magnet was modified to decrease the threshold and, consequently, to decrease the high voltage. This allowed working at higher intensities with a high efficiency.*

- *Aerogel Cerenkov counters were installed in the left arm of the downstream detectors for kaon and proton separation.*
- *New gas Cerenkov detectors were installed in both arms of the spectrometer for pion and kaon separation. These counters are filled with a heavy gas - perfluorobutane (C4F10). The existing gas Cerenkov counters filled with nitrogen (N_2) have been modified and are still used for electron suppression.*
- *New scintillation counters were installed in both arms. The existing Vertical Hodoscopes (VH) were extended. The Horizontal Hodoscope (HH) and Preshowers (PSh) were produced from scratch. The modification of the counters allows an increase of the setup aperture and essentially increases the $A_{\pi K}$ detection efficiency.*
- *A new front-end electronics with dedicated data transfer system was implemented for SFD. The new electronics allows to measure time and amplitude for every SFD column. As a result the SFD efficiency was increased up to 98% and a close hit separation became much better. Such electronics was implemented also to IH, VH, HH, and all Cerenkov detectors.*

In contrast to the $\pi^+\pi^-$ pairs, the π^+K^- and π^-K^+ pairs from $A_{\pi K}$ breakup have momenta that differ by a factor 3.5. Only $A_{\pi K}$ with momenta higher than 5.2 GeV/c break up into πK pairs entering the apparatus acceptance. The pions from $A_{\pi K}$ pairs have a momentum range 1.15 ~ 2.7 GeV/c, whereas the kaons have momenta between 4.05 and 9.6 GeV/c. The simulated topology of π^-K^+ pairs from $A_{\pi K}$ breakup is shown in Fig. 2.3. The kaon trajectories are close to the setup symmetry axis, whereas the correlated pions are away from the axis. kaons from π^-K^+ atoms are detectable in the K^+ momentum range from 3.9 to 8.9 GeV/c when the atoms are emitted along the left side of the collimator. When the π^-K^+ atoms are emitted along the setup symmetry axis, the kaons pass at the edge of detectors (the momenta 4.5 – 5 GeV/c). For π^+K^- atoms the particle trajectories are mirrored relative to the symmetry axis (proton beam). Such topology dictates the geometry of the Cerenkov detectors used for the particle identification.

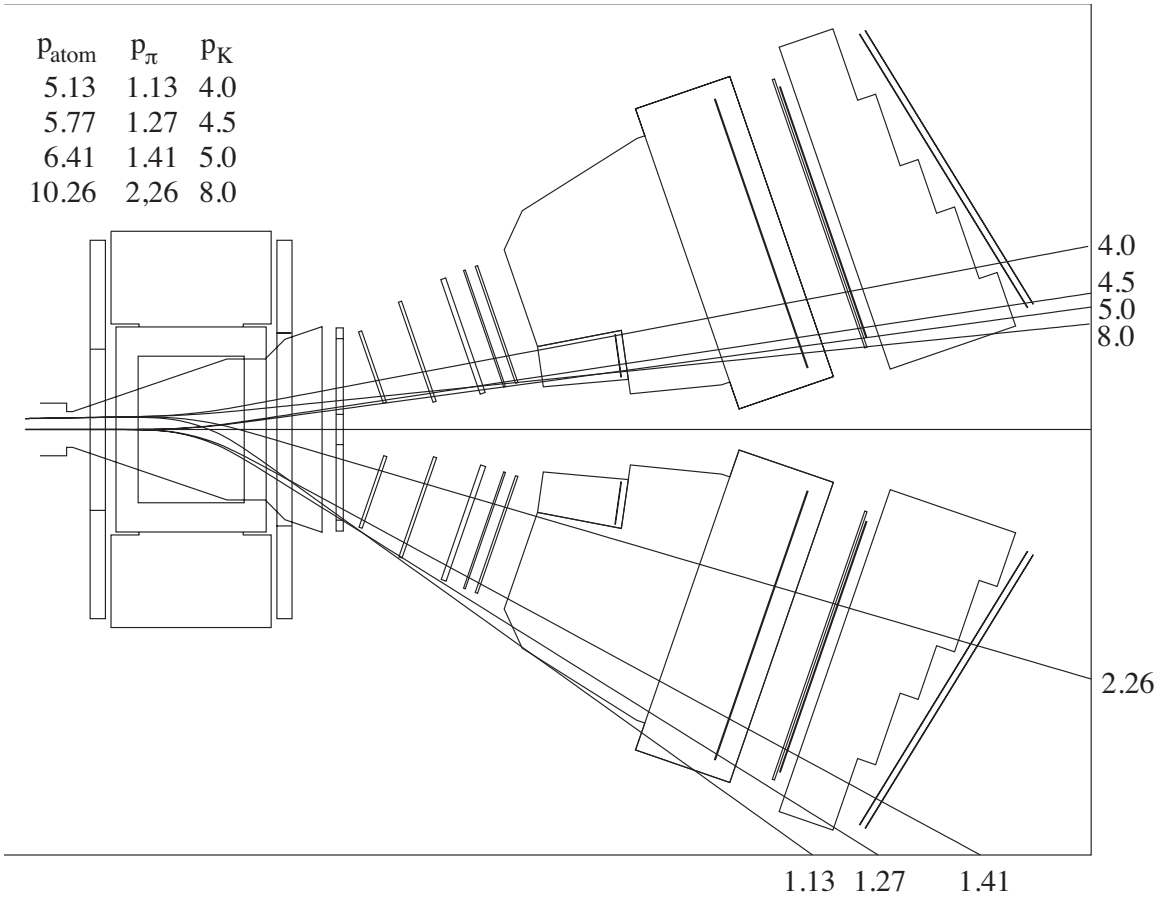

Fig. 2.3 Trajectories of π^- and K^+ from the $A_{\pi-K+}$ breakup. The numbers on the trajectory lines are the π^- and K^+ momenta in GeV/*c*. The $A_{\pi+K-}$, π^- and K^+ momenta are shown in the table in the left upper corner.

The top view of the updated experimental setup is shown in Fig. 2.2. The set-up consists of the proton beam line, target station, secondary particle vacuum channel, spectrometer magnet and detectors placed upstream and downstream the analyzing magnet. Free particles and atomic pairs produced in the target enter the secondary particle channel which is tilted upwards by 5.7° with respect to the proton beam (Fig. 2.1). The spectrometer magnet, together with all the downstream detectors, is installed at the end of the secondary particle channel and also tilted by 5.7°.

The upstream section of the secondary particle channel between the target station and the spectrometer magnet is instrumented with the following detectors: Microdrift Chambers (MDC), scintillating fibre detector (SFD) and scintillation ionization hodoscope (IH). Downstream the spectrometer magnet, the set-up splits into two quasi-identical arms for detection and identification of positive and negative charged particles. The angle between each arm and the spectrometer symmetry axis is 19 degrees. The following detectors are located along each arm: drift chamber system (DC), vertical scintillation hodoscope (VH), horizontal scintillation hodoscope (HH), gas Cerenkov counters with heavy gas (C2F10) and nitrogen (N_2), preshower detector (PSh) and muon detector (MU). The aerogel Cerenkov counters is installed in the positive arm only.

The atoms in metastable state are also observed in the DIRAC setup with a small change in the setup and the results can demonstrate the feasibility of Lamb shift ($E_n^s - E_n^p$) measurement. For that, a retractable Platinum foil in the secondary particle channel downstream of the target is installed at 105 mm from the main target in order to break up

metastable states. Ionization of metastable atoms in Platinum foil induces additional amount of "atomic pairs", which are absent in the absence of this foil.

The utilization of a small permanent magnet installed in the channel between the target and the foil will sweep out the charged pions (it will not affect the neutral atoms) and remove the peak in the relative momentum distribution for all “atomic” pairs produced in the target and thus will provide significantly better background conditions for observation of “atomic” pairs produced in the foil.

3. Beam, target and magnets

3.1 Proton beam

The upgraded DIRAC experimental setup is located at the T8 proton beam line of 24 GeV/c momentum in the East Hall of the PS accelerator at CERN. To extract protons from the PS into the T8 beam line, a slow ejection mode is used. The PS proton beam line includes bending, corrector and quadrupole magnets. The length of the proton beam line in the DIRAC experimental area is 32m. The beam is extracted in spills. The spill duration is 450 ms. Beam intensity is $(1.2-1.6)\times10^{11}$ per spill.

To measure the beam intensity and to tune the beam position on the target, the beam line is equipped at several locations with secondary emission chambers and luminescent screens with TV cameras.

The target station houses a remote controlled device with 12 holders for the targets, including an empty holder and a luminescence screen. During data taking, targets made of Pt (26 μm thick), Ni (98 μm and 108 μm thick) and Be (106 μm thick) were used. The dimension of the beam spot at the target location is about 1.75 mm (RMS) in the vertical direction, and about 2 mm in the horizontal direction at 2 ×RMS level.

The ratio of detector counting rates with the target in place to those with an empty holder was measured to be 25.

During upgrading, a new shielding with collimators (Fig. 3.1) for the proton and secondary beams was installed downstream of the target station. The dimensions of the shielding are $1.4\times2.4\times1.0$ m^3 (W× H×L). The total length of the new vacuum section is 3.3 m. The aperture of the collimator of the proton beam are 88×50 mm^2 (W × H).

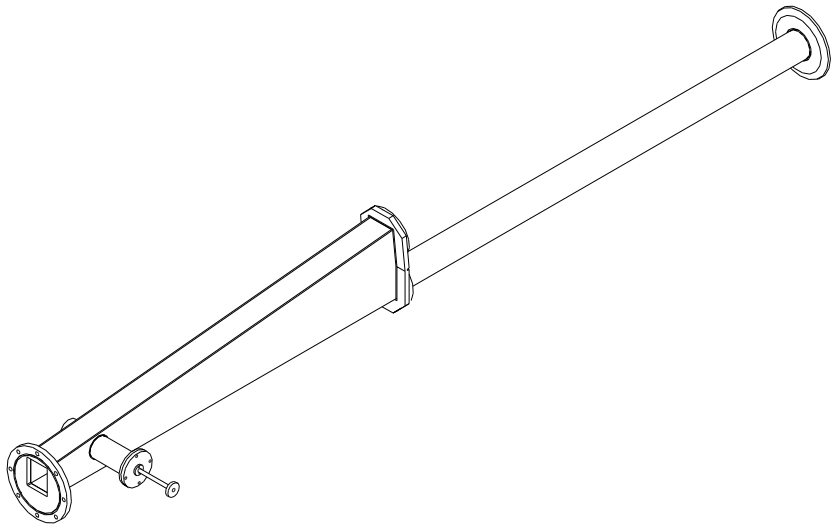

Fig. 3.1 Collimator

The downstream detectors are shielded from background secondary particles produced on the primary proton pipe and surrounding elements. For this purpose a 1 m thick iron wall was installed in 1998 between the upstream detector region and the spectrometer magnet. In addition, collimators are inserted both in the primary proton beam pipe and in the secondary particles channel. The presence of the collimator in the proton beam line significantly reduced background rate.

Beam position

The proton beam position on the target during the 2012 runs was evaluated for each run by reconstructed tracks in offline analysis with DC and SFD coordinate data. The result is shown in Fig. 3.2

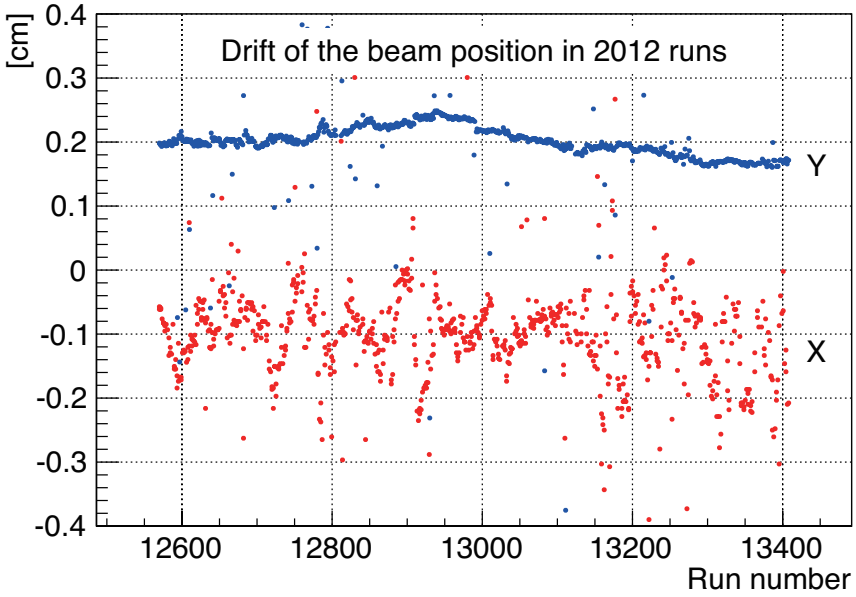

Fig. 3.2 y- and x- positions of the proton beam in the 2012 runs

The maximum deviation of the proton beam axis in y direction is 0.4 mm. The mean values and the RMS widths in two directions are:

$\mu_x \pm \sigma_x = -1.04 \pm 0.68$ mm

$\mu_y \pm \sigma_y = 1.99 \pm 0.26$ mm

Beam shape

The beam shape as well as the beam size have been measured in conjunction with the study of the effect of the beam halo on the metastable state observation. A Pt foil was placed in the secondary beam line. The bottom edge of the foil is at 7.5 mm above the center of the primary beam. We shifted the center of the primary beam in y direction to see if the proton halo hits the Pt foil, and thus the counting rate on a slab of IH increases. When the distance between the central axis of the primary beam and the lower edge of the Pt foil is reduced to 3.5 mm, the counting rate on an IH slab starts increasing above the standard noise level. This rate measurement as a function of the height with respect to the primary beam line was carefully carried out, and it was found that the intensity of the primary beam has a Gaussian distribution in y direction with a width $\sigma < 1.75$ mm, it varies very smoothly, and no separate spot (isolated halo) has been observed.

Independently, another measurement was carried out. We installed a 0.3 mmϕ copper wire horizontally on the yoke of the small magnet. This wire, together with the magnet yoke, can move vertically. In the absence of the target, we measured the rate of the secondary particles stemming from the copper wire using again slabs of IH, which is proportional to the intensity of the protons hitting the copper wire in the primary beam. It was again confirmed that the intensity distribution of the protons within the primary beam is smooth and follows a Gaussian distribution with $\sigma < 1.75$ mm.

3.2 Target station

The DIRAC target station is an aluminum box that accommodates a marguerite type rotary target system and a small magnet assembly. (See Fig. 3.3)
The marguerite system has 12 target frames. In addition to the frames used for the physics targets mentioned below, one frame holds a ZnS scintillating plate used for the beam tuning, and one frame is just empty.

The target station is placed between the vacuum channel for the incoming proton beam and the DIRAC collimator shown in Fig. 3.1.

In DIRAC experiment, different types of target, listed in Table 3.1, have been used for physics during the data taking between 2007 and 2012.

Table 3.1 Targets used in the DIRAC experiment

Year	Target	Thickness (μm)	Thickness (Radiation Length)	Thickness (Nuclear Interaction Length)
2007	Pt	28	92.2×10^{-4}	3.3×10^{-4}
2008	Ni	98±1	6.7×10^{-3}	6.4×10^{-4}
2009	Ni	108±1	7.4×10^{-3}	7.1×10^{-4}
2010	Ni	108±1	7.4×10^{-3}	7.1×10^{-4}
2011	Be (+Pt)	106.4±0.6, (2.1±0.3)	3.0×10^{-4}, (6.9×10^{-4})	2.5×10^{-4}, (2.3×10^{-5})
2012	Be (+Pt)	106.4±0.6, (2.1±0.3)	3.0×10^{-4}, (6.9×10^{-4})	2.5×10^{-4}, (2.3×10^{-5})

Pt and Ni targets have been used for the lifetime measurements of $\pi^+\pi^-$, π^-K^+ and π^+K^- atoms. A Be target was used together with a thin Pt foil placed at 105 mm downstream of the Be target in the secondary beam line for the observation of metastable atoms. A Platinum foil is placed in the secondary flow of particles so that the bottom edge of the foil is 7.5 mm away from the primary beam axis.

A general view of the spatial arrangement of the marguerite, permanent magnet and platinum foil is shown in Fig. 3.3

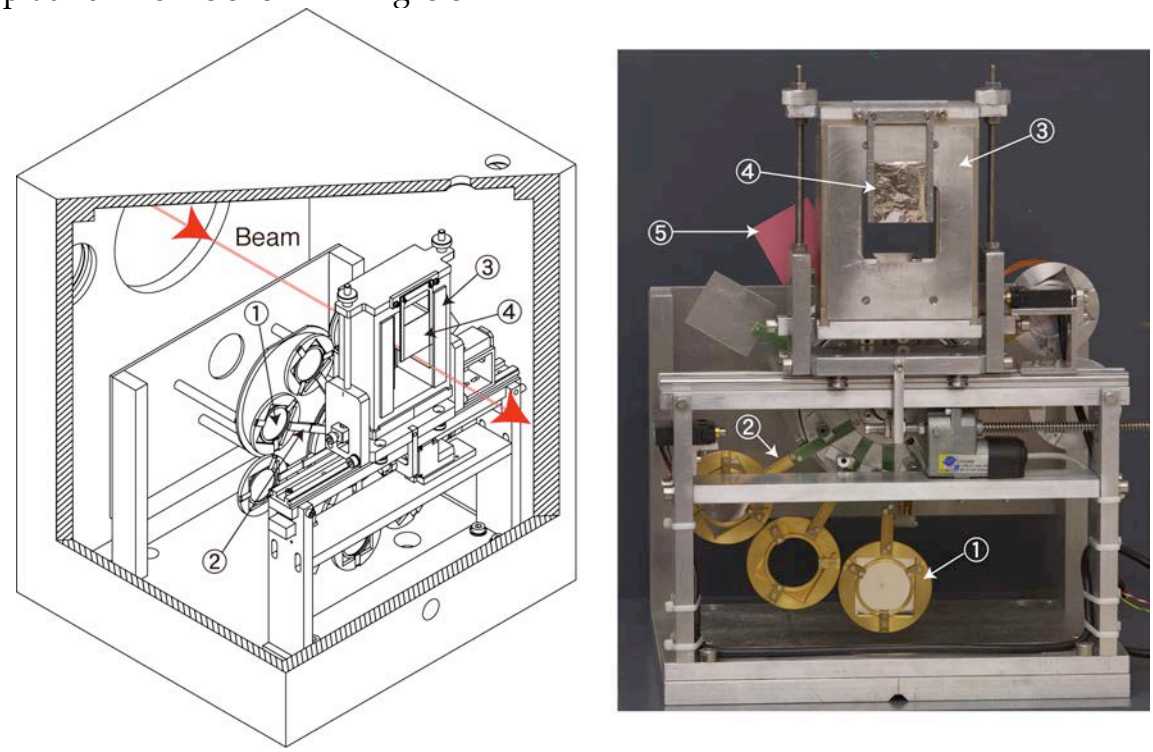

Fig. 3.3 General view of the target station (left) and the photo of permanent magnet, actuator and marguerite holding targets (right). 1. target, 2. marguerite, 3. permanent magnet, 4. Pt foil, 5. Scintillating screen

3.3 Small magnet

A dipole magnet was installed for the observation of metastable atoms [VOR12]. It was revealed, however, that a significant radiation background emerges at the planned position of the small magnet in case some malfunctioning of the transport system for extracted beam occurs.

For this reason, Sm_2Co_{17} with a high radiation hardness was used as the material for the permanent magnet poles. The magnet parameters, such as aperture, integrated magnetic field and required field quality are determined by the beam optics. The full magnet aperture was fixed to 60 mm so as to keep off additional background caused by the beam halo. The magnet provides an integrated field strength of $B \times L = 0.0213$ T·m, defined as an integral of horizontal field component B_x at transverse position X = Y = 0, the magnet centre being at $z = 0$. The integrated field homogeneity, ($\Delta \int B_x dz / \int B_x(0,0,z) dz$) is better than ± 2% inside the good field region of 20×30 mm^2. The overall length of the magnet is 66 mm, which is determined by the required beam optics, yet the existing target station can accommodate the magnet.

The magnet measures 130 mm (width) and 170 mm (height) and weighs 8.6 kg. Fig. 3.4 shows the sketch of the magnet with detailed information about the size and composition of the magnet blocks. The grade of the permanent magnet blocks in Sm_2Co_{17} is equivalent of the «RECOMA 30S» from ARNOLD Magnetic Technologies having the maximum intrinsic coercivity among alloys with high radiation hardness. The return yoke consists of four pieces of soft ferromagnetic steel.

As it is occasionally necessary to calibrate the setup without magnet, a special retractor was designed for the magnet displacement. Fig. 3.3 (right) shows the photo of the magnet mounted on a movable support with an actuator (Mini-Actuator HG2-05240 TECHNISCHE ANTRIEBSELEMENTE GMBH, Lademannbogen 45, 22339 HAMBURG (TEC467, MA01)). One can see also the marguerite holding targets.

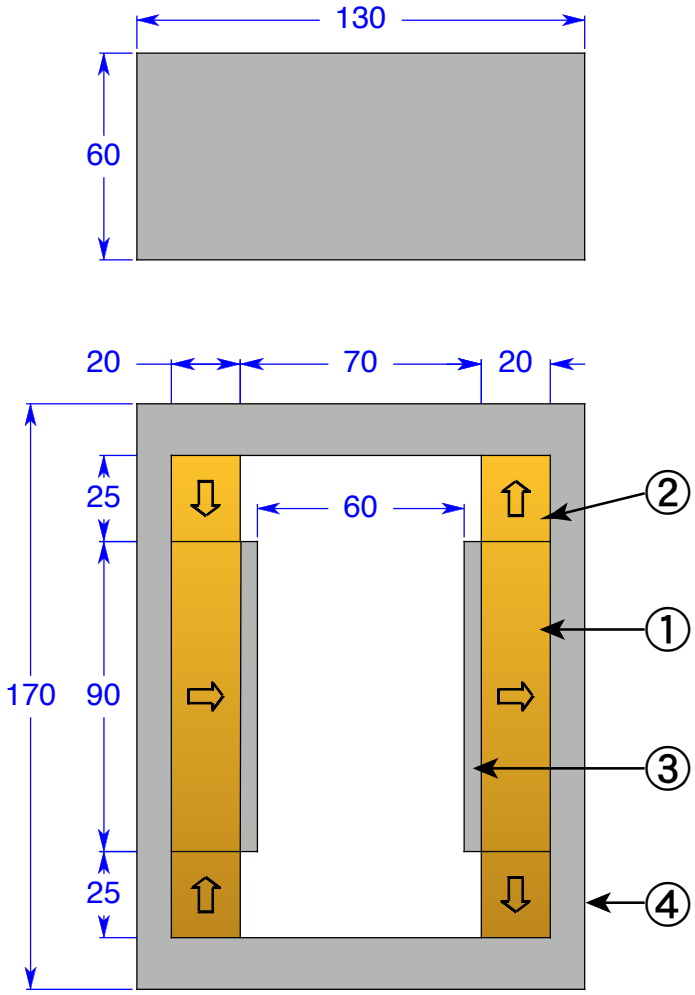

Fig. 3.4 Layout of the dipole magnet (only magnetic components are shown), with arrows indicating the direction of magnetization of the blocks. 1. PM block Sm2Co17 "Recoma30S", 2. M block Sm2Co17 "Recoma30S", 3. Pole AISI 1010, 4. Return yoke AISI 1010

3.4 Beam dump and shielding

Downstream of the target station, the proton beam travels in a vacuum channel below the magnet and detectors and finally is absorbed by iron in a beam dump. The beam dump dimensions are: $8.0 \times 3.2 \times 3.2$ m^3 (L×W×H).

To decrease the background gamma and neutron fluxes from the beam dump towards the detectors, a radiation shielding has been installed [KUR96]. It includes a graphite core in the beam dump area, a concrete wall near the beam dump and, at 3 m distance, another iron-concrete-iron wall, both with holes to allow the passage of the proton beam pipe. In addition, to decrease the slow neutrons in the detector area, a block of borated polyethylene with a hole in the middle was attached to the concrete wall. To decrease the muon flux from the beam dump an additional cast-iron shielding was added in 2007. That allowed increasing the intensity of the proton beam by about 6 times.

All the setup is surrounded by a radiation shielding to protect the outer hall against radiation from the experimental zone. The dimensions of the shielding are $43 \times 13.6 \times 4.4$m^3 (L × W × H). The shielding consists of steel (0.8 m thick) and concrete (0.8 m thick) covered by a roof (2.4 m thick).

The apparatus being located in a fully enclosed area, it has become necessary to provide the experimental area with cooling equipment to prevent overheating of detectors and electronics.

3.5 Secondary particle channel

Atomic $\pi^+\pi^-$ and $\pi^{\pm}K^{\mp}$ pairs enter the secondary particle channel. They pass through vacuum chambers and are bent by the 1.65 T field of the dipole magnet. The channel consists of: first collimator, air gap, second collimator, cylindrical tube and flat vacuum chamber placed between the magnet poles.

The first collimator is a new vacuum section in cast-iron shielding located immediately downstream of the target station. Secondary particles exit this tube through a window, made of 100 μm thick mylar film. An air gap between the two vacuum sections allows insertion of the upstream detectors: MDC, SFD and IH.

The angular aperture of the channel is determined by the second collimator and is equal to $\pm 1^{\circ}$ in horizontal and vertical directions resulting in a solid angle acceptance of 1.2×10^{-3} sr. The second collimator is in a cast-iron shielding of dimensions $3.6 \times 3.0 \times 1.0$ m^3 ($W \times H \times L$). The flat chamber is ended with a 0.68 mm thick Al outlet window of 2.0×0.4 m^2 dimensions ($W \times H$).

The total thickness of the materials encountered by the secondary particles before they reach the DC system, where their momenta are measured, is about 0.077 X_0.

3.6 Spectrometer magnet

The spectrometer magnet MNP21/3 is installed at the end of the secondary particle channel. The magnet with magnetic field B = 1.65 T, BL = 2.2 T·m has an aperture of $1.55 \times 0.50 \times 1.10$ m^3 ($W \times H \times L$).

To reduce the stray field, two magnetic screens are fixed near its entrance and exit. The screens are three-layered and have aperture holes.

The total weight of the magnet is 120 tons, its power consumption is 1.43 MW and the maximum current is 2500 A.

4 Frontend Detectors

4.1 MicroDrift Chamber (MDC)

The microdrift chamber system (MDC), as one of the frontend detectors, was to be used to perform particle tracking in the area upstream of the dipole magnet. The MDC is located behind the first shielding wall near the target in a hard irradiation area. The counting rate on the sensitive area of the detector is more than 10^7 particles/s. Thus MDC has to provide a high counting rate capability (low dead time, small dead zone). A primary ionization in the MDC cells, produced by different kind of particles, varies from a few electrons to a few thousand electrons. The pulse amplitude varies from 1 μA or less to a few mA. A threshold of 8 μA and rise time of 3ns were chosen as a reasonable input parameters to MDC readout electronics.

MDC measures particle coordinates using 18 identical planes combined into 9 modules.

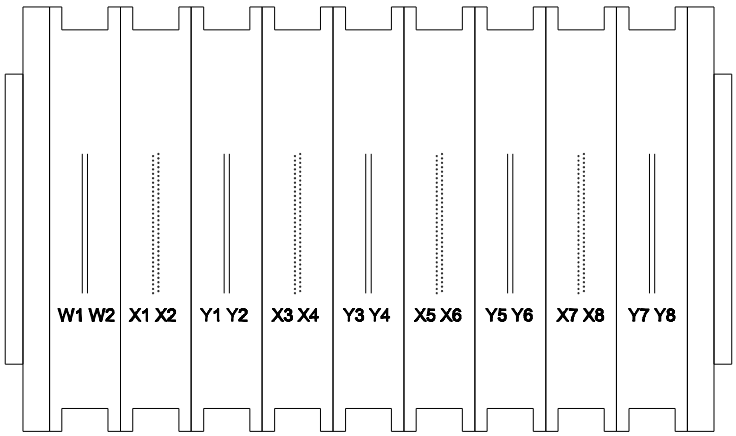

Fig. 4.1 Combination of the modules of MDC

Arrangement of the modules: (WW, XX, YY, XX, YY, XX, YY, XX, YY), as shown in Fig. 4.1, where W plane is rotated by 10 degrees with respect to the Y-axis. Each module contains 2 complementary planes shifted by half a sensitive wires pitch, with 32 sensitive anode wires in each plane. This design is usually employed to eliminate a left-right ambiguity. It also helps to solve the problem of two close tracks detection. For more detailed description, see ref. [DUD09].

A schematic drawing of the MDC sensitive area is shown in Fig. 4.2.

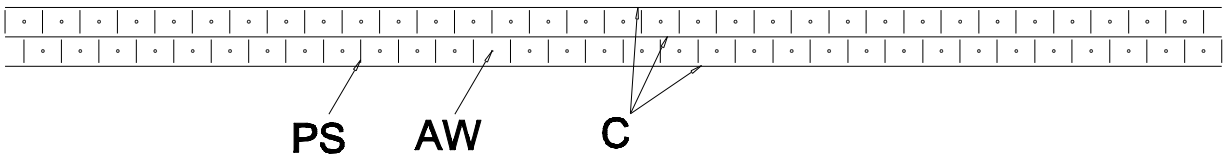

Fig. 4.2. Schematic view of the MDC electrodes: AW – anode wires, C – cathodes, PS – potential strips

The pitch of anode wires and that of potential strips are both equal to 2.54 mm. The distance between the anode and cathode planes is 1 mm. The anode is made of 20 μm

gold-coated wolfram wires. Cathode planes and potential strips are made of 20 μm thick carbon-coated mylar foils. MDC contains 576 electronic channels, and the sensitive area of MDC is about 80 × 80 mm^2.

MDC is filled with well-known argon-isobutane gas mixture: Ar [33%] + iC_4H_{10} [66%] + H_2O [1%] (2atm absolute)

The designed performance is listed as follows:

Double track resolution < 0.200mm

Coordinate resolution < 30 μm

Efficiency > 95% per plane at the primary beam intensity of 2×10^{11}protons per spill

Low multiple scattering: total detector thickness < 5×10^{-3} X_0

Time resolution < 1ns

Small readout time < 3×10^{-6}s

Maximum drift time 23 ns

Performance

MDC was designed and tested on the DIRAC setup in 2003-2005. Starting from 2007 the MDC data are included in DIRAC DAQ system. This detector was used in the data taking of the years 2008 – 2010.

On the Fig. 4.3, the beam position and its spread collected with MDC during the 2007 runs are shown.

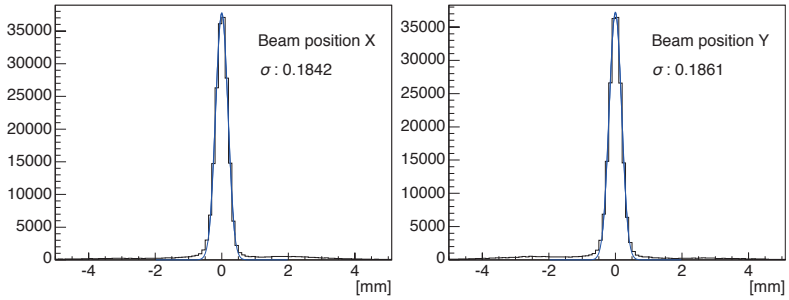

Fig. 4.3 The beam position and its spread collected with MDC during the 2007 runs

Due to the difficulty in operating such a detector in a very high intensity beam, the effective detection efficiency of the planes remained relatively low. However, helped by the large number of planes, the data from this counter is expected to be efficiently used in the data analysis in the reduction of background tracks in events where the multiplicity of the charged particles is very high.

Due to an instability problem, the detector was removed from the spectrometer in 2011.

4.2 Scintillation Fiber Detector (SFD)

4.2.1 Principal updates and the main characteristics

The role of SFD (Scintillation fiber detector), installed downstream of MDC at 2.8 m from the target, within the DIRAC spectrometer is to identify geometrically-close pairs of charged particles produced in the target in the secondary beam. This detector, as one of the front-end detectors, must have a good detection efficiency even in the high-intensity beam including background particles. A good spatial resolution is the most important characteristic of the detector, but it must have also a relatively good timing resolution in order to identify pairs of particles originating from one event.

At the starting of DIRAC experiment, a couple of detector planes (X and Y) consisting of 0.5 mmϕ scintillating fibers, which are read out with PSPM (position-sensitive PMT), have been installed and were named SFD. In the course of data taking quite a few improvements have been brought to SFD.

First was to add a new diagonal U plane detector to resolve the ambiguity in the combination of hits in case more than one hit is detected by SFD. This addition helped also the improvement of the detection efficiency (one can eventually require hits on two planes out of three). This plane became operational in early 2002.

In addition we could successfully replace the 0.5 mmϕ scintillating fibers by those of 0.28 mmϕ (HRH: high-resolution hodoscope; The diameter is further reduced to 0.26 mmϕ in the new setup in X and Y planes). This improvement not only gave a very high spatial resolution (0.075 mm RMS), which is almost comparable to that of chamber detectors, but also helped to increase the efficiency due to the increased granularity, and allowed to accept even higher beam intensities. It was technically very difficult to build a detector with such thin fibers, but a development of new techniques and tools finally allowed to build a pair of prototypes of about 5 cm x 5 cm. They have demonstrated to give a light-output of 10.90 ± 0.80 photoelectrons per hit in average [GOR06], and encouraged us to build a full size (10.4 cm x 10.4 cm) X and Y planes (named new SFD) which became operational in autumn 2006.

Another improvement was a replacement of the readout electronics. At the beginning SFD used a discriminator called PSC (peak-sensing circuit) to avoid counting as two hits when one particle goes between two columns of scintillating fibers [GOR00]. Later, however, shortcomings of PSC were revealed namely when a real pair of particles goes through two adjacent columns of the SFD planes, their signals cancel each other to some extent, and the detection efficiency for this event was reduced. Using TDC-F1 chip developed by the Freiburg group [ACA01], a so-called F1-TDC-ADC (D412 see Chap. 6) was designed. The timing resolution of the TDC-F1 is 120 ps (optionally 60 ps) and is much better than 500 ps of LeCroy 3377 TDC used for the readout of PSC. Therefore the use of this readout electronics improved also the timing resolution of the detector from 660 ps with the LeCroy 3377 to 450 ps with the new circuit.

4.2.2 Construction of the planes

The Scintillating Fibre (SciFi) bundle (sensitive plane) is made of SCSF-78M (KURARAY, Japan) double-clad fibres. The cross section of the fibre is round and the outer diameter is 0.26 mm (0.57 mm for U plane). A sketch of the construction of the X and Y planes is shown in Fig. 4.4. A particle coming in perpendicularly to the plane goes through a "column", or "channel" of fibres consisting of 8 (3) SciFi (see the inset left of Fig. 4.4). This number has been chosen so as to obtain enough light when a minimum ionizing particle hits the plane. To avoid dead space and to obtain a uniform response, SciFi

columns are overlapped, and the resulting column pitch is 0.205 mm (0.43 mm). Fibres in the bundle are fixed with water-soluble white paint. The sensitive area of the new SFD is 104 x 104 mm^2.

Each plane has 480 (320) columns of SciFi. The ends of the SciFi are joined with clear fibres (also KURARAY double-clad type with an attenuation length of ~3m) with the same diameter as SciFi and with a length of about 300 mm. An aluminized mylar foil is glued to the opposite end of the SciFi so as to increase the light output. Eight (three) clear fibers joined from a column of SciFi bundle are carefully polished and glued into the holes of a square black plate, which fixes the fibre positions on the 16 photocathodes of position-sensitive photomultipliers. No optical grease is used.

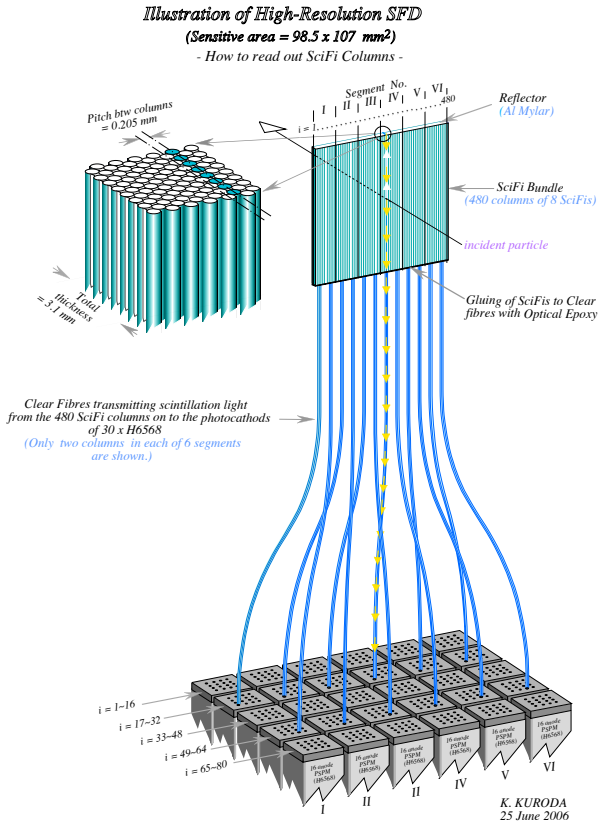

Fig. 4.4 Sketch of the construction of X and Y planes

Sixteen-channel metal dynode position-sensitive photomultiplier tube, Hamamatsu H6568Mod2, has been selected as photosensor. This photomultiplier is characterized by good timing properties (rise time ~0.7 ns), low noise (1–2 pulses/s at a nominal detection threshold) and perfect single photoelectron spectrum. It has been modified to monitor the amplitude from the last dynode for calibration purposes. The level of optical cross-talk among the PSPM channels was found to be ~1% (with a 1.6 mm diameter light spot on the photocathode). The measured linear range of this tube (for the linear bleeder) extends up to 15 photoelectrons at 950 V.

The SFD individual planes are installed close to each other. Direction of fibres is orthogonal in planes X and Y while plane U is rotated by 45 degrees. The U-plane nearly in an octagon shape, has 5 sections of different fibre lengths to cover roughly the same

area like the X- and Y-planes. Fig. 4.5 shows the photo of the three planes, X, Y and U installed. Fig. 4.6 shows the X and Y planes ready to be put in the housing.

The detail of the construction and the performance of HRH can be found in the reference[GOR06].

The geometrical specifications of the three planes of SFD are summarized in Table 4.1.

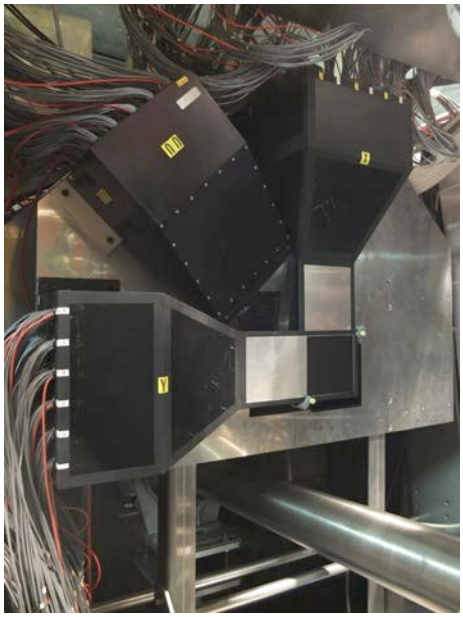

Fig. 4.5 Three planes X, Y and U of SFD installed in the beam line

Fig. 4.6 New SFD X and Y planes under construction

Table 4.1. Specification of the SFD planes

Plane	Scintillator material	Fiber diameter	Fibers/ column	column spacing	Number of channels	Number of PSPM
X	SCSF78M	0.26 mm	8	0.205 mm	480	30
Y	SCSF78M	0.26 mm	8	0.205 mm	480	30
U	SCSF78M	0.57 mm	3	0.43 mm	320	20

4.2.3 Light yield and detection efficiency

One can expect a very good efficiency due to the relatively large observed number of photoelectrons (and its small variation) in a passage of a minimum ionizing particle in the counter and the good behavior in the small amplitude signal region (low noise and clearly-visible single photoelectron peak) of the PSPM used.

One factor that could limit the efficiency is the hardware (firmware) threshold applied to the F1-TDC-ADC unit. When the threshold is below 10 mV, the F1-TDC-ADC unit becomes a little unstable. Thus we set the threshold to 10 mV. This value, however, corresponds to a fraction of the position of single photoelectron peak, and therefore this should not reduce the efficiency significantly.

Event selection

Events, which involve only one track in each arm reconstructed using DC, were chosen among the mixed trigger events (mostly π^+- π^- with about 11% of e^+- e^-). Without using the SFD information, that means assuming that the particles are coming from the center of the target, the tracks are calculated, and the hits on the SFD planes are predicted. In such a reconstruction, it is known that the precision of the prediction is about a few cm. Therefore, if hits are predicted near the edge of the SFD planes, the real track might go outside the sensitive area of the plane. Thus as samples we kept only events whose hits are predicted to be confined in the square of 50 mm by 50 mm at the centre of the plane. It should be noted that this event selection is applied only for this analysis, and not for the physical data analysis, where information from other detectors is also available.

Triplets

As the three planes, X, Y and U are installed close, there is a certain relationship between the three hit positions of a track as far as the track is almost parallel to the z axis. Fig. 4.7 shows the situation of the hits on the 3 planes and the hits predicted by DC. The symbols used in the figure are explained in the caption. Fig. 4.8 shows the histogram of events as a function of the value $x + y - 3u$, where x, y and u are column number of the hits on each plane. (The units are 'column numbers'. It should be noted that the column separation is almost 2 times larger in U plane.) In addition to the sharp peak, one observes a relatively large background. This is because in this histogram all the combination of multiples hits on the three planes are plotted. Therefore the hits not from one track form a random background. From the small width of the central peak, one could see that if one takes the combinations within ±10 channels, then the right hit combinations are all taken. We call those hits within this width the 'triplets' in this paper.

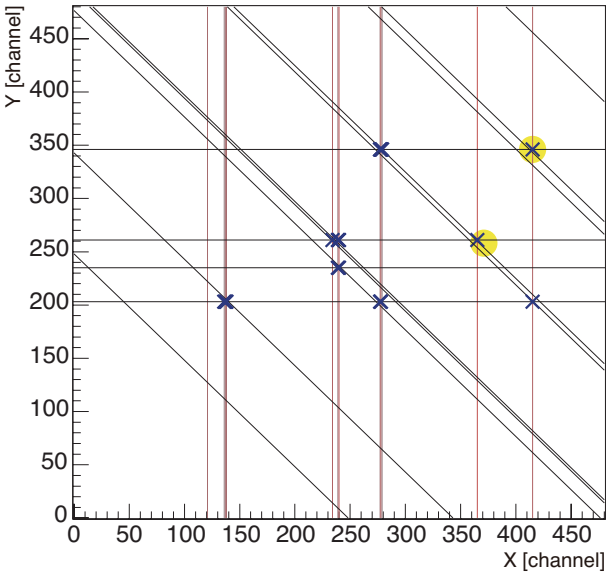

Fig. 4.7 Typical event display showing a rather cluttered event with many hits. The vertical lines show the hits on X plane, while the horizontal, on Y plane. The diagonal lines represent the U plane hit positions. The blue cross marks show the successfully reconstructed triplets (see text). The yellow disks represent the projection by DC.

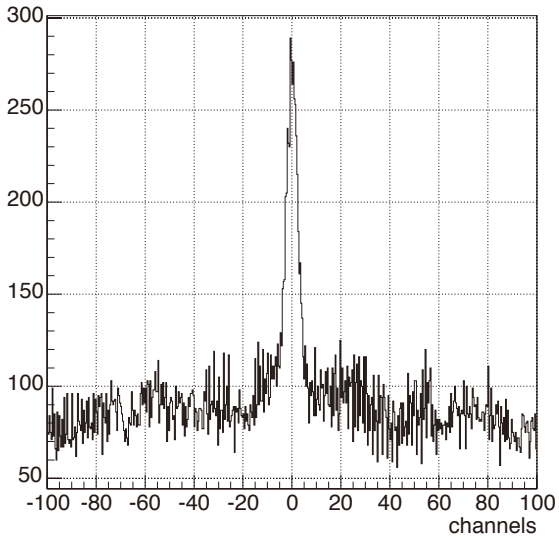

Fig. 4.8 Distribution of the value $x_i + y_j - 3u_k$ of all the hit combinations of 3 planes where x_i are hits on the X plane, y_j Y plane and u_k U plane. The central peak ±10 channels represents the triplets. The background level is high because all the hit combinations are included in the histogram.

Pulse-height dependence of the X plane efficiency

The use of F1-TDC-ADC allows us to record the pulse height of each hit. As mentioned above, the software (firmware) threshold of F1 module has been set to 10 mV. At that level, only obvious background noise is rejected. Fig. 4.9 shows a typical raw pulse-height distribution of the X plane. F1 module does not record the hits with (nearly) zero pulse height, thus the 'pedestal peak' observed when a conventional ADC is used is not seen. The sharp and large peak on the left side of the structure observed is due to the single-photoelectrons. This is produced mostly by the cross talk between channels [GOR06].

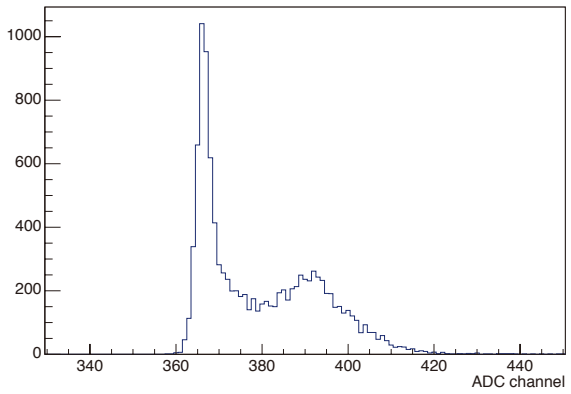

Fig. 4.9 Pulse-height distribution of a column of the X plane. The left-side peak is a single photoelectron peak which is in reality very narrow. In this histogram, all the signals from 480 columns are added without being normalized, that makes the peak broad.

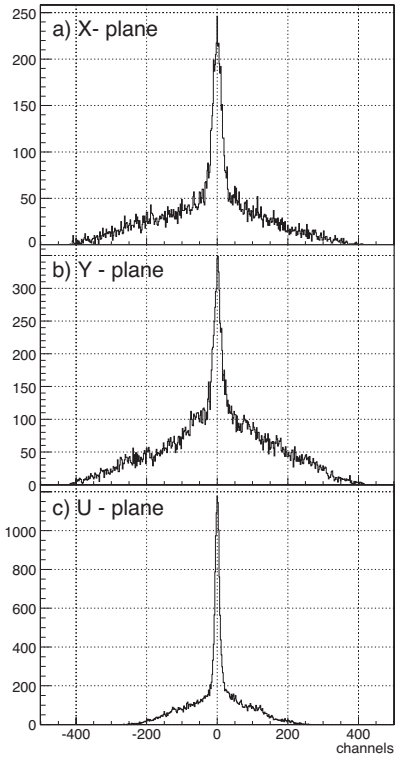

Fig. 4.10 Distances between DC predictions and the hits on 3 planes which are members of all the triplets found in one event.

Offline PSC

It is difficult to decide where the offline threshold should be set. The lower the threshold is, the higher the apparent efficiency, which is expected to rise up to almost 100% judged from the number of photoelectrons observed. Before the introduction of the F1-TDC-ADC units, the PSC has been implemented. The threshold of PSC was set just above the single photoelectron peak, and a criterion applied was the hit multiplicity from the single tracks does not exceed 1.05 when PSC was tuned using the test beam T11. One cannot, however, apply this criterion this time, because there are always more than one hit on the planes in the DIRAC trigger condition, and the beam condition is different at T8

and T11. Thus we apply the offline PSC algorithm to X plane, and set its threshold so that the multiplicity of X plane be equal to Y (U) plane, which is read out with PSC as before.

Efficiency

As mentioned above, the existence of triplets gives a very good standard. In case a triplet is found within a 'certain distance' from the hit predicted by DC, we consider it as an efficient instance. But the number of triplets is 4.2 in average in an event. Thus the problem is how to fix this distance criterion. Fig. 4.10 shows the distance from the predicted point of hits on each plane that form all the triplets found. This figure shows that the widths of the peaks are ±45 channels for X and Y planes, and ±21 channels for U plane. One can conclude that if the distance exceeds square root 2 times 45 channels, namely 63.6 channels (13 mm), the hit is surely a background.

In the next step, we remove all the hits within triplets that are successfully associated with DC predictions.

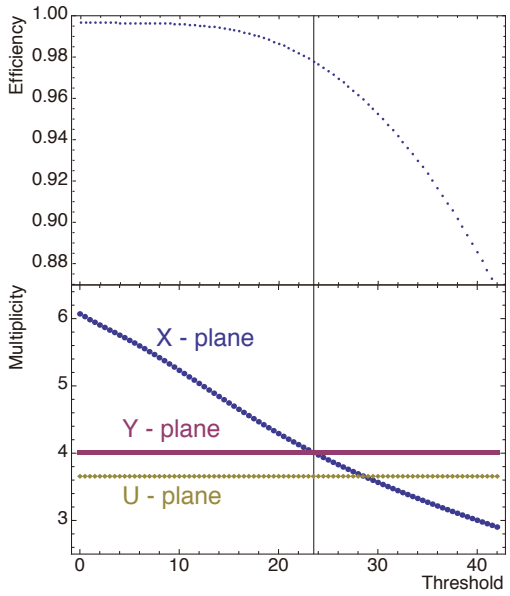

Fig. 4.11 Efficiency of the X plane as a function of the offline PSC threshold (Top) and multiplicity of hits in X, Y and U planes as function of the offline PSC threshold (Bottom). The threshold is plotted in the unit of F1-ADC channel. At threshold = 23.5, the multiplicity of the X plane is equal to that of Y plane whose hardware PSC threshold has been tuned in the T11 beam line (see text).

From the stringency of the triplet condition, triplets are not expected to be formed in case a plane is inefficient. Thus among the remaining predicted hits, those which have a hit reconstructed with only two planes within the above-mentioned distance, we consider that this is due to a missed hit in a plane. The efficiency of the X plane thus estimated is plotted in Fig. 4.11 (Top) as a function of the offline PSC threshold. The offline threshold is applied to

$$A_i - (A_{i-1} + A_{i+1})/2$$

where A_{i-1}, A_i, A_{i+1} designate the pulse heights of the three adjacent columns $(i - 1, i, i + 1)$. On the other hand, the multiplicity which changes depending on the threshold is also shown in Fig. 4.11 (Bottom). (The unit is F1-ADC-TDC channel.) In this figure, the multiplicities of the Y and U planes tuned at the T11 beam line are also indicated. For example, the offline PSC threshold that gives the same multiplicity as Y plane is 23.5, and

the efficiency of the X plane at this threshold is 0.978. It should be noted that this efficiency and the multiplicity are those for a single track. The efficiencies of the Y and U plane corresponding to the offline PSC threshold of 23.5 are 0.976 and 0.992.

4.2.4 Time resolution

For the investigation of SFD timing properties, the difference of time measured with new SFD planes and that measured with VH for particles with measured momenta (time-of-flight) has been used. Individual time resolutions have been obtained from sigma value of Gaussian fit of measured time distributions in each plane (example shown in Fig. 4.12). For X-plane of new SFD, amplitude correction (move of the F1-TDC-ADC trigger timing as a function of the pulse amplitude) was switched on whereas for U and Y planes the resolutions were determined without amplitude corrections. To obtain real time resolution of each plane, it is needed to subtract time resolution of VH from each sigma value, because the VH resolution is a part of total resolution of SFD. Final results are summarized in Table 4.2.

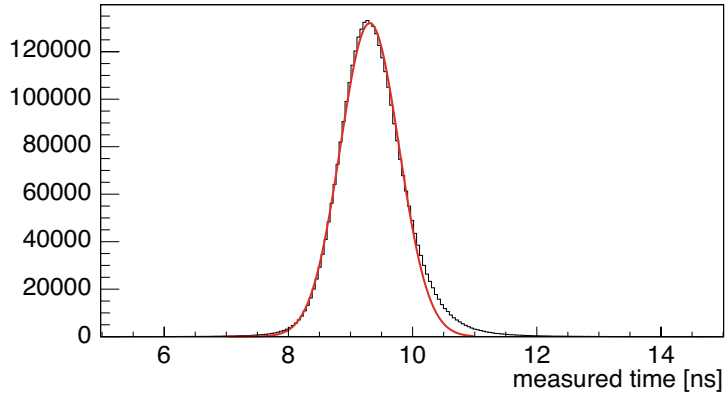

Fig. 4.12 Typical time difference between SFD and VH

Table 4.2 Time resolution of indivudial SFD planes for 2008 and 2010 year

time resolution [ps]			
plane	SFD		
	X	Y	U
2008	379	508	518
2010	382	517	527

4.3 Ionization hodoscope (IH)

4.3.1 Light yield

Characteristic situation with the DIRAC experiment is that one has to detect pairs of particles with small relative momentum ($Q < 2\text{MeV}/c$) that results from break-up of atoms. When those particles are very close on an SFD plane, and hit the same column of it, the SDF gives information of only one hit. With the information obtained solely from the SFD it is not possible to tell either the event consists of one particle or more in that case. To resolve this problem, four planes of Ionization Hodoscope (IH) were used in order to measure the ionization loss of the particle(s) which is proportional to the charge of the particle(s) passed. It is placed behind the SFD at 3.1 m from the target. The IH detector is a hodoscope composed of four planes, two vertical and two horizontal placed alternately (X - Y - X' - Y'). A plane consists of 16 strips (slabs) of scintillators with a size of 7×110×1 mm^3 each. The sensitive area is 110×110 mm^2. Mechanical part of the detector was not changed from the beginning of exploitation in 2001 when it was installed in the DIRAC setup. (The detail is described in a previous paper about DIRAC setup [ADE03A]). A more complete description of the detector and its performance are reported in a separate publication [BIT04]. Two improvements, concerning both electronics part are mentioned here. First, amplifiers with low-noise and high-bandwidth with a gain of 10 were installed between the PMTs and readout apparatus in order to reduce the HV applied to the PMTs so as to eliminate the small degradation of the amplitudes within a spill. Second, a readout system F1-TDC-ADC described in Chap. 6 is introduced.

As it was mentioned above, the detector is working as a front-end detector since 2001 without any interventions, but the light yield is still at a good level, which is confirmed in the following paragraph.

4.3.2 Pulse-height resolution

As the slabs used in IH are thin (1 mm) and long (110 mm) the light attenuation along the length of the slab is large, and as a result of which, the raw pulse-height spectrum is broad. To measure a correct energy-loss of a particle, one has to correct this attenuation. Fig. 4.13 shows a typical raw pulse-height distribution. Events are selected so that there is only one hit on a slab.

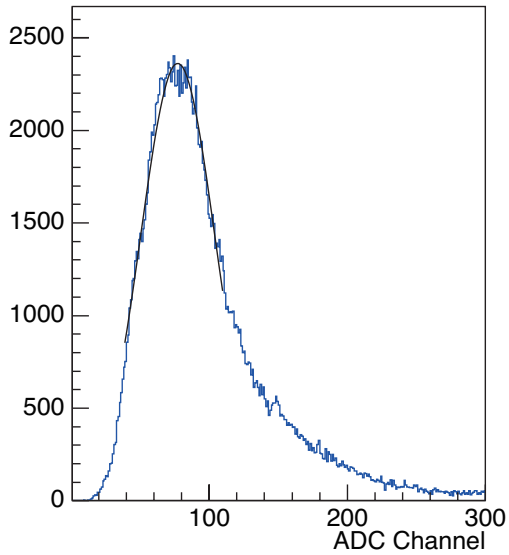

Fig. 4.13 Typical single hit spectrum. A long tail due mainly to the attenuation in the slab, in addition to the Landau effect, is clearly observed. (the 6th slab of the 4th plane). Run number 11315, 2011.

By fitting with a Gaussian the peak area in the pulse-height spectra of hits at different positions, we try to find the attenuation within a slab namely the position dependence of the peak-position. The hit position was obtained from the SFD information. However, this attenuation varies from slab to slab. Fig. 4.14 shows two examples of dependencies of the peak position on the position of the hit. Fig. 4.14 (a) is plane 2 slab 10, which has a relatively small attenuation, whereas (b) shows a large attenuation in plane 4 slab 6.

Fig. 4.14 (a) and (b) show the attenuation for the plane 2Y slab 10 and the plane 4Y slab 6, respectively. In each figure are shown two curves, result of two sets of runs within 2011 data. In fact this instability of the signal amplitude is a problem. An offline correction to the pulse-height, however, is possible since this variation is uniform within a slab as shown in Fig. 4.15.

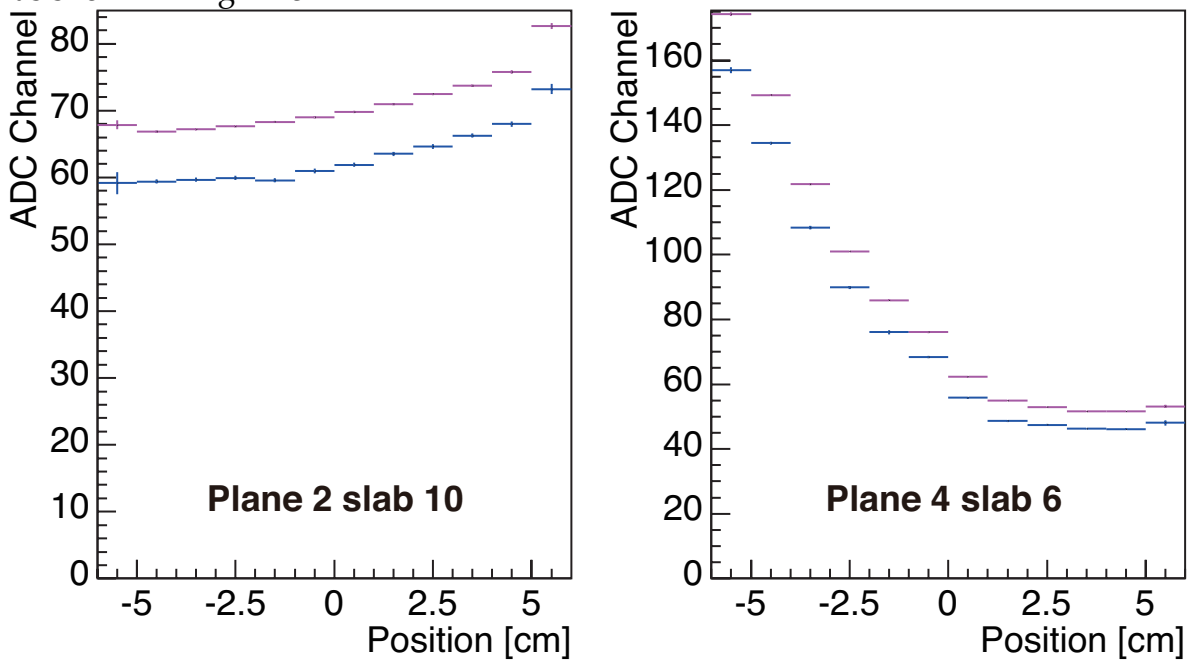

Fig. 4.14. Hit-position dependence of single-hit amplitude (peak) for two different run intervals of 2011 data set. Left: the 10th slab of the 2nd plane, PMT is on the right side.; right: the 6th slab of the 4th plane, PMT is on the left side. The two lines correspond to the data taken in two period, runs 11347-11408 and runs 11900-11985

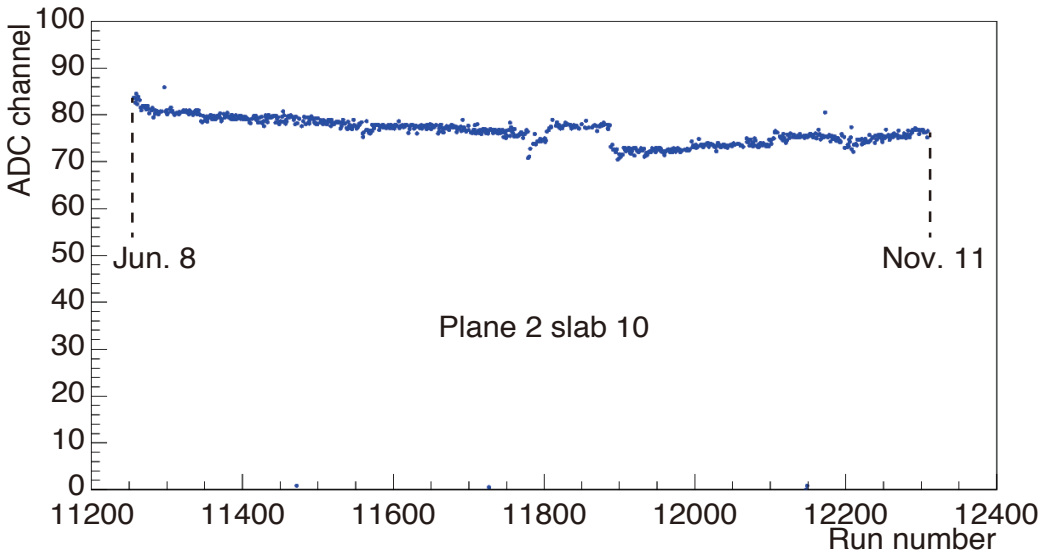

Fig. 4.15 Time dependence of single-hit amplitude peak position for 10th slab of the 2nd plane of IH during 2011 experiment run.

The pulse height spectra before and after correction of the attenuation effect along the slab length are shown in Fig.4.16 Top and Bottom, respectively. These spectra are obtained by summing up each spectrum from slab1 to slab16. The width of the corrected spectrum gets slimmer by 86% than the raw pulse height spectrum.

From this corrected pulse-height distribution, we tried to obtain an "effective number of photoelectrons" just by fitting the peak with a Gaussian.

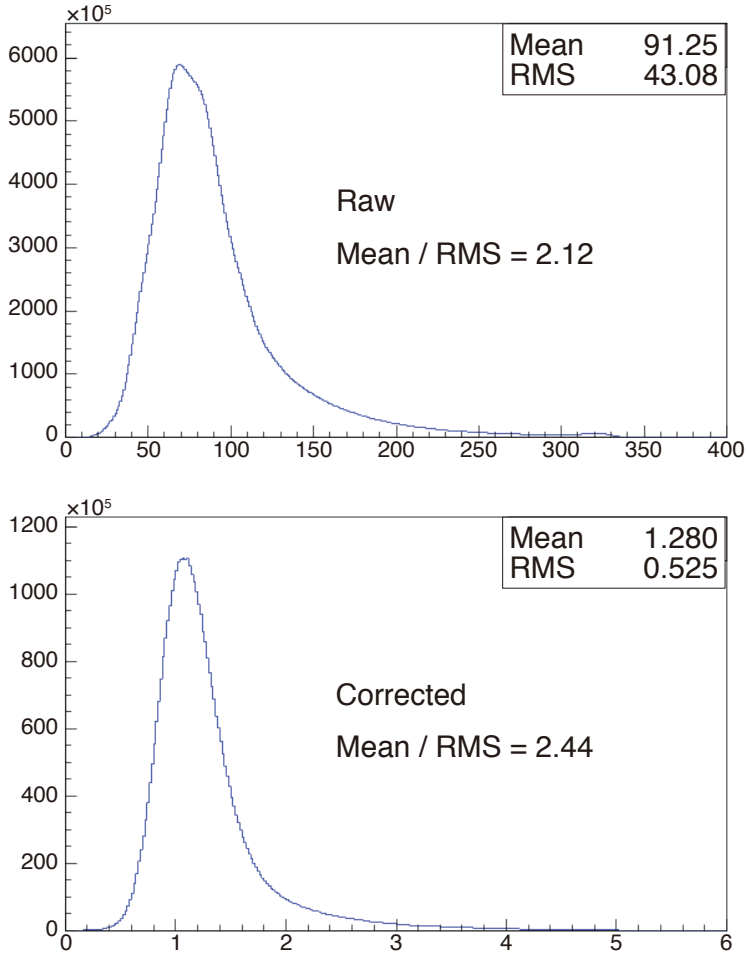

Fig. 4.16 Top: A raw pulse-height distribution for a single hit. The ratio mean/RMS = 2.12. Bottom: A correction to the attenuation in the slab is carried out to the spectrum shown in the Top. The ratio mean/RMS = 2.44. (plane 4 sum of all slabs. 2011 data)

Fig. 4.17 shows how the pulse-height spectrum looks like in case single and double hit events coexist. The events are selected so that two tracks of charged particles meet at one point in SFD, and actually one plane of SFD records two hits in adjacent columns or a hit in a single column. Due to the Landau tail, the single-double separation is not perfect. However, use of information about one hit on 4 planes should allow removing the effect of the Landau tail.

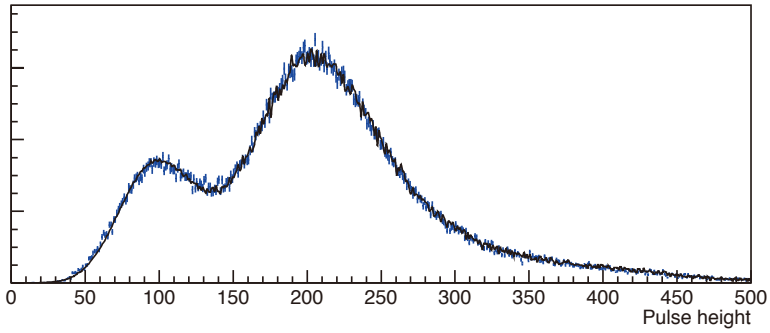

Fig. 4.17 IH slab records single hit and double hits. Special condition (see text) is applied so as to enrich the double hits. This histogram includes all the events taken within a year 2011

Using the corrected spectra for each slab, the variation of the 'effective number of photoelectrons' is obtained by applying a Gaussian fit to the central part of the spectra. The result is shown in Table 4.3.

Table 4.3 'Effective numbers of photoelectrons' obtained as a square of ratio of position and width of amplitude peaks was obtained for each slab in each plane.

Sl \ Pl	1	2	3	4
1	19.9	23.1	25.0	13.6
2	24.7	25.9	22.9	25.4
3	22.2	24.1	10.4	18.0
4	15.3	20.5	14.3	26.4
5	18.1	15.4	20.6	22.5
6	23.0	13.7	24.8	16.3
7	19.4	16.0	16.7	17.9
8	16.5	27.5	16.6	26.6
9	12.8	20.6	23.3	14.8
10	25.7	14.3	19.7	19.6
11	17.9	20.6	22.9	32.9
12	18.7	23.8	21.2	14.7
13	16.0	25.7	22.4	20.7
14	14.8	18.4	24.3	19.7
15	17.3	12.8	21.9	21.4
16	33.0	20.8	35.4	20.2

4.3.3 Time resolution

Individual time resolutions have been obtained from sigma value of Gaussian fit of measured time distributions in each plane. A typical time difference between a slab of IH and VH is shown in Fig. 4.18. To obtain the real time resolution of individual planes, it

is needed to subtract time resolution of VH from sigma values, because the VH resolution is a part of total resolution of IH. Final results are summarized in Table 4.3.

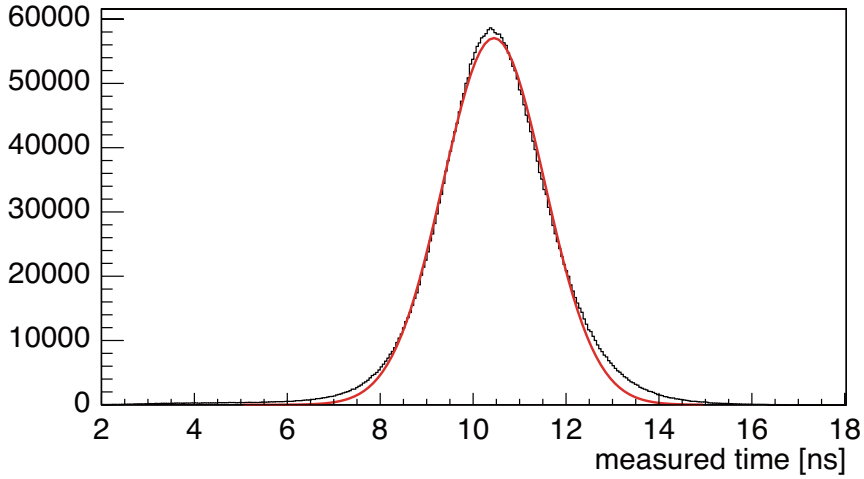

Fig. 4.18 A typical time difference between a slab of IH and VH Fit result is shown in red.

Table 4.3 Time resolution of indivudial IH planes for 2008 and 2010 year

time resolution [ps]				
plane	IH			
	1	2	3	4
2008	713	728	718	798
2010	907	987	997	1037

5. Downstream detectors

5.1 Drift Chambers

5.1.1 General layout and characteristics

The drift chamber system (DC) is used to perform particle tracking downstream of the dipole magnet. It operates at a high-intensity flux reaching 10^4 counts/cm^2 s .
The drift chamber system was designed and installed at the beginning of DIRAC experiment in 1999 and worked in a stable manner without damages and significant changes until the end of the measurements in 2012.

In 2006 during a technical stop of PS accelerator, this detector was refreshed. The sensitive areas of the chambers were cleaned and a few wires were replaced by new ones.

One can find a detailed description of the DC system in [ADE03A]. Only a short description of the device is given here together with a note on some small changes.

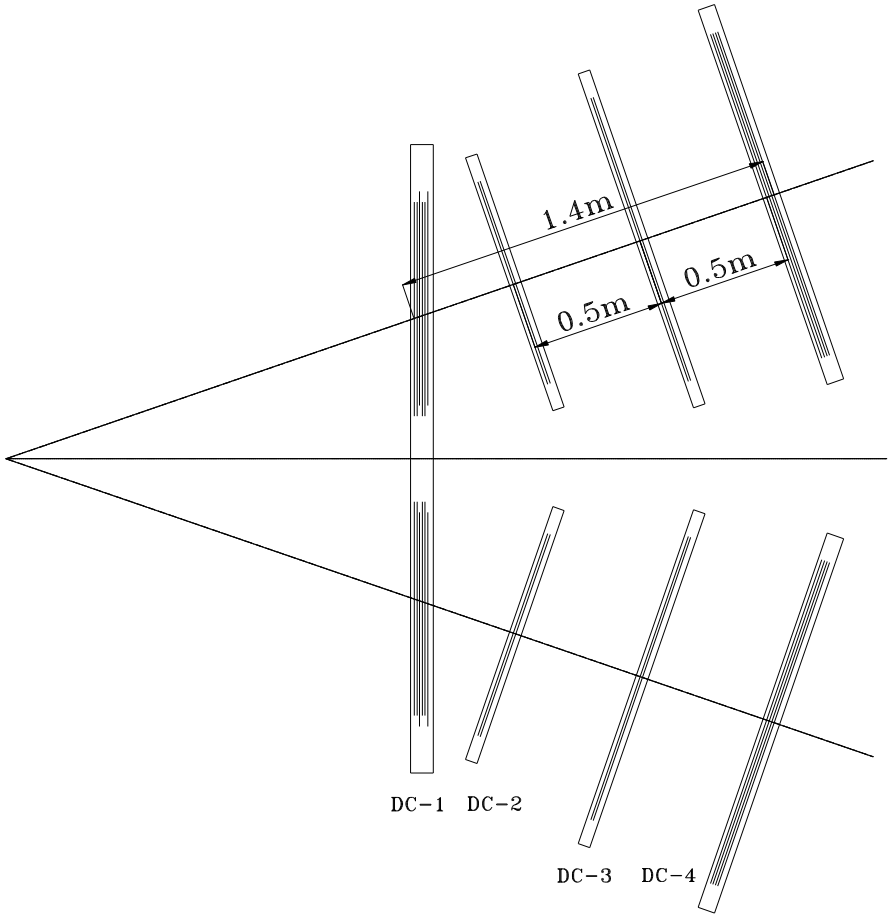

Fig. 5.1 Schematic view of the drift chambers system

A schematic view of the drift chambers system is shown in Fig. 5.1.
The drift chambers system includes 7 modules. Six modules (DC-2, DC-3, DC-4) installed in left and right arms of the spectrometer. The DC-1 module is common to both arms.
DC-1 is designed symmetrically with respect to the central axis with two separated sensitive areas of 0.8×0.4 m^2 each. This chamber contains 6 coordinate planes X, Y, W, X, Y,

W where W plane has an inclination angle of 11.3 degrees with respect to the X-coordinate. DC-1 is equipped with 800 electronic channels.

DC-2 and DC-3 chamber modules contain each 2 coordinate planes X, Y. DC-4 contains 4 coordinate planes X, Y, X, Y. The dimensions of modules are: 0.8×0.4 m^2 (DC-2), 1.12×0.4 m^2 (DC-3), and 1.28×0.4 m^2 (DC-4). Both arms together, the detector contains 1216 electronic channels. The distance between the center of the first half of DC1 and the center of DC4 is 1.4 m along the arm axis.

A schematic drawing of the sensitive element is shown in Fig. 5.2.

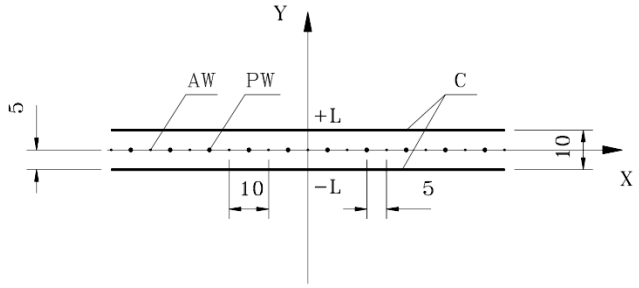

Fig. 5.2 Schematic view of the wire chamber electrodes: AW – anode wires, PW – potential wires, C – cathode foils. Dimensions are in mm

The anode-wire pitch is 10 mm, and the distance L between the anode and cathode planes is 5 mm. The cathode planes and potential wires are at equal voltages.
The sensitive area corresponding to each anode wire, limited by the cathode planes and potential wires, has a size of 10×10 mm^2.

With this design and with an argon-isobutane gas mixture, a linear behavior of the drift function is achieved, except for a small region near the potential wire. Cathode planes are made of 20 μm thick carbon-coated mylar foils. Such cathode foils provide a stable chamber operation due to a high work function of the carbon coating and add only a small amount of material along the particle path. Anode and potential wires of 50 μm and 100 μm diameter, respectively, are made of a copper-beryllium alloy.

5.1.2 Operation and performance

The drift chambers operate in a high current avalanche mode with a high pulse amplitude (about 1 mA) and a small pulse width (20 ns). The stable operation is achieved by virtue of an efficiency plateau larger than 1 kV. The single hit efficiency is above 96% at the particle flux of about 10^4 hits / cm^2 s.

The DC system operates at 3.75 kV. The threshold of electronics was set to 50 μA.

The employed gas mixture is Ar(50%) + iC4H10(50%) +H2O(0.5%). A small admixture of water vapour to the well-known argon-isobutane mixture improves significantly its performance. Probability of sparking decreases and the drift chambers operate in a more stable manner. The counting rate capacity increases more than 10 times. This allows working in a high current mode with relatively high threshold of electronics, even in hard irradiation conditions of DIRAC. Better than 90 μm coordinate resolution in the DC system was achieved. Tracking efficiency of the drift chamber system is about 99%.

5.2 Vertical hodoscope

5.2.1 Improvements and improved time resolution

A pair of Vertical Hodoscopes is used for precise time measurement of hadron pairs originating from the same proton-nuclear interaction. It also provides signals for the first level trigger. It is installed downstream of the drift chambers as shown in Fig. 2.2. The hodoscope design is essentially unchanged since the initial setup. Its design and performance were completely described in a separate publication [ADE03B]. The main difference is an increased number of slabs due to the need for increased acceptance. The effective area of VH after the upgrade is 400×1442 mm^2 for each arm (400×1300 mm^2 before), and the distance to the target is 11.6 m. After the modification, arms are composed of twenty (was eighteen before) slabs each with dimensions 400×71 mm^2 and 20 mm thick. This modification required an adjustment of the supporting frame. The proper time resolution of the slabs is about 100 ps. The improved resolution obtained is mainly due to changes in the front-end electronics and signal cables. In the old setup, the readout electronics was installed in the electronic room and was connected to the detector by 36 meter coaxial cables, whereas the new electronics is installed in the vicinity of the detector and cable length is of the order of ~ 2 meters. See Chap. 6 for details about the electronics. The efficiency of the vertical hodoscope is 0.99. A general view of one arm of hodoscope is presented in Fig. 5.3.

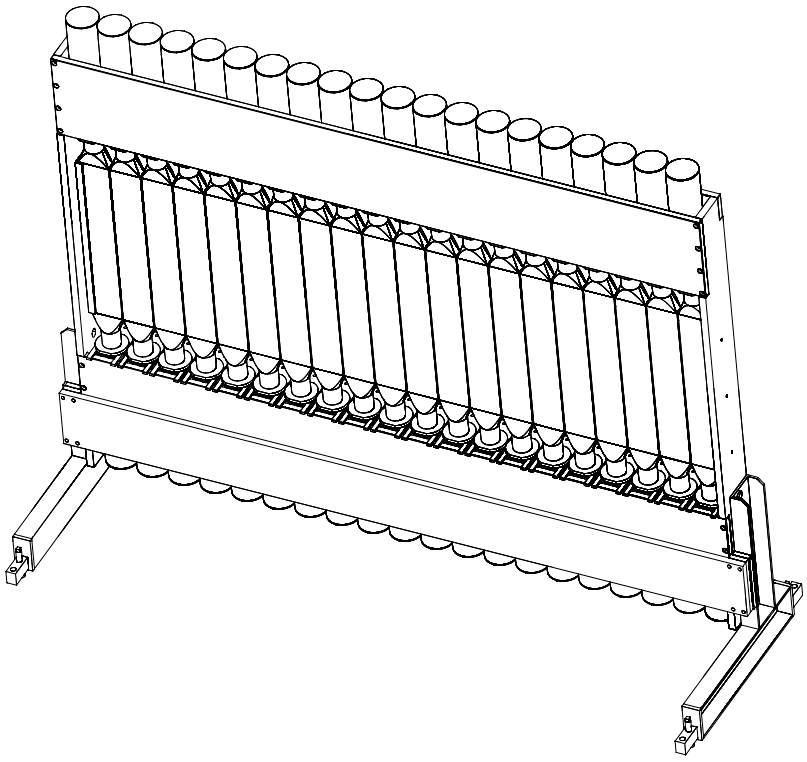

Figure 5.3 General layout of the vertical hodoscope

5.2.2 Time resolution

The time resolution of the vertical hodoscope was obtained from sigma value of Gaussian fit to the distribution of the time difference in two VHs in left and right arms for all e+e− pairs. For each scintillator block, the timings of the signals from two ends are averaged to remove the dependence on the hit position in a scintillator block. Pulse-height (walk) corrections are also carried out. The result is shown in Fig. 5.4

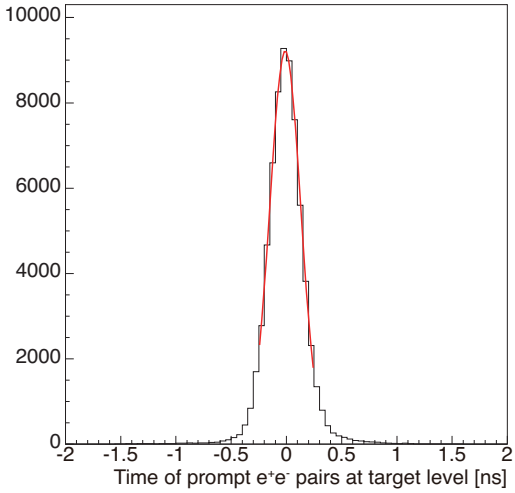

Fig. 5.4 Time difference between the positron and the electron ($t_{left} - t_{right}$) fitted.

The sigma value obtained was then divided by $\sqrt{2}$, since one can assume that two hodoscopes are almost identical and the two uncertainties are not correlated. The time resolutions finally obtained are, 112 ps in the 2008 data, and 113 ps in the 2010 data.

5.3 Horizontal hodoscope

5.3.1 Construction and performance

A couple of Horizontal Hodoscopes (HH) are placed downstream of VH. They were updated also for the same reason as for VH. After the modification, the effective area of the detector in one arm is now 1500×400 mm^2 (1300×400 mm^2 before). The distance of HH to the target is 11.7 m. In HH the modules are rotated by 90 degrees with respect to VH. Therefore to increase the surface, it was necessary to replace all the scintillating slabs with new and longer ones, the number of slabs being kept. A new type of plastic scintillator was used in the modified hodoscope. The former one was extrusion type custom made (in IHEP, Protvino), but this time, BC-408 from Saint Gobain Crystals is used.

The light guides and PM houses were modified to keep the overall length of the detector unchanged, although the active length has been increased by 200 mm. A modification of the support frame was also needed as in the case of VH. The value of the base resistor in the divider was increased in order to decrease the heating of the divider and also additional power supplies for the last three dynodes were used for the compensation of base current decrease. For the photomultiplier, PM XP-2008 was used. Sixty-four photomultipliers were selected from a few hundreds to choose samples with best gain and quantum efficiency. The proper time resolution of slab is about 211 ps.

An improvement of time resolution compared to that before the modification was made possible in the same manner as VH, namely a new readout electronics and short cables between detector and electronics. The efficiency of hodoscope was about 98% in 2008 [JED11] and was slightly decreased up to 2012. A general view of hodoscope is presented in Fig. 5.5.

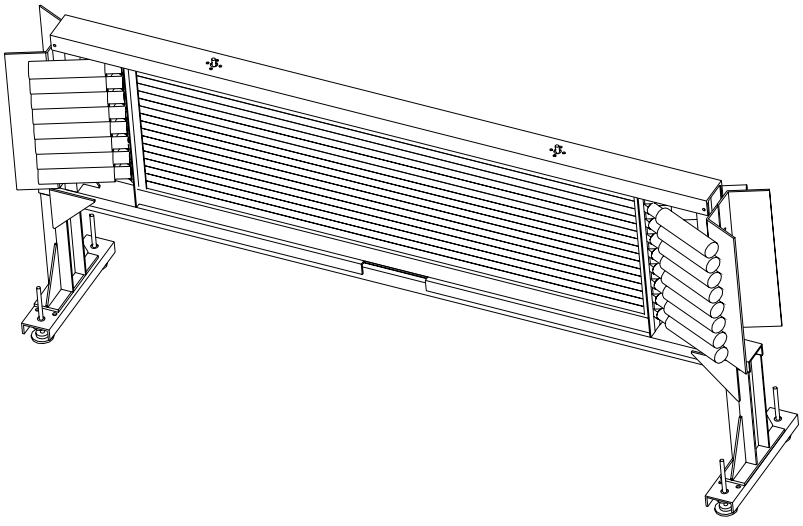

Figure 5.5 General layout of the horizontal hodoscope

5.3.2 Time resolution and amplitude analysis

For the e^+e^- pairs the detected time difference recorded between two HH's placed in 2 arms is shown in Fig. 5.6.

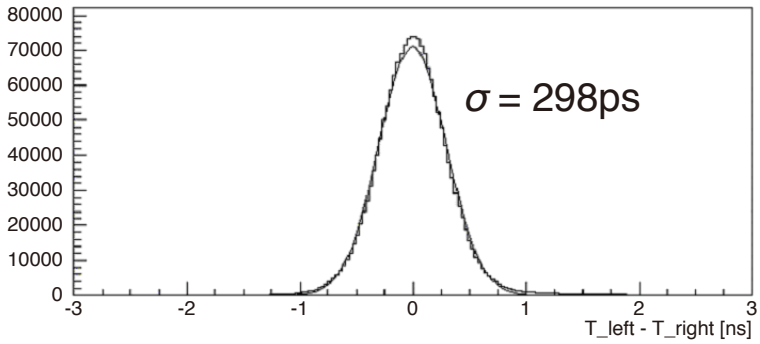

Fig. 5.6 Difference between times measured by left and right horizontal hodoscopes

In this measurement, timings of the signals read out from two ends of a long block are averaged. As a first approximation, this takes care of the hit-position dependence of the timing obtained, since light propagation velocity is almost constant and uniform in all the modules. Also, as F1-TDC-ADC is essentially a leading-edge discriminator, the timing recorded depends on the pulse-height of the signal (walk), but this can be corrected as the pulse heights are recorded at the same time. The time difference spectrum shown in Fig. 5.6 was obtained after these corrections.

This peak was fitted with a single Gaussian, and it gave a standard deviation of 298 ps.

Assuming that two HH are quasi-identical and the timing uncertainties involved in the measurement of timings on the two HH's are independent, one can obtain the intrinsic time resolution of HH by dividing this value by $\sqrt{2}$, which gives 211 ps.

The light propagation in each module (block) in HH is slightly different and also it is not uniform. Thus we further tried to improve the timing by correcting the difference in light propagation in each module. However, the improvement was rather negligible. Thus in the final data analysis, this sophisticated correction is not taken into account.

Also an estimation of 'effective number of photoelectrons' was performed for each slab in HH. The result is presented in table 5.1.

Slab	Left	Right
1	149	134
2	119	124
3	114	137
4	76	137
5	158	162
6	140	125
7	140	124
8	140	138
9	117	136
10	141	160
11	161	152
12	135	147
13	155	147
14	107	152
15	131	141
16	159	139

Table 5.1 Approximate effective numbers of photoelectrons obtained as a square of ratio of the position to the width of amplitude peaks.

5.4 Cerenkov counters

For the added detection of $\pi^+ K^-$ and $\pi^- K^+$ pairs the DIRAC identification system of charged particles was modified.

In addition to the existing gas threshold Cerenkov detectors filled with N_2 gas (to detect electrons and positrons, n =1.00029) there were installed threshold Cerenkov detectors with aerogel (n =1.015 and n =1.008) and with a heavy gas C_4F_{10} (n =1.0014). Downstream detectors for particle identification in addition to the 3 Cerenkov counters are a preshower detector (PSh) and a muon counter (MU).

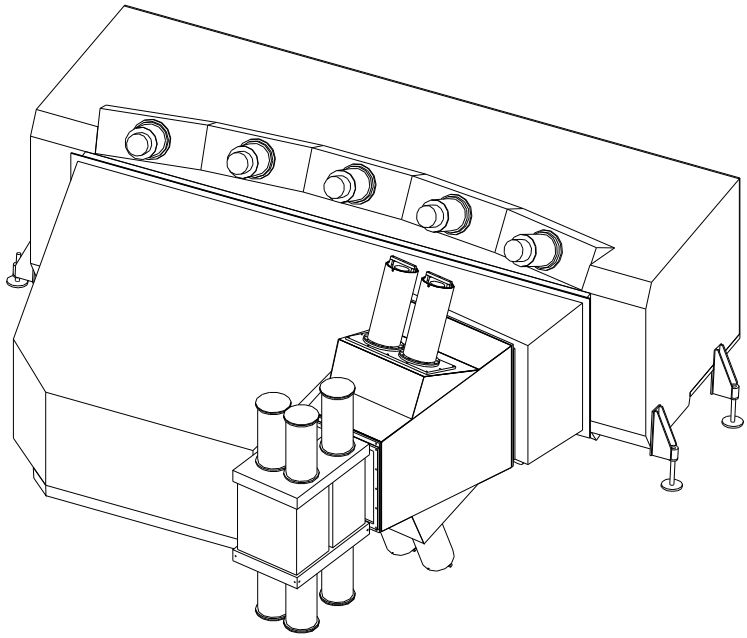

Fig. 5.7 Set up of the Cerenkov counters

The nitrogen Cerenkov detectors detect only electrons. These detectors have been modified to make space for the new Cerenkov detectors (aerogel and C4F10).

Fig. 5.8 shows the speeds of particles (electrons-positrons, pions, kaons and protons) in the range of momentum of each particle accepted by the spectrometer. Also are shown the speeds at which the N_2, heavy-gas (C4F10), aerogel with n = 1.008 and aerogel with n = 1.015 start emitting light.

Thus C4F10 detects electrons and large-momentum pions. Only large-momentum kaons are detected by Aerogel counters. Protons are below threshold for Cerenkov radiation in N_2, C4F10 and aerogel counter with with n = 1.008 detectors.

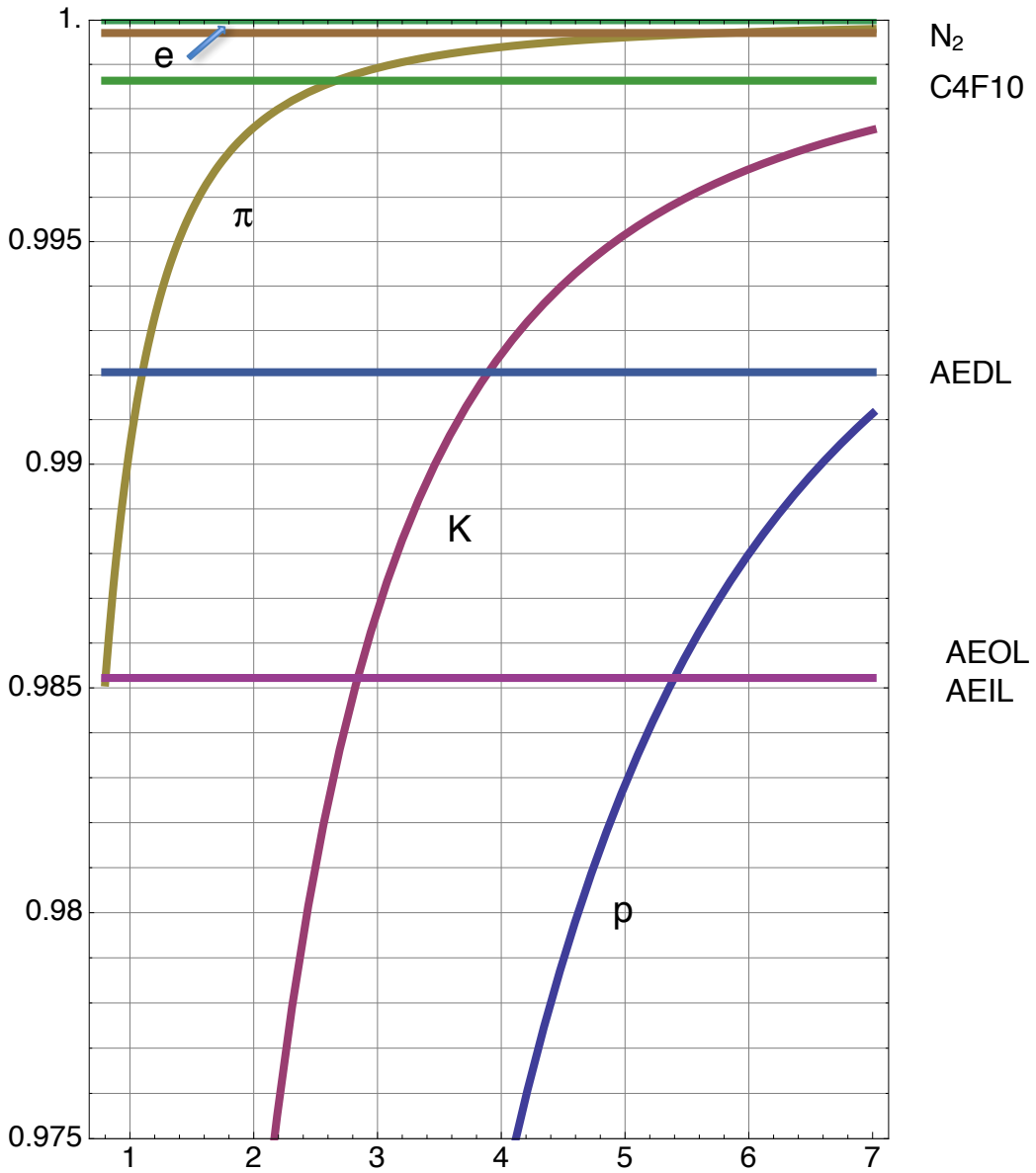

Fig. 5.8 The speed of particles (electrons-positrons, pions, kaons and protons) in the range of momentum (GeV/*c*) of each particle accepted by the spectrometer. Also are shown the speeds at which the N_2, heavy-gas, aerogel with n = 1.008 and aerogel with n = 1.015 start emitting light (horizontal lines).

Since the momentum of πK atoms is in the range of 5 to 9 GeV/c, the momentum of the kaons arising from the atoms is larger than 3.9 GeV/c in lab system.

5.4.1 Aerogel Cerenkov counter

5.4.1.1 Construction

A new aerogel Cerenkov counter with two indices of refraction (Figs. 5.9, 5.10) was installed for separation of kaons from protons in a large momentum range.

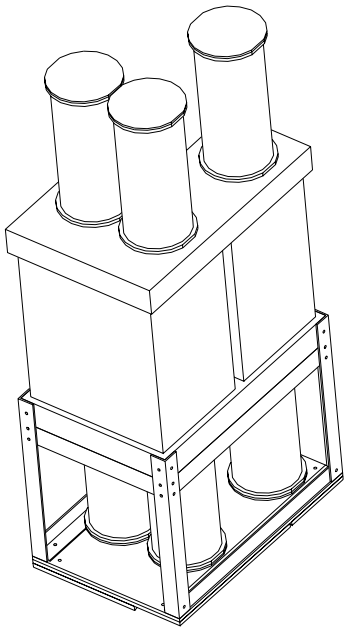

Fig. 5.9 Aerogel Cerenkov counter - Support

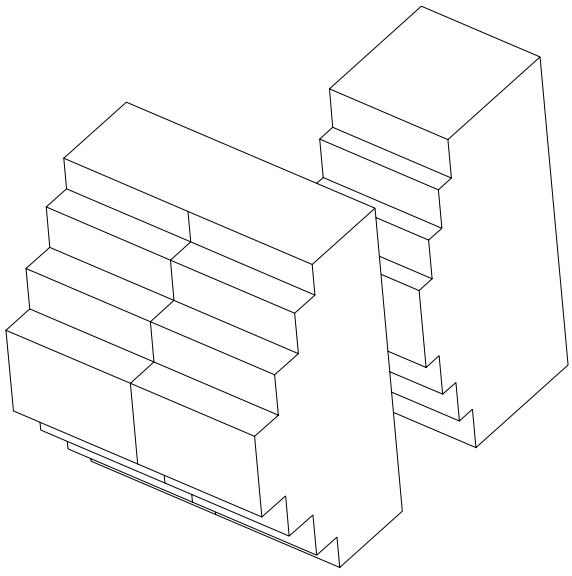

Fig. 5.10 Aerogel Cerenkov radiators

The detector separates kaons from protons in the left arm [ALL07A, ALL07B]. Such a detector is required only in the left arm since the contamination from antiprotons in the right arm is small due to their low production rate.

The detector consists of three modules having identical geometry. The low-momentum modules (AEIL and AEOL) cover the momentum range of 4 - 5.5 GeV/c with a refractive index n =1.015 of aerogel radiators. The high momentum module (AEDL) with n =1.008 is overlapping with the module AEIL to cover the momentum range of 5.5 -

8 GeV/c in the inner half of the acceptance.

The sensitive area of AEIL+AEOL is 333×417 mm^2 (W × H) and that of AEDL is 159×427 mm^2 (W × H). The thickness of the modules is between 11 cm (on the top and bottom) and 23 cm (in the center).

We chose the aerogel with n =1.008 from the Budker Institute for Nuclear Physics (BINP) associated to the Boreskov Institute of Catalysis (BIC) in Novosibirsk and the one with n =1.015 from Matsushita (Panasonic) Electric Works (MEW) Ltd. in Japan.

To compensate the strong position dependence of the light yield, aerogel tiles are added at the centre of the detector forming a unique pyramidal shape.

The sensitive area of AEIL+AEOL is 33 × 42 cm^2 (W × H), L = 11 - 23 cm. The sensitive area of AEDL is 16×42 cm^2 (W × H), L=16 - 23 cm.

A three-layer wavelength shifter (WLS) is implemented in the AEDL module to increase the collection and detection efficiency for UV light. Tetratex reflector foils coated with WLS and layers of aerogel radiator are alternately stacked in the direction of incident particles. The best results were obtained with p-terphenyl giving a 50% increase in light yield.

The light is collected from the top and bottom by six 5-inch PMs Photonis XP4570/B with UV-glass window. The typical quantum efficiency of the bialkali photocathodes of the PMTs reaches a maximum value of 20-25% in the blue region around 420 nm.

The average number of detected photoelectrons is N_{pe} =7 and 4 for heavy and light modules, respectively ($\beta = 1$). The signal uniformity is within ±10%. Table 5.2 summarizes the specifications of the aerogels used in this work.

Table 5.2 Specification of the aerogels used in this work.

n	Unit tile	Scattering length	Absorption lengths	
	mm^3	mm at 400 nm	cm at 270 nm	cm at 350 nm
BIC 1.008	53×53×23.3	>40	~10	~300
MEW 1.015	111×111×10.5	>30	~5	~40

5.4.1.2 Performance

The response of the counters to the kaons was evaluated using the experimental information about the response to the pions having the same momentum (but different velocity). This procedure is justified since the emission of the Cerenkov light is determined only by the velocity, and not dependent on the kind of particle. The geometrical condition is the same for pions and kaons for a given velocity.

This procedure is also applied to protons, and we have seen that the experimental response to the protons is correctly reproduced. Fig. 5.11 shows the detection efficiency of kaons for the 3 detectors as a function of the kaon momentum.

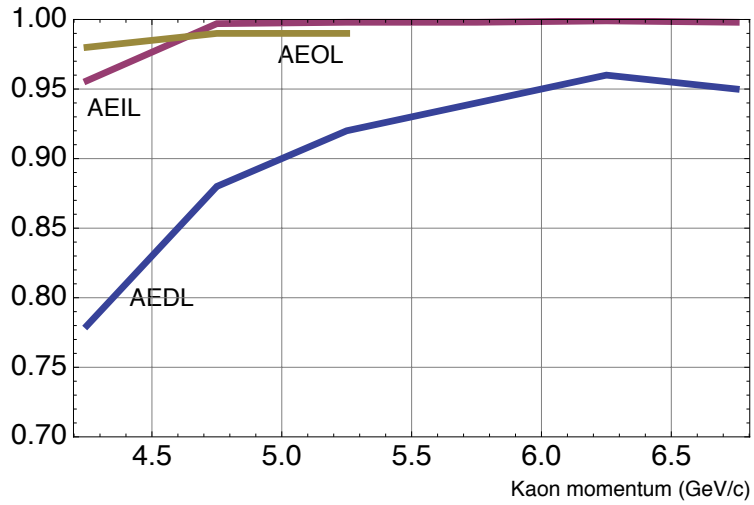

Fig. 5.11 K detection efficiency of the 3 aerogel counters as function of the K momentum when the threshold is set to $N_{pe} = 1$.

To evaluate the efficiency of the 3 aerogel counters for the detection of protons, protons coming from the lambda decay were used. The result is shown in Fig. 5.12. The counter AEOL is situated far from the central axis of the spectrometer, thus no protons with high momenta (>5.3 GeV/c) hit this counter. Therefore, the proton detection efficiency was evaluated only in the proton momentum range of 4 – 5.3 GeV/c for the AEOL counter. The protons start emitting light at 5.4 GeV/c theoretically when the refractive index = 1.015 (AEIL and AEOL). In reality one observes that the detection efficiency rises at the threshold momentum. As for AEDL with refractive index = 1.008, protons should emit light above 7.4 GeV/c. In reality one observes no change in the efficiency in this counter.

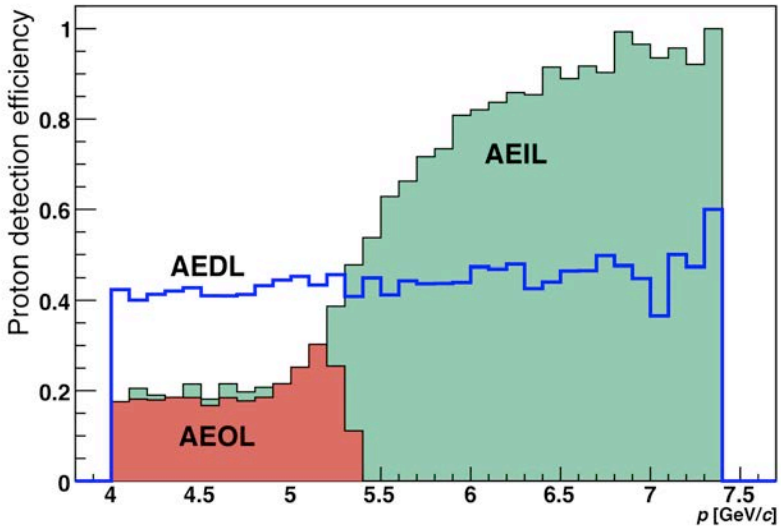

Fig. 5.12 Proton detection efficiency of the 3 aerogel counters as function of the proton momentum when the threshold is set to $N_{pe} = 1$.

These 3 counters were installed in 2007, and used for the analysis of 2007 and 2008 data. In the end of that period, a deterioration of the performance was observed and the data were not used in the period after 2008.

5.4.2 Heavy-gas Cerenkov counter (C4F10)

5.4.2.1 General description

The Heavy Gas Cerenkov Detector, C4F10 was redesigned for the upgraded DIRAC setup. It is one of the two new detectors (the other one is Aerogel Cerenkov) constructed especially for the new DIRAC setup to obtain the possibility of pion-kaon pair identification. The Heavy Gas Cerenkov Detector C4F10 is placed downstream of Horizontal Hodoscope (in the left arm, the aerogel Cerenkov counter is placed in-between) in the space which became available after cutting the Nitrogen Cerenkov. The main role of C4F10 is the pion/kaon separation in the high-momentum region. Protons and kaons are identified by their time-of-flight in addition to the Cerenkov counters.

As kaons from the decay of the πK atoms in the DIRAC setup geometry have momentum range of 4 - 8 GeV/c, it is enough to cover with C4F10 only part of the full aperture as shown in Fig. 5.7. Perfluorobutane (C_4F_{10}) with a refractive index $n = 1.00137$ (for the wavelength of 300 nm under normal conditions) was chosen as Cerenkov radiator. It is sufficient to be above the threshold for the whole momentum range. The optical system is composed of four spherical and four flat mirrors (Fig. 5.13) [KUP08, HOR08]. The use of this scheme has enabled to decrease the size of the detector compared to only one mirror scheme, which is very important as it is necessary to accommodate the detector in the current geometry of the setup. The alignment of the optics with a laser was executed before the installation in the beam line [BRE08A]. Five-inch photomultipliers HAMAMATSU H6528 with UV-glass are used as photo-detectors.

A closed recirculation scheme was chosen for C_4F_{10} as it is rather expensive and not readily available [HOR08]. The circuit of recirculating–recovery system is schematically shown in Fig. 5.15. To minimize gas losses during operation of the system, the pressure was maintained at 1 - 2 mbar below atmospheric pressure. The typical amplitude spectrum of the signal produced by pions is shown in Fig. 5.16. The average number of photoelectrons is about 25.

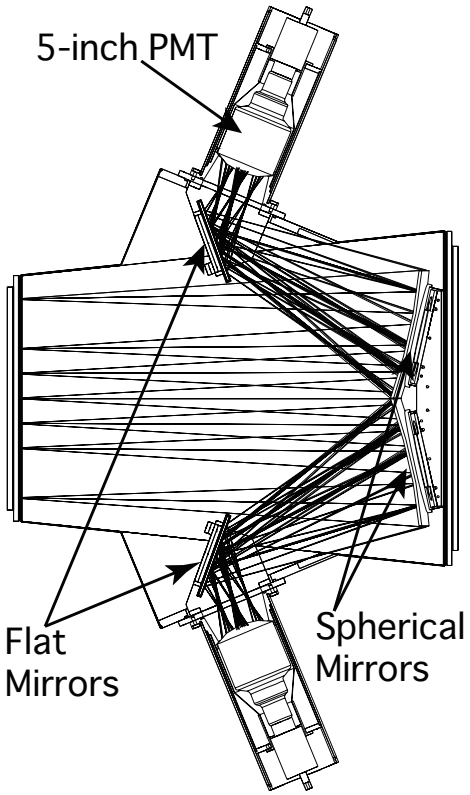

Figure 5.13 The optical system of Heavy Gas Cerenkov Detector C4F10

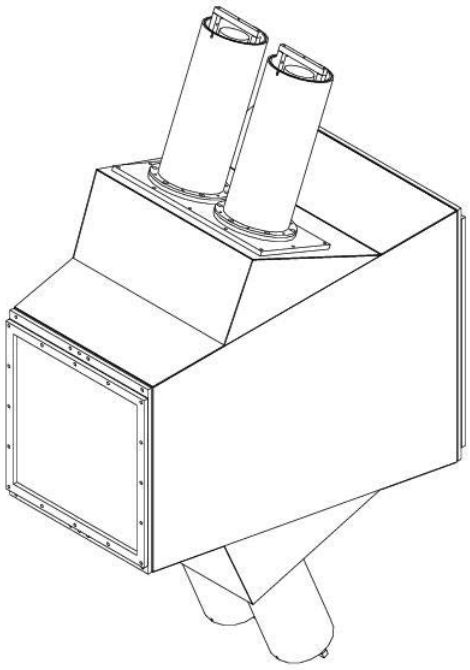

Figure 5.14 General layout of Heavy Gas Cerenkov Detector C4F10

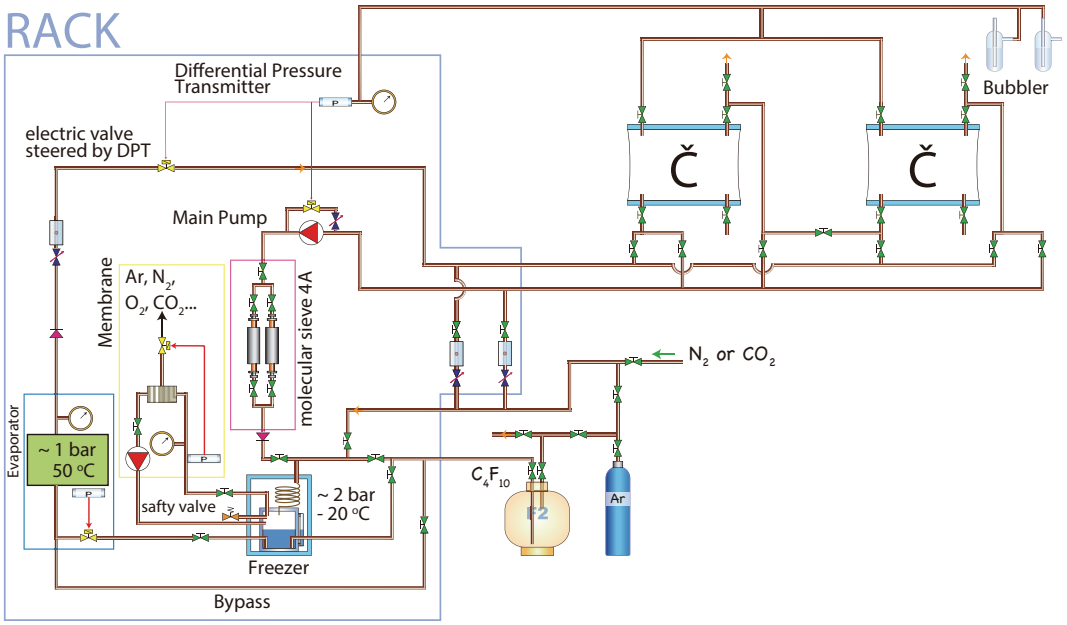

Figure 5.15 Heavy Gas Cerenkov Detector C4F10 gas recirculating–recovery system

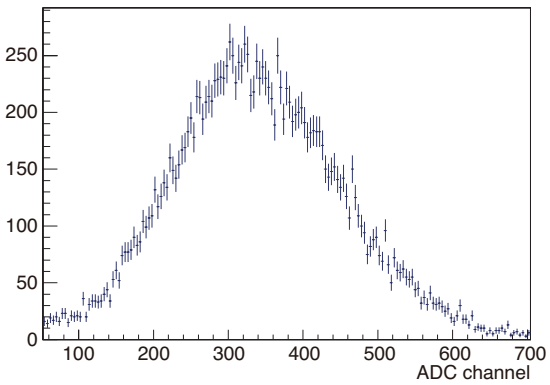

Fig. 5.16 Typical amplitude spectrum of the signal produced by pions

5.4.2.2 Detection efficiency

The estimation of the efficiency of the Heavy-gas Cerenkov counter C4F10 is very important for the analysis of events with momentum greater than 3 GeV/*c*.

The "pion efficiency" is basically the ratio between number of detected pions and that of all pions that cross the C4F10. The method has a momentum limitation at 5 GeV/c. So the C4F10 efficiency is studied only in the interval between 3 and 5 GeV/c (the counter detects particles above 3 GeV/c), which is divided into 10 parts with a width of 200 MeV/c. The analysis is made for each part separately. Detected and non-detected particles are determined by the C4F10 pulse-height and the time-of-flight between VH and C4F10. The identification of the detected pions is done by the help of the time-of-flight.

The exercise to find the efficiency was performed separately for the π^+ and the π^-. The results obtained about the efficiency for individual momentum intervals are summarized in Table 5.3 (π^+) and in Table 5.4 (π^-) .

From these two tables it is seen that the pion efficiency of the counter for 2010 considerably depends on momentum. The efficiency varies between 45-98% as momentum changes. The lowest efficiency is for the lowest momentum interval (i.e. P=(3000,3200) MeV/c) and afterwards grows almost till 98% in highest momentum intervals. As seen in Figs. 5.17 and 5.18, values for amplitude conditions (pions are identified with ADC) are a little lower than for time conditions (pions are identified with TDC). The reason comes from the electronics. The cause is that if a signal appears in the counter, the time information is always present but the amplitude may not be.

The next thing that is clear is that the efficiency for the negative arm is higher and smoother than for the positive arm. This can be caused by the fact that the number of negative particles is smaller than for positive ones and, thus, the dead time of electronics is for the negative arm lower than for the positive ones.

Table 5.3 The π^+ efficiency for both type of conditions depending on momenta intervals with statistic error.

Mom. intervals [MeV/c]	Ampl.conditions eff[%]	Time conditions eff[%]
3000-3200	43.2 ± 3.3	44.6 ± 3.4
3200-3400	58.1 ± 4.2	60.0 ± 4.3
3400-3600	65.6 ± 4.7	71.4 ± 4.8
3600-3800	74.4 ± 5.1	74.1 ± 4.9
3800-4000	90.3 ± 5.5	91.8 ± 5.5
4000-4200	93.3 ± 5.6	94.6 ± 5.6
4200-4400	93.4 ± 5.8	93.0 ± 5.7
4400-4600	93.4 ± 5.8	94.5 ± 5.8
4600-4800	93.4 ± 6.0	92.9 ± 6.0
4800-5000	94.1 ± 6.2	96.2 ± 6.0

Table 5.4 The π^- efficiency for both type of conditions depending on momenta intervals with statistic error.

Mom. intervals [MeV/c]	Ampl.conditions eff[%]	Time conditions eff[%]
3000-3200	42.0 ± 3.3	46.6 ± 3.5
3200-3400	58.0 ± 4.2	57.4 ± 4.2
3400-3600	72.4 ± 4.9	73.5 ± 4.9
3600-3800	85.1 ± 5.4	85.3 ± 5.3
3800-4000	92.1 ± 5.5	94.9 ± 5.5
4000-4200	96.5 ± 5.6	96.5 ± 5.5
4200-4400	96.7 ± 5.6	97.1 ± 5.5
4400-4600	96.7 ± 5.6	98.2 ± 5.5
4600-4800	96.8 ± 5.7	97.1 ± 5.7
4800-5000	96.1 ± 5.8	96.1 ± 5.8

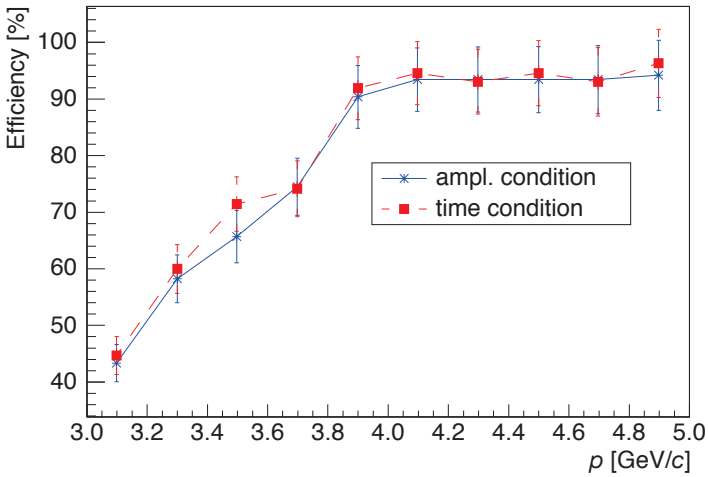

Figure 5.17 The CHF efficiency dependence on momentum for the positive arm with statistic error.

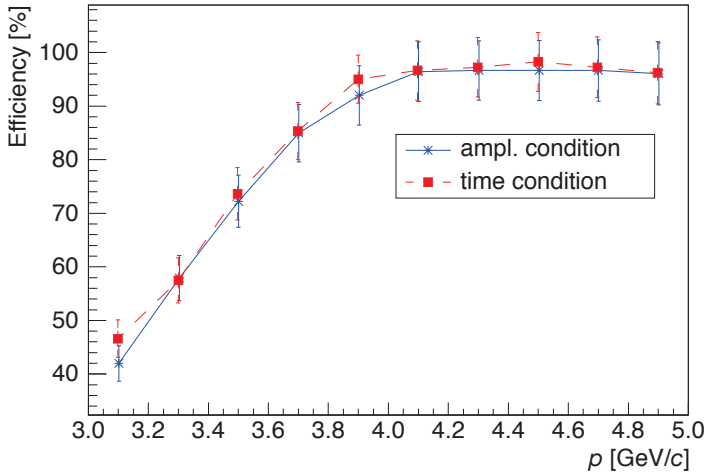

Figure 5.18 The CHF efficiency dependence on momentum for the negative arm with statistic error

5.4.3 Nitrogen Cerenkov Counter

5.4.3.1 General description

The old N_2 Cerenkov counters have been modified to permit insertion of the new heavy gas (C4F10) and aerogel Cerenkov detectors in the region of the kaon trajectories (see Fig. 5.7). Therefore, in this region the electron rejection efficiency of the N_2 Cerenkov detectors becomes smaller due to a smaller path length.

The N_2 Cerenkov detectors are used for rejection of the large e^+e^- background in $\pi^+\pi^-$ and πK pairs detection. They consist of two identical threshold Cerenkov counters [BRA99], each for one spectrometer arm (see Fig. 2.2).

One counter is equipped with 10 photomultipliers, 5 upside and 5 downside and 20 mirrors. Cerenkov light reflected by pairs of adjacent mirrors is focused onto the same photomultiplier.

The N_2 gas radiator is used at normal temperature and pressure. These conditions determine particle momentum threshold values $p^e_{thres} = 20.3 MeV/c$ and $p^\pi_{thres} = 5.5 GeV/c$.

The N_2 Cerenkov sensitive volume has been cut in the kaon trajectory region to permit insertion of the C4F10 for pion identification and aerogel Cerenkov detector for kaon identification (see Fig. 5.7). Consequently, the counter length is 285 cm in the pion flight region ("long part") and 140 cm in the kaon flight region ("short part"). The Cerenkov process produces photons in proportion to the primary particle path length in the sensitive region.

The N_2 at atmospheric pressure has the refractive index $n = 1.000298$ and the number of photons produced per unit length $dN_\gamma / dx = 780\,(n\text{-}1) \approx 0.23$ photons/cm. So, in the "long part" we can have ~65 photons and in the "short part" ~32 photons.

The analog signals from individual PMT of each arm are fed into LeCroy 4300B ADC units and are used to perform overall amplitude alignment. At the same time, the individual signals from 10 PMT's are fed into a custom-made summing module, which gives at the output a linear sum signal, fed into another LeCroy 4300B ADC unit (indexed as signal 11 for the left arm and 22 for the right arm).

5.4.3.2 Performance

Typical ADC Cerenkov spectra are presented in Fig. 5.19. Fig. 5.19*a* shows the ChN1 ADC spectrum from the "short part", and Fig. 5.19*b* shows the ChN7 ADC spectrum from the "long part" of the left arm, both taken with e^+e^- trigger. Similar spectra are for the right arm.

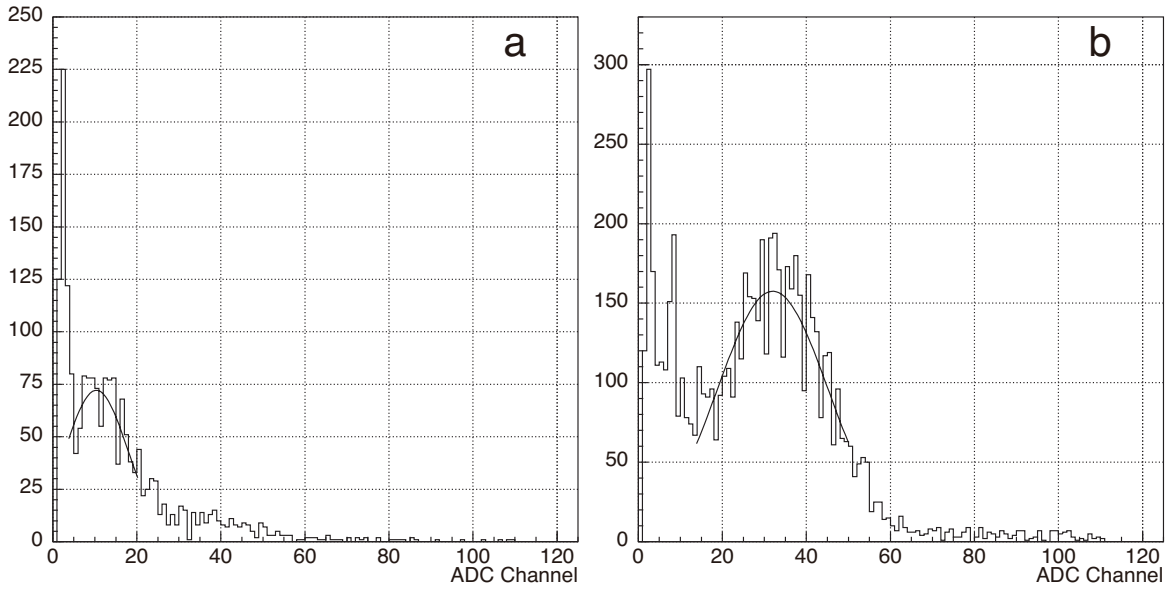

Figure 5.19 The N_2 Cerenkov ADC spectra taken from individual PMT of the left arm. ChN1 spectrum of the "short part" – contribution of ~ 2 photoelectrons. ChN7 spectrum of the "long part" – contribution of ~ 6 photoelectrons.

Table 5.5 Estimated numbers of collected photoelectrons

	Left arm					Right arm				
PMT	5	4	3	2	1	16	15	14	13	12
N_{pe}	3.32	4.77	6.58	0.28	1.91	0.84	1.44	6.72	4.36	5.84
PMT	6	7	8	9	10	17	18	19	20	21
N_{pe}	3.18	5.85	8.08	3.57	2.28	2.62	1.73	6.62	4.93	3.23

The analysis of individual ADC spectra gives the mean number of photoelectrons (N_{pe}) reaching the first dynode for each PMT, $N_{pe}=(\mu/\sigma)^2$ (see Table 5.5). The relative position of the Cerenkov and Preshower PMT's is shown in Fig. 5.20, for the left arm elements.

In the "short part" of the N_2 Cerenkov detector, PMT 1, 2, 9, 10 (left arm) and 15, 16, 17, 18 (right arm), the numbers of photoelectrons are smaller due to the small number of the produced Cerenkov photons. Therefore the ADC distribution has a small mean value and a small width (see for example ChN1 Fig. 5.19a) due to a small number of photoelectrons contribution.

Based on the data in Table 5.5, the mean number of photoelectrons for the "long part" is $\left\langle N_{pe}^{long} \right\rangle = 5.3$ and the number of photoelectrons for "short part" is $\left\langle N_{pe}^{short} \right\rangle = 1.83$.

Then the *electron rejection efficiency* for the "long part" is ~99.5% and for the "short part" is ~85%.

The high energy pions (momenta above the threshold value $p_{thres}^{\pi} = 5.5 GeV/c$) and accidental coincidences occurring within the trigger time-gate are labelled as "electron" by Cerenkov signals. The Preshower detectors can separate the pion and electron signals in these "electron" spectra (see the next section) and permit the evaluation of the Cerenkov *pion contamination*.

5.5 Preshower detectors

5.5.1 General description

Preshower detector [PEN09] samples the early part (1-6X_0) of the electron shower, before the pion shower is initiated. Therefore the preshower detector has a high amplitude distribution for electrons and a low amplitude one for pions. This provides with an electron/pion separation possibility.

The new preshower detector [PEN11] for DIRAC-II experiment has been extended to include the phase space of the kaon flight region. To improve the smaller electron rejection efficiency of the Nitrogen Cerenkov in this region, the preshower detector has been built with two layers.

The geometrical characteristics of the preshower detector for DIRAC-II [PEN11] are presented in Fig. 5.20. It contains, as first layer a Pb converter of 10 *mm* thick for the first two slabs and a 25*mm* one for the rest. The second layer is placed behind the first one in the kaon flight region. It contains Pb converter slabs of 10*mm* thickness. The detector slabs, placed behind the Pb converters, are plastic scintillators BICRON type 408 of 750 *mm* high, 10 *mm* thick and 350 *mm* or 175 *mm* wide.

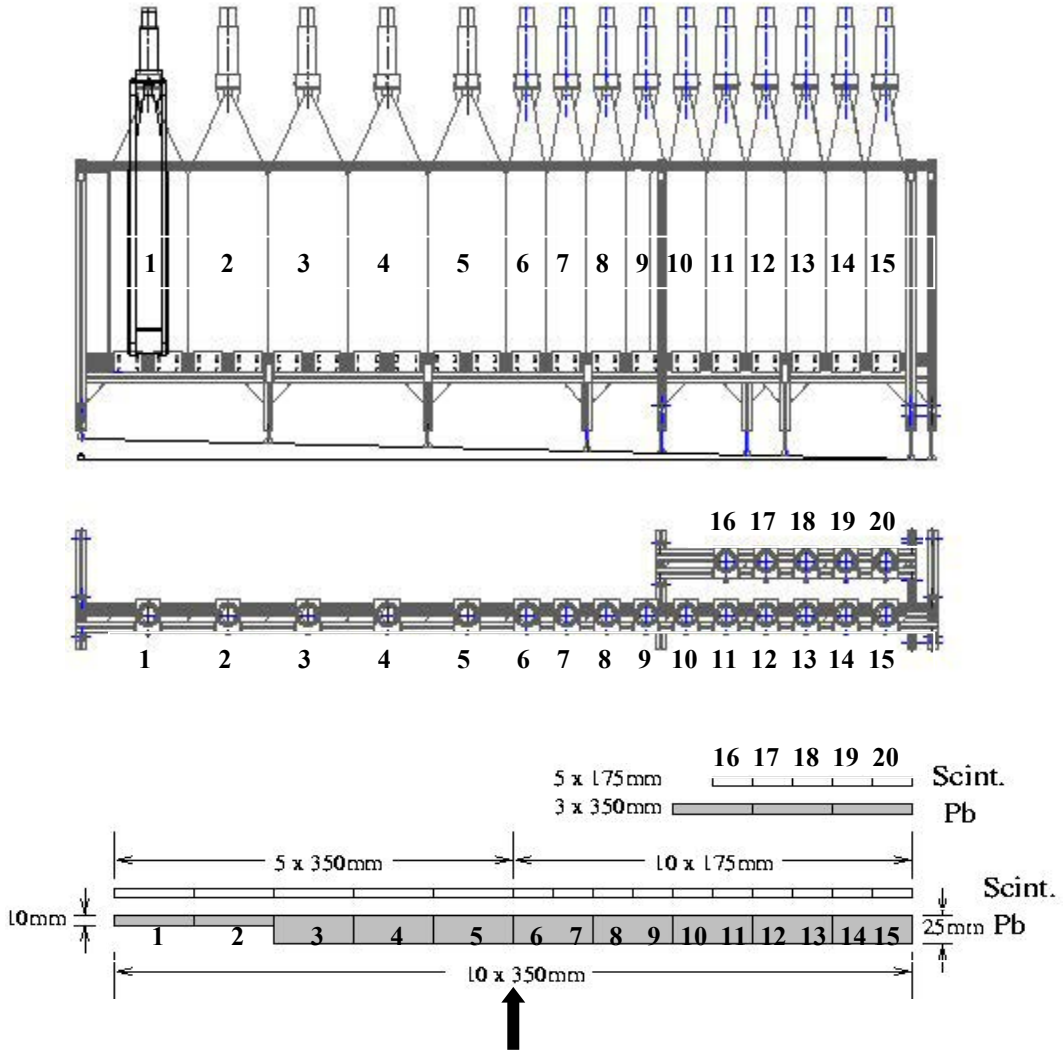

Fig. 5.20 The preshower left arm geometry and structure.

5.5.2 Efficiencies

a. One layer preshower

The characteristic preshower amplitude spectra are presented in Fig. 5.21. The position of the pion peak (the left-most peak in Fig. 5.21) is practically unchanged with the energy (as minimum ionizing particle), but the electron distribution is moving to larger amplitudes at higher energies.

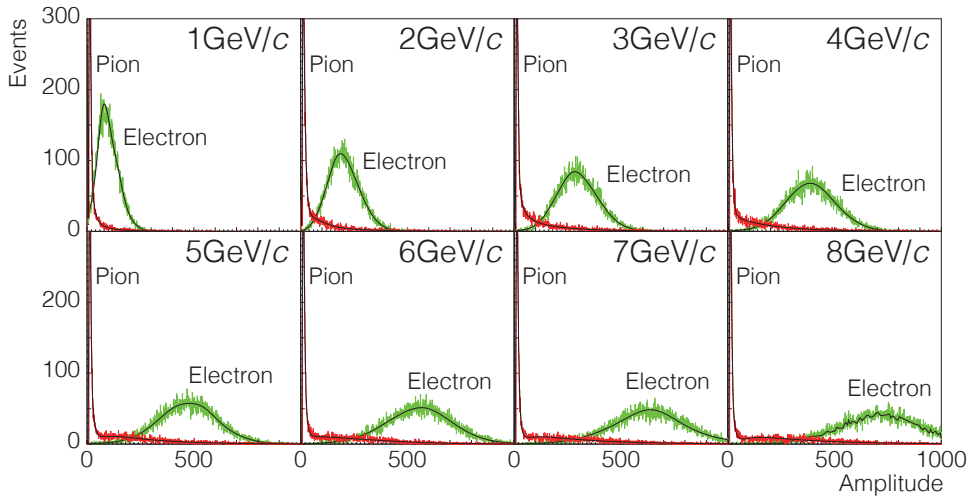

Fig. 5.21 Preshower simulation of the pion and electron amplitude distribution.

The preshower amplitude spectra have been measured in the DIRAC setup for both pion and electron triggers, and for all preshower detector slabs. Typical experimental spectra, for pions and electrons at intermediate energies, are presented in Figs. 5.22, 5.23, and 5.24 for slabs number 4, 9 and 13 of the right arm (negative particles). They are obtained, respectively, in anticoincidence and coincidence with the Nitrogen Cerenkov detector.

The "cut channel" separates the pion and electron amplitudes (see Fig. 5.22). It is used to determine the number of events A_1 and A_2 ($A_{tot}=A_1+A_2$), thus to define the ratios $\pi_{eff} = A^{\pi}_1/A^{\pi}_{tot}$ (pion detection efficiency, see Fig. 5.25) and $\pi_{loss} = A^{\pi}_2/A^{\pi}_{tot}$ (pion loss) in the pion spectra, as well as $\epsilon_{esc} = A^{el}_1/A^{el}_{tot}$ (electron escape) and $\epsilon_{rej} = A^{el}_2/A^{el}_{tot}$ (electron rejection, see Fig. 5.24) in the electron spectra. The channel position of the cut has been determined by a Gaussian fit to the pion peak, and set at 7σ above the peak to accommodate the Landau tail.

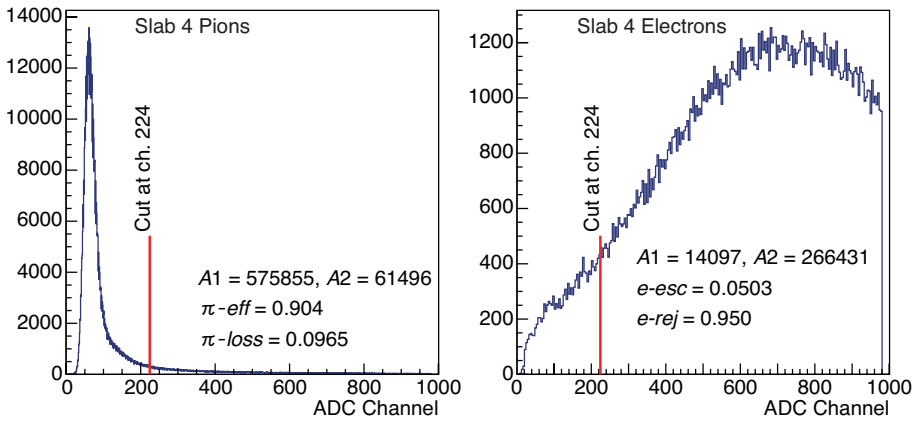

Fig. 5.22 Preshower pion and electron spectra, slab 4, right arm

As the energy increases (higher slab number), some pion signals are also present in the electron spectra (see Fig. 5.23-5.24) due to higher energy pions, which produce Cerenkov radiation. Therefore the Cerenkov detector cannot separate effectively high energy electrons and pions. The PSh electron spectra are contaminated with pions. The pion signals can be rejected in the analysis of the PSh electron spectra and a higher overall electron rejection for DIRAC experiment can be obtained (see Fig. 5.26).

The lower rejection efficiency ϵ_{rej} and pion efficiency π_{eff} in the outermost slabs 1, 15 and 20, are due to the fact that these slabs are partially out of the particle beam. The small number of hits in these slabs is the reason for the uncertainties larger than for other slabs. Apart from these values, the electron rejection efficiency of the preshower ϵ_{rej} is greater than 90%.

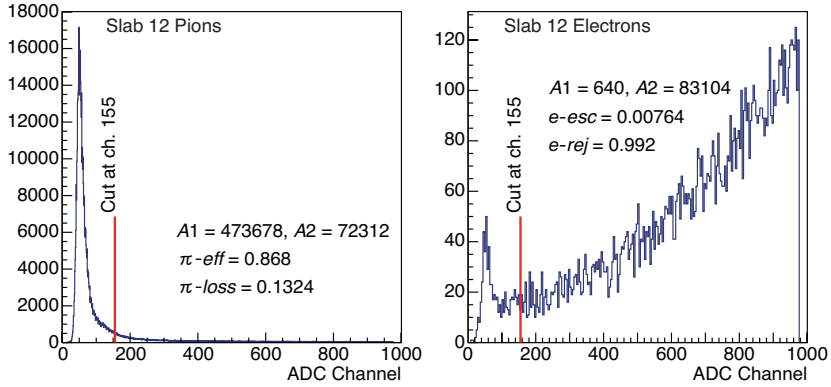

Fig. 5.23 Preshower pion and electron spectra, slab 9, right arm

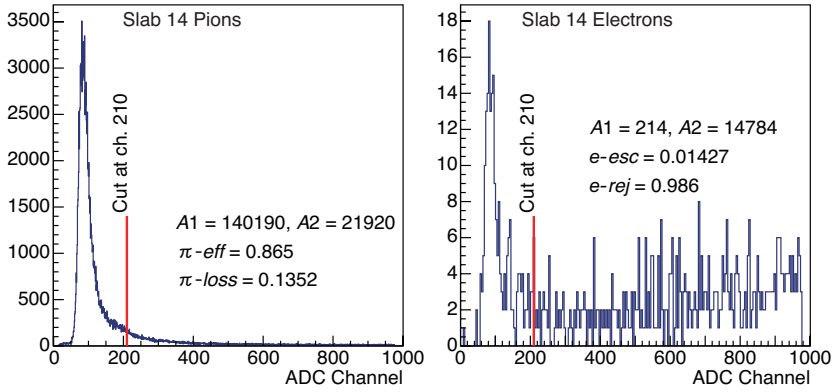

Fig. 5.24 Preshower pion and electron spectra, slab 13, right arm

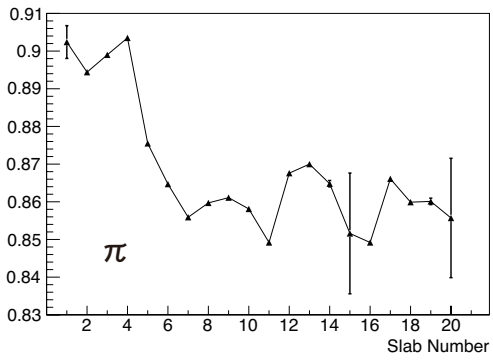

Fig. 5.25 One layer preshower pion detection efficiency (right arm)

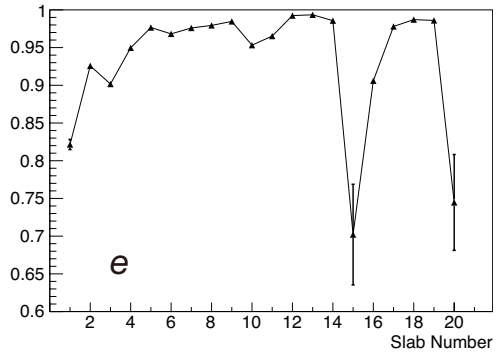

Fig. 5.26 One layer preshower electron rejection efficiency (right arm)

b. Two layer preshower

To increase the preshower detection efficiency, a new layer has been added in the region of kaon phase space where the Cerenkov efficiency is lower (see Fig. 5.23-5.24). The second layer (II) should detect the pions and electrons that fail to be detected by, or escape from the first layer (I). The second layer processes the high amplitude pions (higher than the cut level) and the low amplitude electrons (lower than the cut level).

Fig. 5.27 shows the pion and electron spectra for the overlapped slab pair 12+17 of the right arm. In Fig. 5.27a, the left spectrum (slab 12) shows the pions registered by the first layer, while the loss pions of the first layer (higher than cut channel) are analysed and plotted in the right spectrum (slab 17 of the second layer). Now the overall *pion detection efficiency* is expressed as:

$$\pi_{\text{eff}} = \pi_{\text{eff-I}} + \pi_{\text{loss-I}} \times \pi_{\text{eff-II}}$$

The two layers *pion detection efficiency* π_{eff} for the slab pairs 1=(11+16), 2=(12+17), 3=(13+18) and 4=(14+19) have been evaluated and plotted in Fig. 5.28. The outermost pairs (15+20) in both arms have not been included in the analysis due to partial hit coverage of the detector surface.

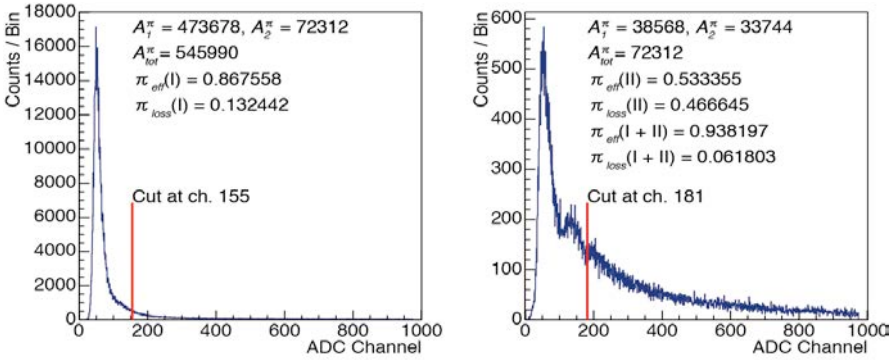

Fig. 5.27a Two-layer right-arm PSh pion spectra in slab 12 (left) and slab 17 (right)

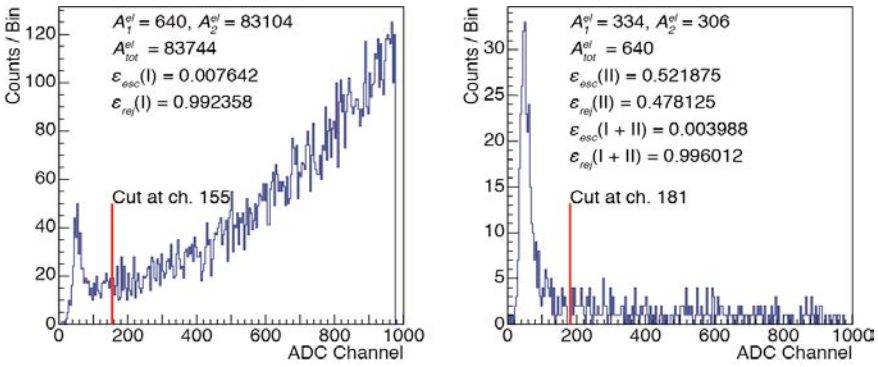

Fig. 5.27b Two-layer right-arm PSh electron spectra in slab 12 (left) and slab 17 (right)

Similarly, in the Fig. 5.27b the left spectrum (slab 12) shows the electrons registered by the first layer, while the escaped electrons from the first layer (lower than cut channel) are analysed and plotted in the right spectrum (slab 17 of the second layer).

Now the overall *electron rejection efficiency* is expressed as:

$$\varepsilon_{\text{rej}} = \varepsilon_{\text{rej-}I} + \varepsilon_{esc\text{-}I} \times \varepsilon_{rej\text{-}II}$$

The two layers *electron rejection efficiency* $\boldsymbol{\epsilon}_{rej}$ for the slab pairs 1=(11+16), 2=(12+17), 3=(13+18) and 4=(14+19) have been evaluated and plotted in Fig. 5.29.

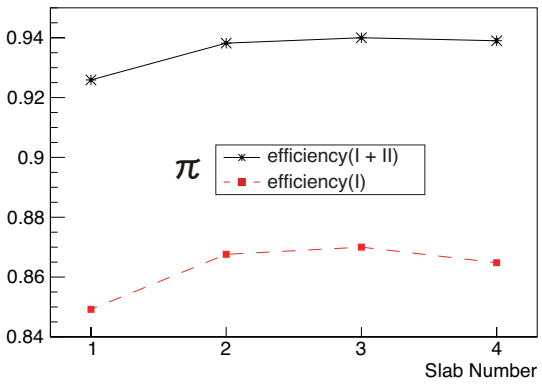

Fig. 5.28 Two layers preshower pion detection efficiency (right arm)

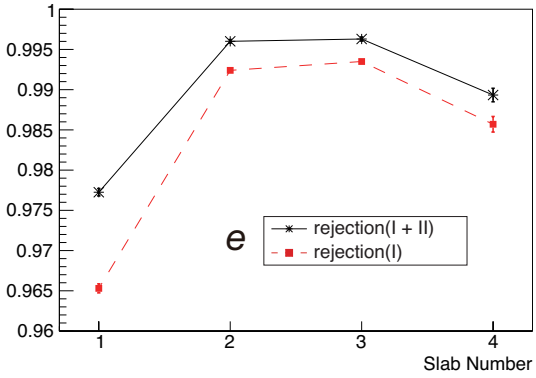

Fig. 5.29 Two layers preshower electron rejection efficiency (right arm)

5.5.3 Electron rejection in DIRAC experiment

In the DIRAC experiment, the observation of the $\pi^+\pi^-$ and $\pi^\pm K^\mp$ atoms and their lifetime measurement is hinged on the observation of "atomic pairs" as an additional peak at small Q (Q<3 MeV/c) submerged in a large background of "Coulomb" pairs (affected by a Coulomb interaction in the final state) and "non-Coulomb" pairs (not affected by a Coulomb interaction in the final state) [ADE11]. Note should be taken that the distribution of "Coulomb" pairs have also a peak at small Q.

The e^+e^- pairs, erroneously identified as hadron pairs, in the Q_T distribution shows a very narrow peak (~1MeV/c). As a result, the e^+e^- background introduces an essential bias to the observation of "atomic pairs". Investigation, presented in the section 5.5.2, shows that the direct rejection of e^+e^- pairs with criteria on the amplitudes observed in the PSh detector leads to essential losses of $\pi^+\pi^-$ ($\pi^\pm K^\mp$) pairs. To prevent it, the next algorithm of e^+e^- background suppression has been developed.

Initially, the PSh spectra are recorded as pion and electron spectra according to the Nitrogen Cerenkov signals. These spectra are contaminated, pions with electrons and electron with pions. The PSh detector removes this contamination.

Fig. 5.30 shows the correlation of the signal from the 4-th slab in the right (negative) and left (positive) arms for the pairs identified as $\pi^+\pi^-$ (a) and e^+e^- (b) by the Nitrogen Cerenkov counter.

Using the cut channel, PSh selects true electrons and pions. This cut, shown by solid line in Fig. 5.30, defines a rectangle at the upper right part. In the low part of the pion spectra (lower than cut channel 250 in Fig. 5.30-left) PSh selects true pions and in the high amplitude part of the electron spectra (higher cut channel 250 in Fig. 5.30-right) PSh selects true electrons.

The same slab pair combination has been done for all the PSh slabs of the left and right arm. So the PSh saves 98% of $\pi^+\pi^-$ events.

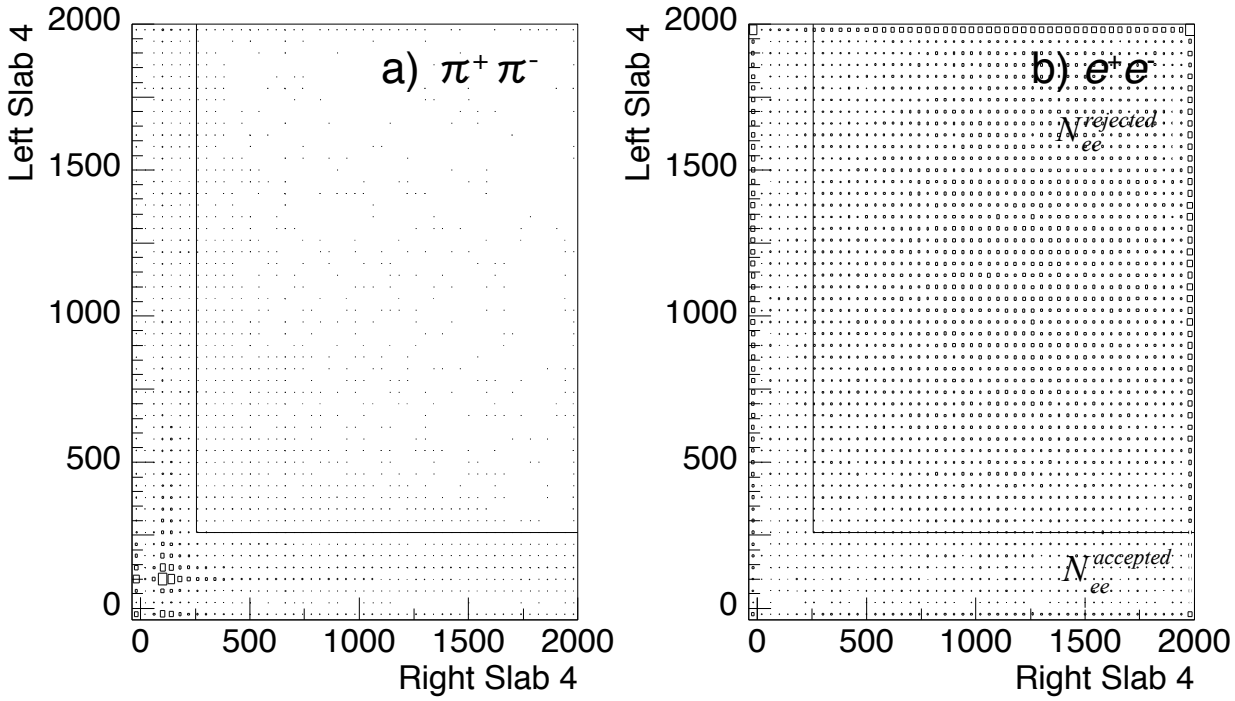

Fig. 5.30 (a) Distribution of the $\pi^+\pi^-$ pairs over amplitudes, detected by the 4-th PSh counter in the Right arm and the 4-th PSh counter in the Left arm; (b) Similar distribution for e^+e^- pairs.

In the next step, for each pair of slabs, has been defined the ratio (R_{ee}) of e^+e^- accepted ($N_{ee}^{accepted}$) to the rejected ($N_{ee}^{rejected}$) events :

$$R_{ee} = \frac{N_{ee}^{accepted}}{N_{ee}^{rejected}} \tag{1}$$

To improve the electron rejection, in the transverse relative momentum Q_T spectra, the PSh rejected events are subtracted from distribution of initially accepted events with the weight R_{ee}.

The results are presented in Fig. 5.31 (top) for e^+e^- pairs and in Fig. 5.31 (bottom) for $\pi^+\pi^-$ pairs. Initial distributions are presented by solid lines. The distributions after the selection on the amplitude in the left and right arm of the Preshower are shown with dashed lines. The criterion accepts 97.8% of $\pi^+\pi^-$ pairs and rejects 87.5% of e^+e^- pairs. After the additional subtraction, the distribution contains 97.5% of $\pi^+\pi^-$ pairs, and 99.9% of e^+e^- pairs are rejected.

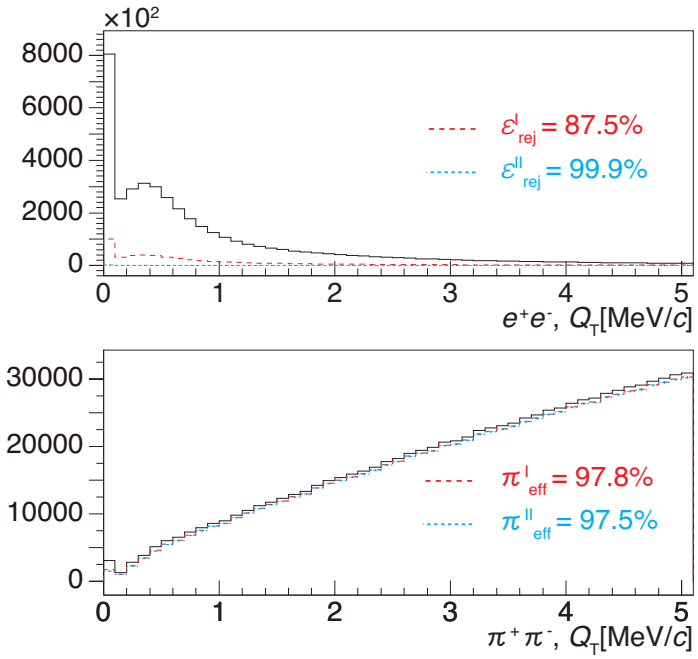

Fig. 5.31 Distributions of the transverse relative momentum Q_T of e^+e^- and $\pi^+\pi^-$ pairs without PSh conditions (continuous line). I. after PSh cut electron rejection (red dashed line) and II. after additional subtraction of the electron admixture (blue dotted line) in the PSh cut data.

5.6 Muon counters

The two identical arms of Muon detector of the DIRAC setup are composed of a variable thickness steel absorber (from 60 cm in the soft region to 140 cm in hard momenta region) for hadrons and hadronic showers absorption and scintillation counters with photomultipliers as sensors. The distance to the target is 16.5 m. The transverse area covered by each arm is 4130×750 mm^2. The total number of slabs in each arm is 2 × 68 (4+28+2) with two different type of counters design. Active area of one slab 120 × 750 mm^2, the thickness varies from 5 to 10 mm depending of the design type. The role of the muon detector is to reject muons, which are a background for pions and kaons we are interested in. Most of these muons result from the decay of pions and that part of the pion, which decayed up the Drift Chambers induces a significant error in the relative momentum reconstruction of the $\pi^+\pi^-$.

Initially, the detector was composed of steel absorber and a single layer of scintillation counters with active area 750×120 mm^2 and 5 mm thick with fish tail light guide, but as right after the muon detector there is a beam catcher with beam dump, it was found that in the place of Muon Detector there is a high background radiation produced by proton beam in the beam dump.

To eliminate an influence of this background, the second layer of scintillator slabs and coincidence circuit based on CAEN C561 mean timer were added. The coincidence scheme was described in [ADE03B]. These modifications significantly reduced the influence of the background. Due to the lack of space at the location of the second layer for this layer, another design has been suggested. The active area of the slab has the same size, but the photomultiplier was rotated by 90 degree with respect to the slab plane without light guide. For that reason, the slab thickness was increased to 1 cm in order to keep the same number of photoelectrons (> 20) from the distant part.

As acceptance of the setup should be increased after upgrade two pairs of slabs near the axis of the beam and the four pairs in the far side of the beam in each arm of the Muon Detector were added [BRE08B]. Steel absorber has been added accordingly. In all slabs regardless of their construction geometry one-inch photomultiplier FEU-85 was used for light collection. A general view of hodoscope is presented in Fig. 5.32.

The readout circuit is completely identical to that used in the previous installation of DIRAC and described in details in [ADE03B]. The muons are discarded during offline processing, and the fraction of events with potential muons in at least one of the arms is about 10%.

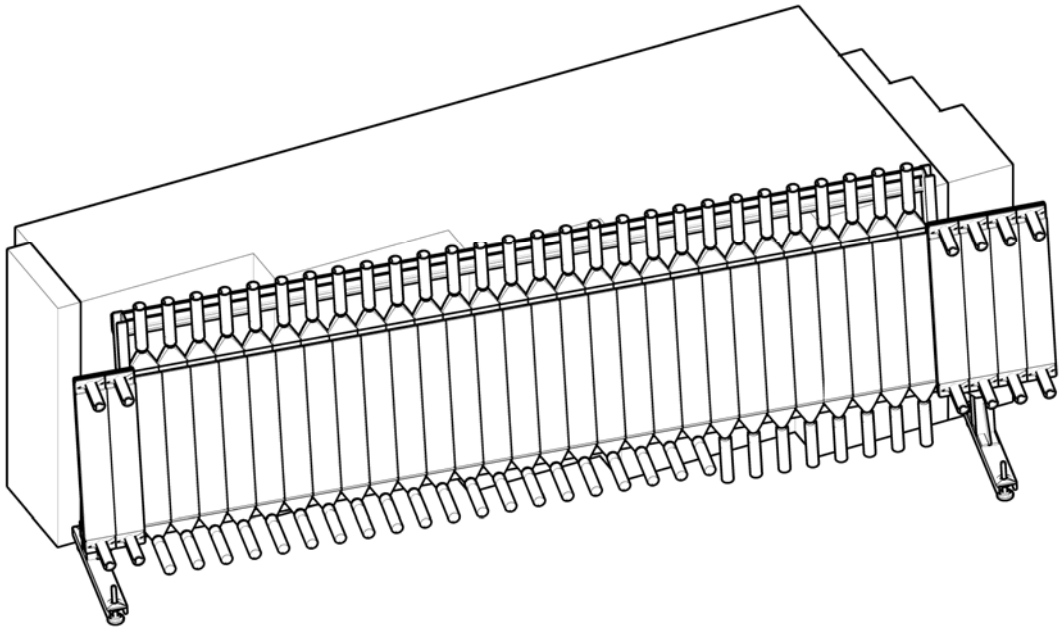

Fig. 5.32 General layout of one arm Muon Detector

6. Electronics

Architecture design of the data acquisition system needs consideration of the time structure of the proton beam. The DIRAC experiment accepts protons in spills with a length of 400-600 ms (maximal width of the gate signal is 700 ms). The number of spills extracted for the T8 DIRAC experiment varies from 1 to 6 within a supercycle of about 40 s with a minimal interval between spills of 2.4 s. The data coming from the front-end electronics during spills are collected in the buffer memories without any software intervention. A slow procedure of data transfer to computer, check of the data consistency, event building, distribution and storing is performed during the pauses between spills.

Originally, the data acquisition system was constructed with eight front-end readout branches connected with VME buffer memories [KAR03]. Unfortunately, the capacity of this system was too low for the new upgrade. For this reason, a new data transfer system (DTS) with a higher bandwidth was designed. After a successful implementation of one segment, introduction of this system was determined for the whole setup and was carried out in the following steps. First, full scale DTS including the front-end part was implemented to almost all scintillating and Cerenkov detectors. Next, the data transfer part was implemented to the rest of detectors, which was simply a replacement of the VME buffer memories. The DAQ scheme at this stage is shown in Fig. 6.1.

6.1 Trigger system

The trigger system of the updated DIRAC spectrometer inherits the main features from the old spectrometer. Thus only modified or improved items will be presented here in detail. As for the old part, readers are invited to refer to [AFA02A, ADE03B] to find the detail.

Although in the previous data acquisition system the trigger for πK pairs has already been implemented together with the trigger for $\pi^+\pi^-$ pairs, the accepted trigger rate for the πK pairs together with $\pi^+\pi^-$ pairs was as low as 2000 events/spill. In the latest DAQ version of the updated system, the rate is increased by 16 times, i.e. 32000 events/spill. While the atomic pairs from the disintegration of $A_{2\pi}$ and $A_{\pi K}$ have very low relative momentum Q, typically below 3 MeV/c, pairs originating from the Coulomb or non Coulomb processes have a widely spread Q distributions. The online data selection rejects events with pairs having $Q_L > 30$ MeV/c or $Q_x > 3$ MeV/c or $Q_y > 10$ MeV/c.

The trigger system selects events with acceptable paired particles in two stages. The first level trigger T1 requires following criteria.

1. A pair requires detection of at least one particle on each arm of the spectrometer.
2. A difference of arrival times of two particles at VH falls within a definite time window. The window covers regions of true and accidental coincidences.
3. Each particle is identified as any one of e^-, e^+, π^-, π^+, K^-, K^+ or p by means of signals from Cerenkov counters.
4. A vertical distance between two particles is less than 3 slabs of the horizontal hodoscope (HH), because the relative momentum of the pair is as small as 3MeV.(Co-planarity condition)

The T1 initiates a digitisation of detector signals in the data acquisition (DAQ) modules (ADC, TDC, etc.).

At the second stage, the dedicated trigger T4 to the drift chambers (called T4 for the historical reasons. T2 and T3 were dropped in the meantime) applies selection criteria to different components of the relative momentum of pairs and makes the final decision as to the acceptance.

To evaluate the accidental coincidence events contained in the prompt coincidence time window for the removal later of those events, the coincidence window was purposely broadened up to 40 ns to acquire accidental events with an acceptance almost equal to the real coincident events. The progress of the simulation program used in the data analysis allowed us to reduce the number of accidentals, and the data were collected with two values of time window namely of 40 and 20 ns, which contributed to the reduction of number of recorded events, thus of the dead time.

In addition to the hadron pairs, e^+e^- pairs are acquired for the calibration purposes. This trigger is prescaled, but criteria concerning Q were not applied.

The whole trigger system is fully computer-controlled, and no manual intervention is needed in case a modification of the trigger configuration is necessary.

The physics and calibration trigger signals pass through a mask register and, after proper prescalings for each, are combined with an OR function. Most of the data were collected without prescaling for ππ and πK triggers, and with a factor of 6 for e^+e^- trigger. A specific trigger mark is added to every event to allow sorting the data by the trigger type in the offline analysis and the online monitoring.

All T1 modules are ECL-line programmable multichannel CAMAC units. Most of them are commercial modules, except for the dedicated coplanarity processor and the drift chamber track processor (T4), which have been custom-developed at JINR. Mean–timer units are used in all VH and HH channels in order to remove the dependence of the timing on the hit position, thus reducing the total trigger time jitter.

The drift chamber processor T4 is placed at the last trigger level. The T4 processor reconstructs straight tracks in the X-projection of each arm of the drift chambers and analyses them to determine the value of the relative momentum (the algorithm is described in Ref. [AFA02A]). The drift chamber processor consists of two stages: the track finder and the track analyser. The track finder receives lists of hit wires from all drift chamber X-planes. To obtain the track information more quickly, precise position obtained from the drift time is not used in the T4 logic. A unique code, track identifier, which contains the encoded numbers of the hit wires, is attached to the found track. The rejection factor at this level is about 2 [AFA02A]. If tracks are found in both arms, the track analyser starts processing the event. The track analyser receives the track identifiers from both arms and compares them with the content of a look-up memory table which contains two pairs of values specifying intervals of momentum and emission angles from the target in the horizontal plane. Intersection of these intervals for tracks in the left and right arms designates the event fit criteria namely $Q_L < 30$ MeV/c and $Q_x < 3$MeV/c for the pion pairs. These intervals had been obtained from a dedicated simulation based on the precise geometry of the setup.

If a relevant combination is found, the T4 processor generates a positive decision signal that starts the data transfer to the DAQ memories. Otherwise, the Clear and Reset signals are sent to the DAQ and to the trigger systems. The T4 decision time depends on the complexity of the event and is about 3.5 μs in average. The rejection factor of full T4 is around 4 with respect to the T1 rate.

As the selection criteria on the components of the relative momentum Q are different for ππ and πK atomic pairs, the track analyser does not provide the same effective

rejection rates for the two event types. To obtain a better suppression, most of the data collected earlier had the full-scale T4 applied to the ππ trigger, whereas for the more recent πK trigger, events were rejected only by the track finders.

During the analysis of the metastable ππ atoms carried out at the final stage of the experiment, T4 was removed in order to avoid possible unexpected biases. A significant increase of DAQ capacity made it possible to accept all events after the T1 trigger. The typical number of accepted events was about 2000 per spill at the beginning of experiment and about 9000 at the final stage. As a result, the trigger dead time increased from 22% to 35%.

6.2 DAQ hardware

There are 3 types of major front-end electronics used in the DIRAC setup:

1. Electronics for the Drift chamber (DC) that consist of TDC boards (for MDC with modified inputs) and auxiliary controllers (N404: see next section) [AFA02B]. They are custom made in NIM standard and are located in the beam area near the detectors. Dedicated CAMAC modules are used for the control and the setting of the electronics. The total number of channels for the whole DC's is 2592 (2016 - DC and 576 - MDC). This electronics is grouped in 4 readout branches (3 DC and 1 MDC).
2. Electronics for the FERA readout system including several types of CAMAC discriminators, TDC LeCroy 3377, ADC LeCroy 4300B, and programmable module LeCroy 2366 (configured as a register and counters). These modules are made in CAMAC standard and located in the control room. These electronics are used for the Y and U planes of the SFD, the preshower and muon detectors (in total 908 TDC channels and 40 ADC channels for the preshower detector). FERA buses of this electronics are grouped in 5 readout branches (N417: see next section).
3. Combined ADC/TDC (F1-TDC-ADC) boards of DTS and auxiliary modules are made in euro-mechanic and NIM standard (D412, N414 and N414AX: see next section) and located in the experimental area close to the detectors. This electronics is used for the X plane of the SFD, the IH, the VH and HH and the Cerenkov detectors (726 channels in total on 51 boards) and grouped in 2 readout branches connected to DTS transmitters (N415: see next section).

During the whole data taking period up to year 2010, the DC and FERA readout branches were connected to the two types of VME buffer memories LeCroy 1190 and CES HCM 1870. The capacity of these buffer memories was the main limitation for the number of accepted triggers. For this reason, the VME buffer memories were replaced by one L1P module of new DTS (see below) by 2011. So the number of readout branches was reduced to 3. This modification allowed us to work without higher level trigger using DC information (so-called T4 trigger).

The TDC boards for DC and LeCroy 3377 modules are operated in the common stop mode. The T1 trigger generates two signals, one for a stop signal of the TDC and the other for a gate signal of LeCroy 4300B ADC. For the reason above, linear signals from the detectors must wait just before the ADC until the completion of the gate formation by the T1 signal. In T4 trigger mode the readout of DC and FERA modules is inhibited until T4 decision is ready and, in the case of negative decision, data are cleared inside the modules.

The slowest data sources are some CAMAC modules (mostly scalers integrating the information during each spill), VME register CAEN V259 (collecting alarms from different

setup components) and the beam intensity information provided by PS accelerator via computer network. These informations are read once at the end of each spill.

Directly controlled modules are located in one VME crate, 12 CAMAC crates arranged in 2 CAMAC branches and one NIM crate (L1 modules).

For the control of the VME modules, a Concurrent Technologies VP110 VME processor board is used. The program in the VME processor is linked to the VME library developed by ATLAS group at CERN. The CAMAC crates are controlled by Wiener CC16 crate controllers via VC16 VME-CAMAC interfaces connected to the VME computer.

Beside the VME computer, the DAQ system consists of the main DAQ host, the data storage host and the online monitoring host. All the computers work under Scientific Linux CERN operating system.

6.3. DTS Hardware

Data transfer system (DTS) transmits data from the front-end devices (Level 0) to the host computer. The system topology is presented on Fig. 6.1. L0 devices select the detector signals, digitize them, and send the event data blocks to the level one (L1) transmitters. The L0 device must send only one data block per event. The input ports of the L1 transmitters are buffered and therefore all the L0 devices can transmit the event data blocks in parallel. A type of connections between these levels depends on the specifications of the L0 devices. The L1 devices pre-process these data and send them to the Level 2 transmitter (N415). With the system clock of 40 MHz the data transfer rate is 400 Mbps of payload per port for the F1-TDC-ADC boards (D412) (see upper part of Fig. 6.1). There are three type of L1 transmitters; L1S with serial inputs (N414), L1P with parallel ones (N417) and the auxiliary transmitter L1A (N414AX). The L1 and L2 transmitters are connected with low-cost coaxial cables of which the maximum transmittable length is 100 meters. Both logical and electrical parameters of this connection are specific to this data transfer system.

The L2 transmitter is connected to the host computer with a USB 2.0 serial bus. This connection allows to use any computer as the host and easily expanded many data transfer system. Input ports of the L2 transmitter are buffered and therefore all L1 devices can transmit the event data block in parallel.

The host computer controls the whole DTS over USB 2.0 bus also. If the control data packets are addressed to the lower level devices, then L2 transmitter converts these packets to a serial format and sends to these devices. L1 and L2 transmitters are designed in NIM standard.

During the beam spill, the DTS writes, formats and collects the event data, which come from the L0 devices (write phase). Formatted event data are collected in memory of the L2 transmitter in a consecutive order as a set of data frames. In the time interval between beam spills, DTS transmits data to the host computer (read phase). The write phase is triggered by the accelerator synch pulse. After an adjustable time interval the DTS goes to the read phase. This phase is terminated when all data frames are transferred to the host computer.

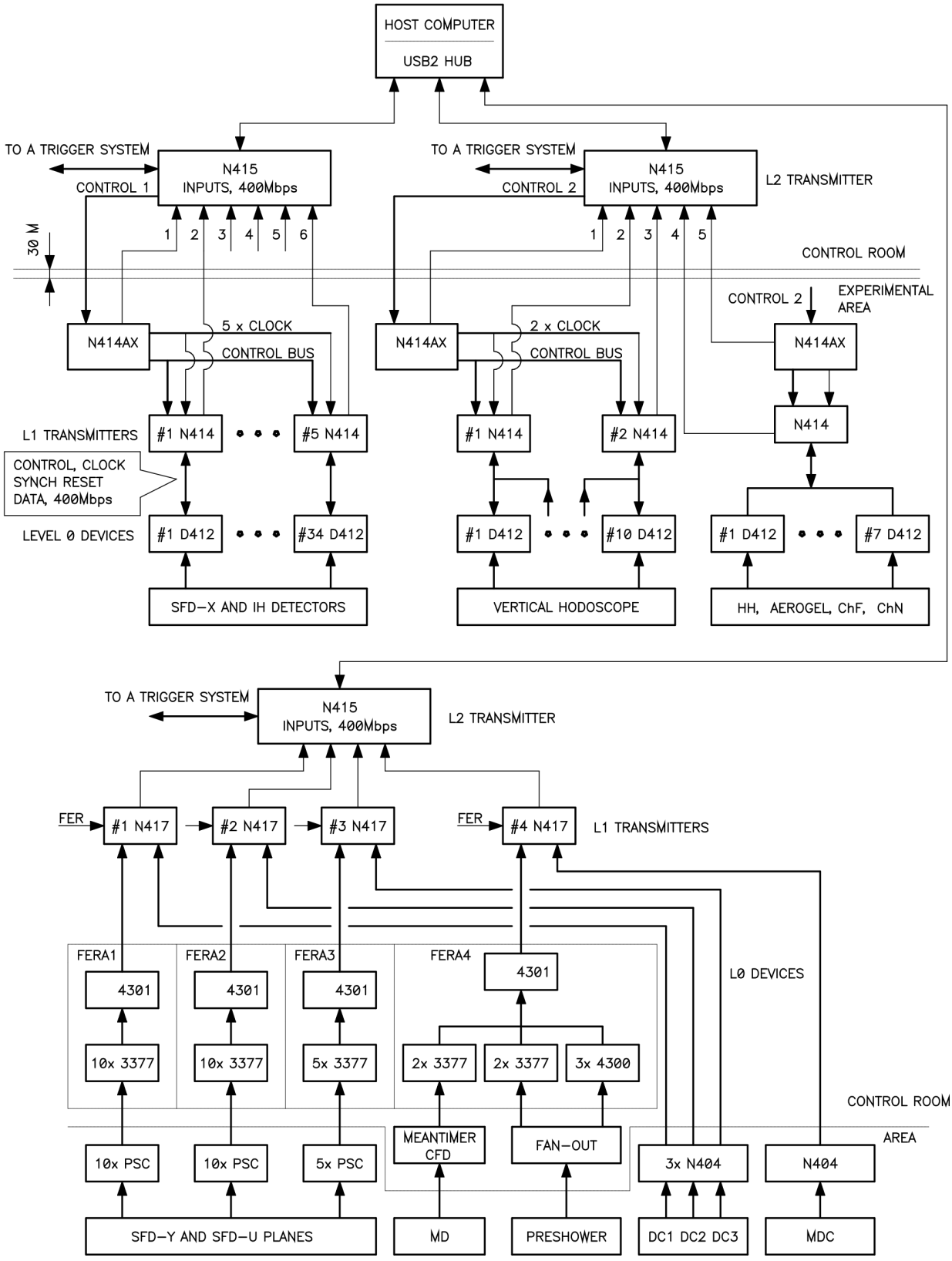

Fig. 6.1 Topology of DIRAC data transfer system. The abbreviation SFD stands for the scintillating fiber detectors, IH the ionization hodoscopes, HH the horizontal hodoscopes, ChF, ChN the Cerenkov counters, DC and MDC the drift/micro drift chambers, MD the muon detector, CFD a constant fraction discriminator, PSC a peak-sensing circuit. N404 is a controller of DC/MDC readout system. FERA is LeCroy Fast Encoding and ADC Readout system. Blocks 3377, 4300, 4301 denote the correspondent LeCroy CAMAC units. (All other abbreviations are given in the text.)

6.3.1 Level 0 devices

Originally the ADC/TDC board D412 was designed as a level 0 device. Later the FERA branches [ADE03A] and the DC/MDC [AFA02B] readout systems were connected to DTS as L0 devices via L1P transmitters (N417 see later section).

ADC/TDC board D412

The D412 board is a native L0 device, which was originally designed to process signals coming from PSPMs of SFD. The D412 can measure both the arrival time and the charge of an input pulse independently in each channel. In addition, there are 16 prompt outputs which can be used in the trigger system.

The D412 F1-TDC-ADC board is built around the TDC-F1 chip [ACA01]. The pulse arrival time is measured immediately by this chip, serving as a TDC. The ADC consists of a charge-to-time converter and the TDC-F1. The input pulse triggers a voltage comparator and the comparator output initiates a charge integrator followed by a discharger, i.e. a charge-to-time converter. As a result TDC-F1 records two time stamps. The first one marks the pulse arrival time, and the second time stamp marks the end of the pulse charge conversion. As the time difference between these stamps is proportional to the integrated charge of the input pulse, thus serves as an ADC.

After a triggering signal, the D412 boards select the event data inside a preset time window, serialize and send the selected data to L1S transmitters (N414). All boards operate in parallel, essentially reducing a readout dead time. The D412 boards are housed in dedicated crates near the detectors and are connected to the detector outputs by short 50Ω coaxial cables. The L1 transmitters inserted to NIM crates are also placed in the beam area.

TDC-F1 chips have two modes, namely low and high time resolution modes with a least count of 120 ps and 60 ps, respectively. The number of channels per chip is 16 in the low resolution mode and 8 in the high one. D412 board supports both modes and the number of channels per board is either 16 or 8 depending on the mode chosen. Some important specifications of the board are: an amplitude of linear input pulse- 0–400 mV, a minimum width of the input pulse - 1 ns, dynamic range of an input charge - 0.4–150 pC, least count – 0.4 pC, the range of charge collection time - 5–25 ns, the maximum data transfer rate - 40 MB/s.

6.3.2 Level 1 transmitters

L1 transmitters accept the front-end device data, pre-format and send them to level 2 devices. Input ports of the transmitters are adapted to the specific L0 devices while outputs are standard both logically and electrically. There are three types of L1 transmitters.

N414 transmitter with serial input ports L1S.

The N414 transmitter device is adapted for connecting the native F1-TDC-ADC D412 boards (see above). After conversion time in every D412 boards, the event data blocks are sent to N414 in series with a rate of 400 Mbps. The N414 converts these data to a 10-bit word format and feeds them in parallel to the buffer memories inside. After the completion of the data transfer from all the boards, the N414 begins reading these buffer memories. The read-out is performed in a priority mode but skipping empty buffers.

N414AX auxiliary transmitter

The N414AX auxiliary transmitter is introduced to make a control between many N414 L1S transmitters and the N415 L2 transmitter simply and to measure a reference time for each D412. The functions of the N414AX are followings. First, it generates a 40MHz system clock and control signals for the N414 transmitters and a synch reset signal for the D412 boards. Second, it generates a time interval between the synch reset signal common for all D412 boards and a pulse arrival time (the first stamp) in each D412 board. The data transfer from the N414AX to the N415 L2 device is initiated by the trigger signal and is executed at the same time of the data transfer from the N414 transmitters. Therefore, the output data format of the N414AX is quite identical with the N414.

N417 transmitter with parallel input ports L1P.

The N417 transmitter receives data from the FERA and the DC readout subsystems. The device has two parallel ports. The FERA must be connected to the first port, which is a 16-bit word high priority port at a working rate of 5 MHz. The DC data are fed into the second port, which is a 23-bit word port, and is adapted for DC readout subsystem at a working rate of 10 MHz. The FERA and DC data are converted to a 10-bit format and transmitted to the buffer memories. Data of the FERA are transferred from the first port to the N415 L2 device. Empty buffers are skipped. During this transfer interval, the second port is filled with the DC data. On the receipt of a DONE signal (FERA PASS) of the FERA transfer, a data transfer of the second port to the N415 is started. The output data format of the N417 L1P transmitter is identical with that of the N414 L1S transmitter.

6.3.3 Level 2 transmitters N415

N415 L2 transmitter is the highest-level device in the DTS segment. The transmitter has a 7-bit address field, thus up to 127 DTS segments can be connected to an USB 2.0 system. It runs under three different time phases; a read phase, a write phase and a front-end read phase.

During a beam spill, the N415 transmitter receives data, formats them and collects event data frames. In the interval between spills, data frames are transmitted to the host computer in a consecutive order starting from the first event in the spill.

The N415 receives 10-bit serial data from the L1S and L1P through 75Ω coaxial connectors with a rate of 400 Mbps. There are 6 independent input channels, each of which has an AC coupled input and an equalizer.

The N415 receives event data only in the write phase. Serial data are converted into a parallel format and are collected during the spill in DRAM memories. The size of the packet received is compared with a packet size calculated in level 1. If an error occurs then the N415 sets a corresponding status bit in a start-of-frame packet. The host computer can process this frame as corrupted. In the write phase all data acquisition channels work in parallel, and independently.

In the read phase the N415 transmits the data frames from memories to the host via USB 2.0 port in a high-speed bulk mode. The data transfer rate depends on the host computer and software programs in operation and is actually 25 MB/sec.

In the working mode the data transfer from the front-end devices to the host is controlled by external signals via the N415 trigger port. The setup trigger system must generate at least 3 signals: WRITE, FER and READ. The WRITE command sets the N415 in

the write phase. The FER is a front-end readout command; the trigger system generates this command to take the current event. In response to the FER, the N415 asserts a BUSY signal and holds it until this event is processed. The READ command sets the N415 in the read phase.

6.3.4 Lower level control

L0 and L1 devices are controlled over a 2-wire serial bus (two twisted pairs on the L2 control connector). The host computer feeds a control data packet into endpoint EP2 of the USB controller. If EP2 is not empty then L2 reads data bytes from this endpoint, converts the data packet into a serial format and sends it to the level 1. If a data packet is addressed to the front-end device(s), then L1 transmitter routes this packet to the level 0.

6.4 DAQ software

The main DAQ program for the DIRAC setup is composed of following several programs. They are programs for a run initialization, several types of data readout (called Readers), an event builder, a data recording, a data distribution, a run control, an online monitoring and for a high voltage control. The run initialization program loads parameters into CAMAC controlled modules-composed of trigger system electronics, DC and FERA front-end electronics. It begins its execution at the beginning of the DAQ program running separately. Such a role-sharing by several independent modules can significantly simplify the transition of the readout from the VME memories to the L1P transmitters.

Three programs for data readout from different electronics are called 'Reader'.
The first Reader runs on the VME computer for the readout from the LeCroy 1190 and the CES HCM 1870 VME buffer memories.
The second Reader runs on the main DAQ host computer for the L2 USB buffer memories.
The third Reader runs on the VME computer for the beam monitor counters and beam intensity information.

The first Reader performs a synchronization task during the interval from start to stop of a data acquisition, and reads all the CAMAC modules at the end of each spill.

These tasks are preserved as first reader after tasks for all the front-end electronics have moved to the second reader.

The third Reader is special, because the information from the PS accelerator arrives late after the end-of-spill signal, or even worse, they can be missing at all due to a trouble in the network., Thus a timeout or no data is allowed for this readout.

The Builder program working on the main DAQ host receives the data from the Readers. After a check of consistency among the data, it builds events. Where, the data consistency means the time information from the Readers, the number of registered events in different readout branches and some other information from the readout electronics. Then the data are distributed to the storage and monitoring hosts.

The sharing of the data among DAQ processes is done through the shared memory buffers. On each computer needing an access to the data online, there is a special program which acts to receive the data from the main DAQ hosts and puts them in the shared memory. Any number of data consumer programs, like monitoring programs, can access the shared memory buffer. Data consumer programs can be started/stopped at any time.

Following four programs that control a run or monitor an acquisition status are executed on the DAQ host computer and are equipped all with graphical user interface(GUI).
The run control program sets run parameters, selects a trigger type, makes a start/stop the run.
The run display program displays current status of the run, information about last processed spill and the accumulative statistics.
The run monitor program generates vocal information messages about changes in the run status, detected errors and received alarm signals and displays them on the monitor.
The scaler monitor program displays current and cumulated scaler values.

The main online monitoring program is written in the frame of ROOT software package. The program fills several hundreds of histograms, including time and amplitude distributions for each channel of the majority of detectors, time distributions of groups of channels of the drift chambers and the scintillating fiber detectors, hit and multiplicity distributions and two dimensional correlations between hit distributions of different detectors. The program allows a selection of trigger types, for which all above histograms should be filled. A saved set of histograms served as good examples can be used as a reference to be compared with current histograms such that one can easily and quickly pinpoint if there is any anomaly in the data acquisition.

Besides the main monitoring program, there is another program for automatic monitoring. This program collects a basic set of histograms for each channel (some thousands of histograms) and periodically compares them with ~~a~~ the reference mentioned above. When a noticeable discrepancy is found in any of the histograms, it generates an alarm signal.

The last component of the DIRAC setup software is a program for the high voltage control. This program can be used separately from other DAQ software. As the high voltage power supplies for all detectors (except for the drift chambers) we employ CAEN SY527 and SY1527 systems with different boards. The total number of high voltage channels is about 500. The program allows the setting of various parameters of these boards, and checks periodically their status. In case of an error an alarm signal is generated.

The control of all the components of DIRAC setup is performed from a monitoring host by a single operator.

7. Overall performance of the DIRAC spectrometer

For the success of the DIRAC experiment it is essential to have a high resolution setup to measure with a high precision the relative c.m.s. momentum Q of particles in pairs. The aim of DIRAC is an investigation of $\pi^+\pi^-$, π^-K^+ and π^+K^- atoms. The method of atom lifetime measurement assumes the observation of "atomic pairs" as an additional peak at small Q (Q<3 MeV/c) over a background of "Coulomb" and "non-Coulomb" pairs [ADE11]. It is needed to take into account that "Coulomb pairs" also form a peak at Q=0 due to Coulomb interaction in the final state. To observe signal it is needed to have a high resolution of Q and its projections Q_L and Q_T in order to exclude the smearing of the "atomic pair" peak among a large amount of background pairs. The characteristic parameter for the width of peaks in distributions of "atomic" and "Coulomb" pairs is the Bohr momentum of atom, p_B=0.8 MeV/c for πK atoms. The resolution of DIRAC setup is adjusted to be at this level.

The experimental data are fitted by a sum of simulated distributions of "atomic", "Coulomb" and "non-Coulomb" pairs. The contribution of each distribution is a free parameter of the fit. An example of such a fit for the distribution of $\pi^+\pi^-$ pairs, collected in 2008-2010, is presented in Fig. 7.1. This fit allows obtaining estimations for the number of "atomic pairs" (n_A) and the number of produced atoms (N_A), which is deduced from the measured number of "Coulomb pairs" [ADE11]. Together, these two values allow obtaining an estimation of the breakup probability (P_{br}), which has a one-to-one correlation with the $\pi^+\pi^-$ atom lifetime [ADE11].

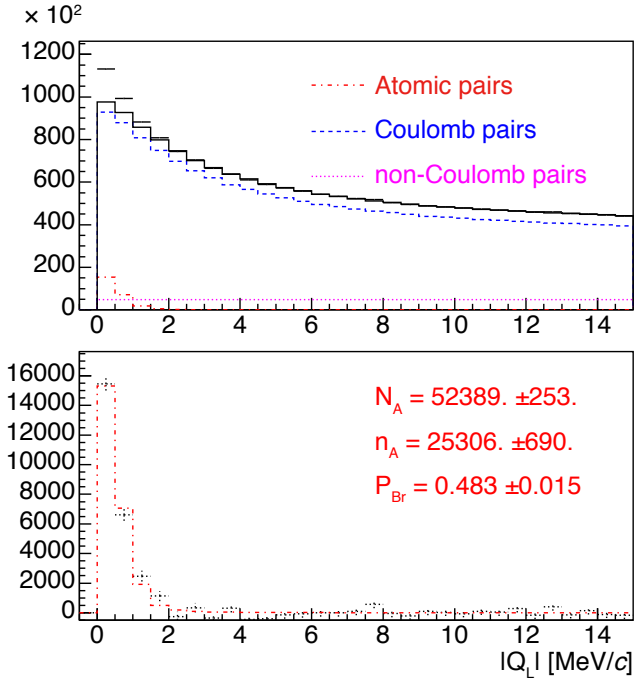

Fig. 7.1 Distribution of $\pi^+\pi^-$ pairs over Q_L (upper picture), shown by points with error bars, is fitted by a sum of simulated distributions of "atomic" (red dashed-dotted), "Coulomb" (blue dashed) and "non-Coulomb" (magenta dotted) pairs. A sum of background distributions ("Coulomb" and "non-Coulomb") is shown by a solid black line. Differences of experimental and background distributions are shown on lower pictures together with simulated distributions of "atomic pairs"

Resolution of the setup over laboratory momentum p, relative momentum Q components - longitudinal Q_L (which is a function of laboratory momentum p of particles), and X- and Y-components (Q_X and Q_Y) of transverse projection Q_T (is proportional to open angle of pair measured by upstream detectors and laboratory momentum of the pair) is defined by spatial resolution of coordinate detectors and multiple scattering in the detector planes, the setup partitions (membranes) and surrounding air.

Difference of smearing in experimental and simulated distributions, induced by wrong definition of the setup resolution, leads to bias of estimated parameters at fit procedure.

7.1 General description of the Monte Carlo simulation

At the first stage, samples of "Coulomb" and "non-Coulomb" π^-K^+ and π^+K^- pairs were generated with a distribution of the total laboratory momentum of pairs P in agreement with the experimental momentum distribution of such pairs [GOR10]. The distributions over the relative momentum Q projections (Q_L, Q_X and Q_Y) are uniform for "non-Coulomb pairs" and modified by Gamow-Sommerfeld factor for "Coulomb pairs". The vertex position is simulated uniformly in the target thickness (98 μm of nickel for 2008 or 108 μm for 2009 and 2010).

πK atoms have the same distribution in the laboratory momentum as "Coulomb pairs" and the atom generation points are also uniform in the target thickness. The positions of the break-up and excitation points where they occurred are obtained by solving numerically the transport equations with the cross-sections for break-up and excitation [AFA96, ZHA08]. The distribution of the relative momentum Q depends on the atomic state at the break-up point.

At the second stage, the GEANT3 based program GEANT-DIRAC [GOR05] propagates particles through the DIRAC setup. The program has been modified to take into account the specific updates of the setup.

Coordinates of detector plane crossed by particles and energy losses in the detector volumes are registered. The membranes, air, shielding materials and collimators are included in the GEANT description in order to correctly simulate the scattering of particles.

In the third stage the response of each detector is simulated by a dedicated code at the initial phase of the offline data analysis program ARIANE. These codes use data prepared by the GEANT-DIRAC program and take into account coordinate, time and amplitude resolution of the detectors. The Cerenkov detectors do not have a proper simulation of the light propagation in GEANT, but have a simulation in ARIANE that produces, event by event, a response in photoelectrons for every type of particles depending on its momentum, charge, and position.

The accuracy of the setup description is tested by comparing experimental and simulated distributions for calibration processes, which is described below.

After the calibration, the Monte-Carlo procedure provides proper distributions for investigated pairs and also allows to estimate the resolution of the setup for measured parameters: laboratory momentum of particles and relative momentum of pairs.

7.2 SFD simulation

The SFD detector plays a fundamental role in the upstream tracking. Since SFD is relatively close to the target, (distance: 281cm), it is important to reproduce in simulation its response to pairs of tracks with small opening angles, because they are immediately translated to the Q_T resolution of the track-pairs.

A big improvement has been achieved for the SFD simulation in the years 2008, 2009 and 2010. The results have been presented in [BEN11] in detail.

Only events with one track in each arm have been used in this investigation. In reality, when one charged particle hits a SFD plane, several columns are fired at the same time. This is mainly due to the grazing effect; a particle hitting a plane not perpendicularly to the plane, crosses several scintillator columns. The cross talk at different levels adds to this phenomenon [GOR00]. However, in the simulation, only one specific column fires. Thus to simulate these effects, we have added, with a probability of 20−28%, to every true Monte-Carlo hit in the plane a firing in the neighbouring columns, and larger cluster of hits with smaller probability. The photomultipliers cross-talk has also to be taken into account and, due to their geometrical disposition, we have added to every true hit a 2−3% extra hit at a column distance of $\Delta n = \pm 4$ [GOR00]. This procedure introduces some diffuseness to the simulated hit position. Then the off-line PSC algorithm was applied to the full SFD plane. The threshold of the off-line PSC was chosen as 20% of the most probable pulse height of the distribution, which reproduces correctly the hit multiplicity (number of hits recorded when one particle hits a plane).

To study one plane (e.g. X plane), the hit information from two other planes (e.g. Y and U planes) together with the track information from DC have been used in ARIANE in the reconstruction of the two tracks. This procedure predicts coordinate of a track in a plane under investigation with accuracy, estimated by Kalman filter of:

$$\sigma_{SFDx}^{pred} = 0.021 cm, \quad \sigma_{SFDy}^{pred} = 0.017 cm, \quad \sigma_{SFDu}^{pred} = 0.007 cm.$$

They are equivalent to 1.02, 0.83 and 0.16 fibre columns for X, Y and U planes, respectively.

The average multiplicity recorded in the tracking window (1 mm around the tracking prediction) when "a pair of particles" hit the plane is μ_X=2.04, μ_Y=2.15 and $\mu_U = 1.95$, for X, Y and U planes, respectively. The agreement between the data and the simulation is quite good as shown in Fig. 7.2 for the case of X plane.

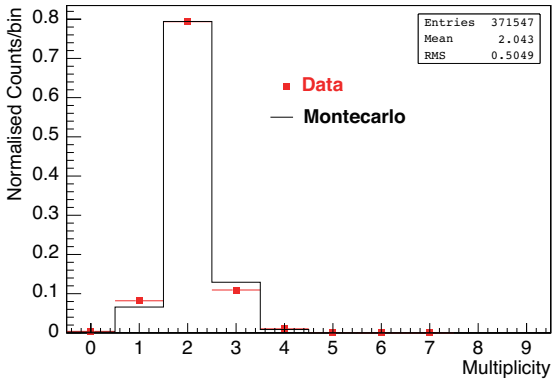

Fig. 7.2 Hit multiplicity in SFD X plane in case two charged particles cross the plane

Pairs of predicted hits whose distances (measured from positive particle to negative particle) on the investigated plane are less than 20 columns were selected, and the total number of real hits found in the vicinity (within 1 mm) of these hits is shown in Fig. 7.3. The left figure shows the probability of finding only one hit within these two regions, P(1), whereas in the right figure shows P(2), the probability of finding two hits.

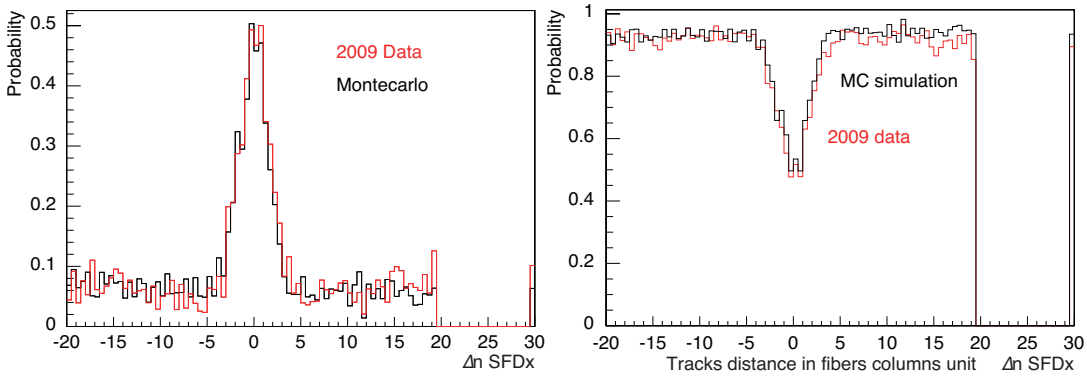

Fig. 7.3 Probability to have one hit (P(1) - left plot) and probability to have two hits (P(2) - right plot) around the extrapolated tracks in SFD X plane

Fig. 7.4 shows the overall efficiency of the X plane experimentally observed in comparison with the simulation. The agreement is quite good. The average detection efficiency for a pair of particles in this plane is 94.7% including the dip in the middle, and 96.6% outside the dip. The latter corresponds to the square of the efficiency calculated (0.976) in **4.2.3**.

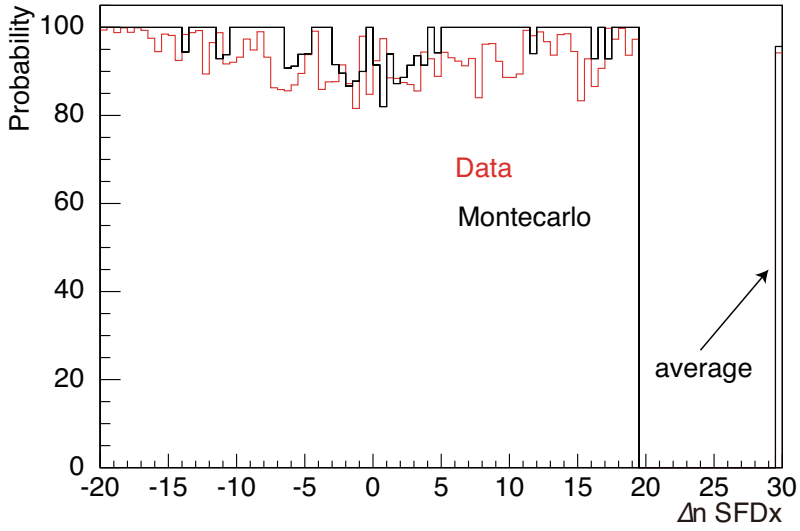

Fig. 7.4 Overall efficiency in SFD X plane for a pair of particles

7.4 Multiple scattering

The thicknesses of the detectors in the DIRAC spectrometer are minimized, especially in the frontend detectors, in order to reduce as much as possible the smearing effect of the multiple scattering in the reconstruction of particles. Despite this, particles are anyway scattered in the detectors planes and it's fundamental for DIRAC to simulate and reproduce the effect of the multiple scattering with a precision better than 1% in order to control the

systematic error due to this effect. The multiple scattering in different detectors has been measured experimentally in 2003 [DUD08] placing samples of the detectors between planes of DC. Detailed study has been performed in the past and the results were applied to the 2001-2003 data analysis [GOR07]. The simulation of the multiple scattering has been modified, taking into account the effective thickness of the detectors measured.

Since then, two of the upstream detectors have been modified, SFD X and Y planes. The latest results [BEN12] show that the multiple scattering angle due to the SFD X plane is 10% smaller than in the SFD detector, which was installed up to 2003, while the SFD Y plane is unchanged.

The study was performed using $\pi^+\pi^-$ experimental and MC data. In a first approximation the two tracks of a prompt ππ pair are originating from a single space point inside the target. The tracks are reconstructed starting from the downstream part of the detector toward the upstream detectors. The variable x_1 (x_2) is the π^- (π^+) final track extrapolated to the target plane in the X coordinates. For Y coordinates, similar variables are y_1 and y_2.

The experimental error in the measurement of the tracks determines the width of $\Delta x=x_2-x_1$ and $\Delta y=y_2-y_1$ which we call vertex resolution, since if everything goes well, these quantities must be very small. The values of Δx and Δy mainly depend on

- the SFD space resolution (momentum independent)
- the detailed material description for the upstream detectors and target (multiple scattering MS ~ $\frac{1}{p}$)
- the distance between target and upstream detector (very detailed knowledge with sufficient precision)

At first our data sample has been divided into several momentum intervals. For each of them, the rms of the vertex distribution, $\sigma_{\Delta x}$, has been evaluated via a Gaussian fit.

We can parameterise the distribution width of the two track impact points (in the target) as

$$\sigma^2_{\Delta x}=2\cdot c^2+\left(\frac{1}{P_-^2}+\frac{1}{P_+^2}\right)\cdot ms^2,$$

where c is the rms of the momentum independent fraction of vertex resolution, ms defines the rms of the momentum dependent one. We assume that the constants are the same for negative and positive particles.

Therefore it is reasonable to use

$$Z=\frac{1}{(P_-\cdot ß-)^2}+\frac{1}{(P_+\cdot ß+)^2}$$

and to fit $\sigma^2_{\Delta x}$ distribution for different value of Z.

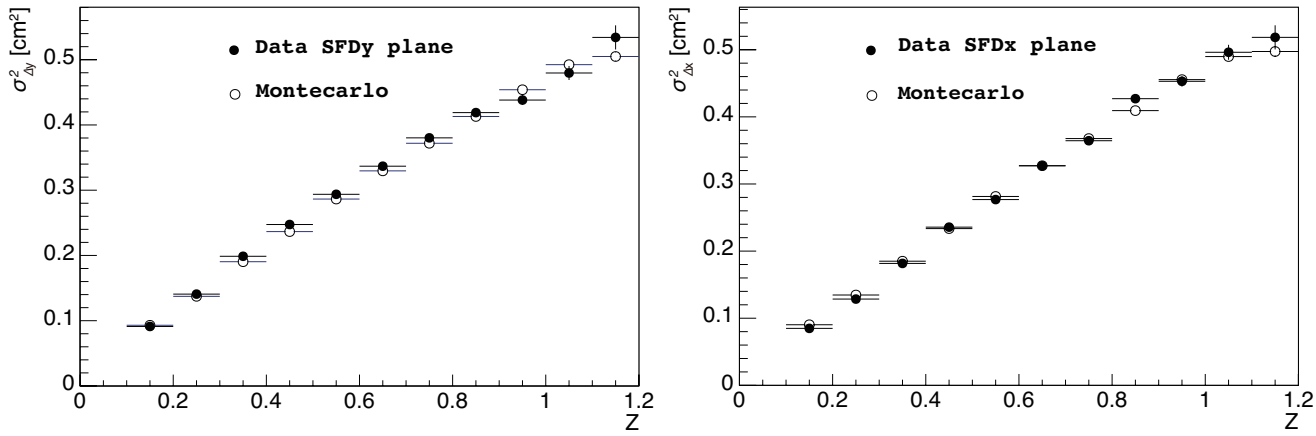

Fig. 7.5 $\sigma_{\Delta x}$ in cm^2 of the vertex distribution as a function of the variable *Z*

Fig. 7.5 shows the agreement between data and MC for the r.m.s. of the target vertex distribution as function of *Z*, on the left for the X plane of the SFD, on the right for the Y plane. In order to have a unique parameter that allows us to estimate how well we reproduce the multiple scattering in the simulation, we introduce a weighted average of the sigmas in Fig. 7.5 $\sigma_{\Delta x}$. For a 10% change in the multiple scattering angle our $\sigma_{\Delta x}$ varies by 4%. The difference between data and simulation, for what concerns the SFD detector, is now 3.1×10^{-4} for X projection and 5.5×10^{-4} for Y.

7.5 Tuning of the setup using Lambda and anti-Lambda particles

In order to check the general geometry of the DIRAC experiment, we use the Λ and $\overline{\Lambda}$ particles that decay in our setup into $p\pi^-$ and $\pi^+\bar{p}$. All the details of this study are reported in [GOR09].

The Λ mass is very well determined [BER12] and, comparing the value reconstructed in our data with the published one, we can be confident that our geometrical description is correct. The main factors that can influence the value of the Λ mass are the position of the Aluminum membrane (which is used as exit plane of the magnetic field) and the opening angle of the downstream arms. We fix the position of the aluminum membrane at z_{AL}=143.385 cm and the opening angle of the downstream arms has been modified by 10 milliradian from the nominal measurements.

Experimental distributions of the reconstructed Λ and $\overline{\Lambda}$ masses are presented in Fig. 7.6. They have been fitted with a sum of a normal distribution and a polynomial, the latter to describe background.

The weighted average of the Dirac experimental values for the Λ and $\overline{\Lambda}$ particles masses is

$$\text{Mass}\,\Lambda_{\text{Dirac}}=1.115685\pm1.2\,10^{-6}\text{GeV}/c^2$$

for the entire set of data of 2008, 2009 and 2010, in very good agreement with the PDG value

$$\text{Mass}\,\Lambda_{\text{PDG}}=1.115683\pm6\,10^{-6}\text{GeV}/c^2.$$

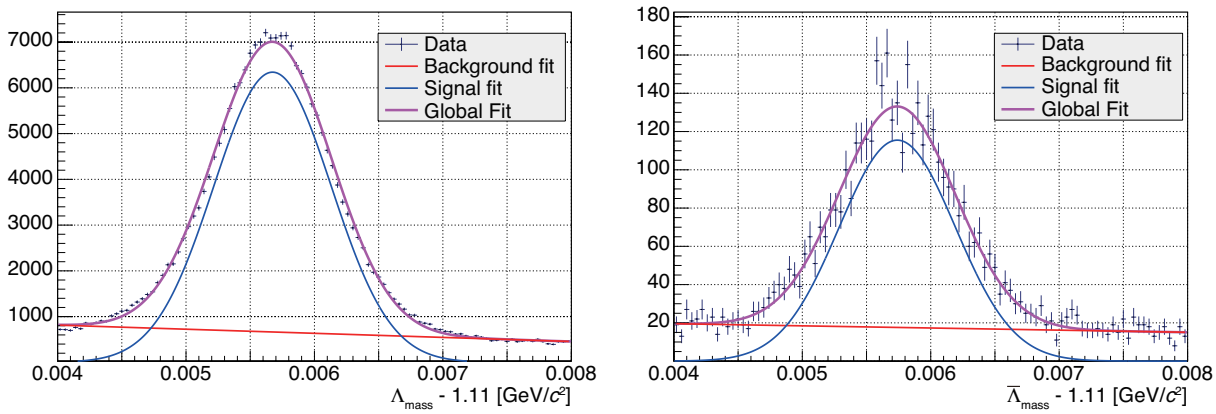

Fig. 7.6 Lambda and anti-Lambda mass distributions for the 2008, 2009 and 2010 experimental data

This confirms that the geometry of the Dirac experiment is well described. The width of the Lambda mass distribution is another tool that we use to evaluate the accuracy of the reconstructed momenta of the particles. The width depends mainly on the multiple scattering in the upstream detectors, and in the aluminum membranes at the exit from the magnet, and on the resolution and alignment of the Drift Chambers (DC). The multiple scattering in the upstream detectors has been measured using target vertex (see section 7.4). Once the multiple scattering in the upstream detectors determined, we attribute the remaining difference between experimental data and simulated data to the error in the reconstructed momenta that affects mainly the resolution of Q_L (to which DC is mainly responsible, but also other downstream detectors). From the MC simulation we obtain [GOR09, BEN13] a value for the Lambda width that is underestimated by $6-7\%$ with respect to the Lambda width in the experimental data. This discrepancy is common for all momentum bins and for both Lambda and anti-Lambda particles. This problem can be fixed by introducing purposely a Gaussian smearing in the reconstructed momenta. We multiply a factor which follows a normal distribution with mean 1, and the standard deviation j x 0.01% to both momenta of protons and anti-protons. Then we evaluate the difference in the Lambda mass distribution between the data and MC by using a quality of agreement χ^2 value, which is a sum of the difference squared in different mass bins between 0.004 and 0.008 GeV/c^2.

As shown in Fig. 7.7, a best agreement is obtained when the smearing is 0.07% RMS.

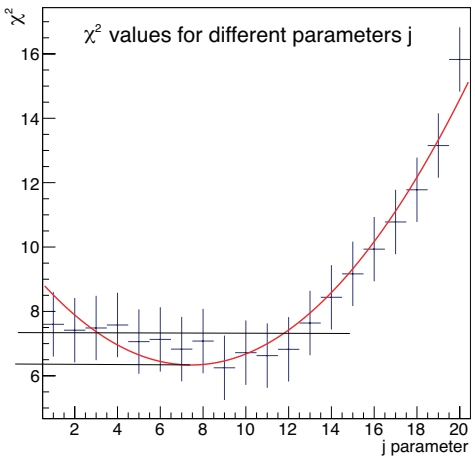

Fig. 7.7 χ^2 for different values of the parameter *j*

We then apply the smearing of 0.0007 to the reconstructed momenta, and, as expected, the data and simulated distributions are in perfect agreement, as shown in Fig. 7.8.

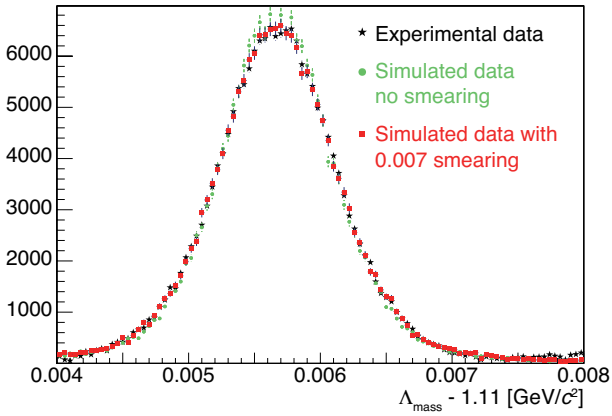

Fig. 7.8 Lambda MC and experimental data superimposed, in green is the MC distribution with no smearing applied, in red is the MC simulation with the smearing of 0.0007 applied, in black is the experimental data distribution

The Q_L distribution of the $\pi^+\pi^-$ can be used as a test for the checking of the geometrical alignment. Since the $\pi^+\pi^-$ system is symmetric, the corresponding Q_L distribution should be centred at 0. Fig. 7.9 shows the experimental distribution of the longitudinal momentum of pion pairs for transverse momenta Q_T<4 MeV/c. The distribution is centred at 0 with a precision of 0.2 MeV/c.

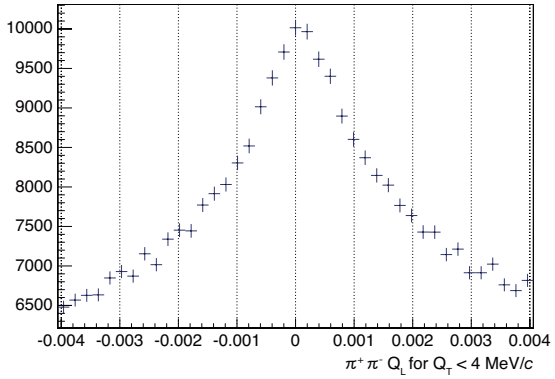

Fig. 7.9 Q_L distribution for $\pi^+\pi^-$ experimental data

7.6 Momentum resolution

The resolution of the laboratory momentum is obtained with simulated Λ particles, taking into account the momentum smearing (see section **7.5**) and using the equation:

$$\frac{\Delta p}{p} = \frac{p_{gen} - p_{rec}^{smeared}}{p_{gen}}, \qquad (6)$$

where p_{gen} and $p_{rec}^{smeared}$ are the generated and reconstructed (smeared with $j = 7$) laboratory momenta of particle, respectively.

The MC distributions of $\Delta p/p$ are fitted with a Gaussian for different momentum ranges and different particles. The σ parameter of normal distribution is shown in Fig. 7.10, giving accurately the laboratory momentum resolution. It is seen that the spectrometer is able to reconstruct momentum with a relative precision between 2.8×10^{-3} and 4.4×10^{-3} for particles with momenta between 1.5 and 8 GeV/c.

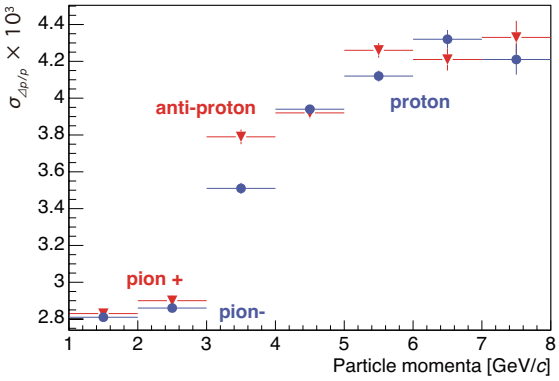

Fig. 7.10 Laboratory momentum resolution as function of particle momentum

The resolution of the projections of the relative momentum Q components has been obtained with simulated πK events, comparing generated and reconstructed values of Q projections. The dependences of the setup resolution of Q_X, Q_Y and Q_L on pair momentum for πK pairs are presented in Fig. 7.11.

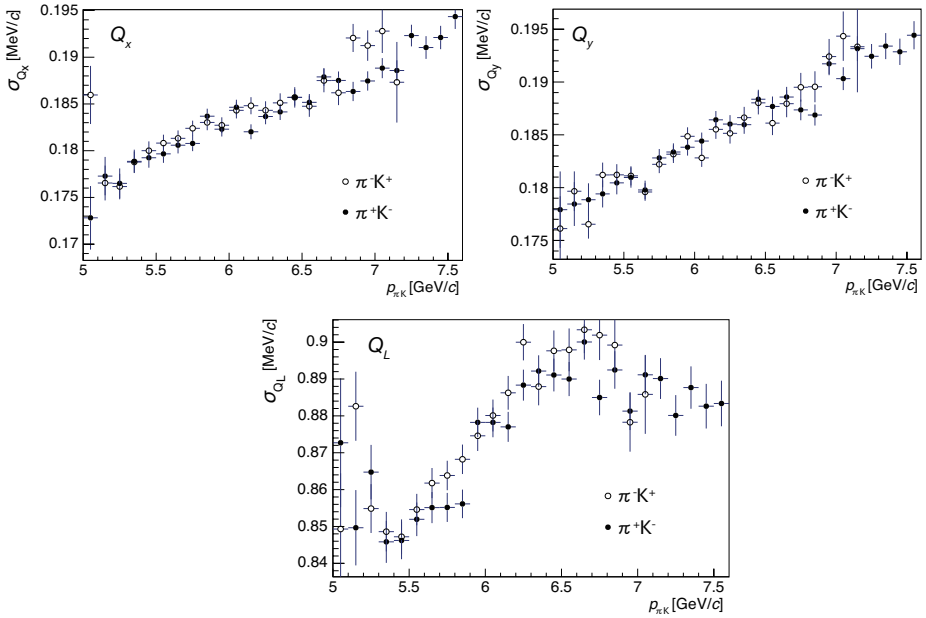

Fig. 7.11 Q_x, Q_y and Q_L resolution of the transverse momentum for π^-K^+ events (open) and π^+K^- events (black)

For Q_L projection, the resolution is determined by the resolution of upstream and downstream coordinate detectors, multiple scattering in IH (ionisation hodoscope), mylar membrane before magnet, aluminum membrane after magnet, surrounding air and DC (drift chambers). Achieved resolution of $\sigma_{Q_L} = 0.85 \sim 0.90$ MeV/c (Fig. 7.11) is at the level of Bohr momentum of πK atoms.

The main contribution to the uncertainty of Q_T measurement is the multiple scattering in the target, which provides an error of the order of 0.8 MeV/c. The resolution of the setup is determined by the resolution of the opening angle of the pair measured with the upstream coordinate detectors, the multiple scattering in the mylar membrane after the target, in the MDC detector, in the SFD detector and in the surrounding air. This resolution is designed to be sufficiently good so as not to seriously increase the error induced by multiple scattering in the target. The values achieved of $\sigma_{Q_x} = 0.17 \sim 0.20$ MeV/c and $\sigma_{Q_y} = 0.17 \sim 0.20$ MeV/c fulfil this requirement.

For this experiment it is needed to know the resolution of the setup on the relative momentum components with a high accuracy, because the difference of smearing between experimental and simulated distributions would lead to biases of the estimated parameters. The influence of the different effects to the measured value of the breakup probability have been investigated in [YAZ13]. The systematic errors induced by the imperfection of the description of the setup are collected in table 7.1. Analysis has been done for one-dimensional distribution of events in Q_L and for two-dimensional distribution of events in (Q_L,Q_T), which have different sensitivities to different sources of systematic errors.

Table 7.1 Estimation of systematic errors induced by different sources for all data collected in 2008-2010

Sources of systematic errors	$\sigma^{syst}_{Q_L Q_T}$	$\sigma^{syst}_{Q_L}$
Uncertainty of correction on Λ-width	0.0039	0.0071
Uncertainty of multiple scattering in the Nickel target	0.0032	0.00054
Accuracy of SFD detector response simulation	0.00075	0.00029
Correction of Coulomb correlation function on finite size of production region	0.000058	0.000058
Uncertainty in a dependence $P_{br}(\tau)$ on the life time	0.0050	0.0050
Accuracy of the target thickness measurement	0.00030	< 0.00030

The size of the systematic errors induced by the setup description is small and allows performing the measurement of πK atom lifetime with the expected accuracy.

8. Conclusion

An upgrade of the DIRAC spectrometer has been carried out in order to measure the life-time of $K^{\pm}\pi^{\mp}$ atoms, and at the same time to identify a long-lived excited state of $\pi^+\pi^-$ atoms, in addition to the on-going measurement of the life-time of $\pi^+\pi^-$ atoms. This resulted in a success of first measurement of the life time of πK atoms, and as for the life time of $\pi^+\pi^-$ atoms, an improvement of the statistical uncertainty from 3.1% to 2.2%, and the total uncertainty including systematic errors from 4.3% to 3.0%.

SFD and IH are the keys as front-end detectors that work in the strong intensity beam such as 2×10^{11}/s. SFD made it possible to identify particle pairs originating from atoms and determined their relative momenta with its high spatial resolution comparable to that of chambers. The short-comings of SFD which sees two particles as one when they are very close, was backed up by IH with its capacity of separating a passage of one and two charged particles.

Large number of background particles have been eliminated with well-performing backward detectors namely Aerogel, C4F10, and N_2 Cerenkov counters, and Preshower, Muon detectors. An excellent time resolution of VH together with good time resolution of the front-end detectors also acted to reduce strongly the background.

DCs with their very high spatial resolution, and the carefully-mapped spectrometer magnet allowed to measure the momenta of the charged particles with a high precision, helped by a strongly reduced mass of the front-end detectors. The lambda decay width used as a monitor of the spectrometer performance allowed to measure it to the world record level.

Newly developed F1-TDC-ADC modules have been used in the readout of most of the detectors, which allowed to record both the timing and the pulse-height of each hit simultaneously, allowed a high-precision measurement and efficient background rejection.

A key-point in the identification of the pairs originated from hadronic atoms is how well one can separate them from the competing processes which end up in producing the same kind of particles. The main signature of the atomic pairs is their small relative momenta in comparison to all other processes. In making the clean separation, the capacity of the spectrometer of measuring it with reduced error was one point, but also the simulation study of the spectrometer to reproduce the distributions of all the competing processes was another important point. The high-quality measurement became possible with a performance of the new spectrometer and with a meticulous offline analysis.

It should be noted that this setup as a spectrometer has a large acceptance in the momentum of exotic atoms from 2 to 9 GeV/c. Although DIRAC experiment was performed using a beam of 24 GeV/c at the CERN PS, this spectrometer can be installed in an accelerator of higher energy, where the atom's production cross section is larger.

Acknowledgments

We are indebted to the CERN PS crew for providing a beam of excellent quality. Some of us acknowledge support from ETC$*$, Trento. This work was supported by CERN, the Grant Agency of the Czech Republic, grant No. 202/01/0779, the Istituto Nazionale di Fisica Nucleare (Italy), the Japan Society for the Promotion of Science (JSPS), Grant-in-Aid for Scientific Research No. 07454056, 08044098, 09640376, 11440082, 11694099, 12440069, 14340079, 15340205, 20340059 and 24340058, the Ministry of Education and

Research (Romania), contract Nr.5/2012 CAPACITATI M.III, JINR Dubna, contract No. 08626319/ 96682-72, the Ministery of Industry, Science and Technologies of the Russian Federation and the Russian Foundation for Basic Research (Russia), under project 01-02-17756, the Swiss National Science Foundation, the Ministerio de Economía y Competitividad (MinEco), and the Xunta de Galicia (Spain).

References

[ACA01] TDC-F1. High-performance 8 channel TDC. www.acam.de ACAM publication, 2001.

[ADE03A] B. Adeva et al., Lifetime measurement of $\pi^+\pi^-$ and $\pi^{\pm}K^{\mp}$ atoms to test low energy QCD, Addendum to the DIRAC Proposal, CERN-SPSC-2004-009, SPSC-P-284 Add. 4, 21 April 2004

[ADE03B] B. Adeva et al., DIRAC: A high resolution spectrometer for pionium detection, Nucl. Instr. Meth. A515 (2003) 467

[ADE04] B. Adeva et al., Detection of ππ atoms with the DIRAC spectrometer at CERN, J. Phys. G: Nucl. Part. Phys. **30** (2004) 1929-1946.

[ADE11] B. Adeva et al., Determination of ππ scattering lengths from measurement of $\pi^+\pi^-$ atom lifetime, Physics Letters **B704** (2011) 24–29

[ADE14] B. Adeva et al., First piK atom lifetime and piK scattering length measurements, Physics Letters **B735** (2014) 288-294

[AFA02A] L. Afanasyev, et al., Nucl. Instr. and Meth. **A491** (2002) 376

[AFA02B] L. Afanasyev and V. Karpukhin, Drift chamber readout system of the DIRAC experiment, Nucl. Instr. and Meth. **A492** (2002) 351 – 355

[AFA96] L. Afanasyev and A. Tarasov, Phys. At. Nucl. **59** (1996) 2130

[ALL07A] Y. Allkofer, A. Benelli and L. Tauscher, Tracking in DIRAC using only downstream detectors, DIRAC-NOTE-2007-08 (2007)

[ALL07B] Y. Allkofer, A. Benelli and L. Tauscher, Angular resolution and multiple scattering in downstream tracking, DIRAC-NOTE-2007-09 (2007)

[BEN08] A. Benelli, SFD study and simulation for the data 2008-2010, DIRAC Collaboration meeting, 26 September 2011, Geneva, Switzerland, http://dirac.web.cern.ch/DIRAC/talk/talk1101.pdf

[BEN11] A. Benelli, SFD study and simulation for the data 2008-2010, DIRAC Collaboration meeting, 26 September 2011, Geneva, Switzerland, DIRAC-TALK-2011-01

[BEN12] A. Benelli and V. Yazkov, Multiple scattering studies, DIRAC-NOTE-2012-04, http://cds.cern.ch/record/1475780

[BEN13] A. Benelli and V.Yazkov, Setup tuning using Lambda and anti-Lambda particles, DIRAC-NOTE-2013-03, http://cds.cern.ch/record/1622175

[BER12] J. Beringer et al. (Particle Data Group), The Review of Particle Physics Phys. Rev. D **86**, 010001 (2012)

[BIT04] G. Bitsadze, V. Brekhovskikh, A. Kuptsov, V. Lapshin, V. Rykalin, L. Tauscher and M. Zhabitsky, The ionization hodoscope of the DIRAC experiment, Nucl. Instr. Meth. **A533** (2004) 353

[BRA99] M. Bragadireanu et al., A prototype Cerenkov counter for DIRAC, Nucl. Instr. Meth. **426** (1999) 254

[BRE08A] V. Brekhovskikh, A. Kuptsov, J. Martincik, T. Trojek, Test with a laser of C4F10 Cherenkov detectors, DIRAC-NOTE-2008-02

[BRE08B] V. Brekhovskikh, A. Kuptsov, V. Rykalin, Updating the DIRAC muon identification system, DIRAC-NOTE-2008-08

[DUD05] A. Dudarev, V. Kruglov, L. Kruglova, M. Nikitin, Pion multiple Coulomb scattering in the DIRAC experiment, DIRAC-NOTE-2005-02

[DUD08] A. Dudarev et al., Pion multiple Coulomb scattering in the DIRAC experiment (updated version), DIRAC-NOTE-2008-06, http://cds.cern.ch/record/1369639

[DUD09] A.V. Dudarev, V.V. Kruglov, M.V. Nikitin, Micro-Drift Chamber as a precise vertex detector for the DIRAC experiment, Nucl. Instr. Meth. **A607** (2009) 394

[GOR00] A. Gorin, M. Kobayashi , K. Kuroda, A. Kuznetsov, I. Manuilov , K. Okada , A. Riazantsev, A. Sidorov and F. Takeutchi, Peak-sensing discriminator for multichannel detectors with cross-talk, Nucl. Instr. Meth. in Phys. Res. **A452** (2000) 280-288
[GOR05] O. Gortchakov, The implementation of new multiple scattering procedure into GEANT-DIRAC, DIRAC-NOTE-2005-20, http://cds.cern.ch/record/1369671
[GOR06] A. Gorin et al., High resolution scintillating-fibre hodoscope and its readout using Peak-sensing algorithm, Nucl. Instr. Meth. in Phys. Res. **A566** (2006) 500-515
[GOR07] O. Gortchakov, On multiple scattering simulation in the GEANT-DIRAC, DIRAC-NOTE-2007-04, http://cds.cern.ch/record/1369657; Y. Allkofer, A. Benelli, L. Tauscher, Angular resolution and multiple scattering in 'downstream' tracking, http://cds.cern.ch/record/1369652
[GOR09] O. Gortchakov, The alignment of DIRAC setup for year 2008 using the properties of Lambda peak and ΔX coordinate at the target distributions, DIRAC-NOTE-2009-10, http://cds.cern.ch/record/1369625; O. Gortchakov, The new results on the Lambda peak width and ΔX coordinates at the target for 2002 year and comparison with MC results, DIRAC-NOTE-2009-08, http://cds.cern.ch/record/1369627; O. Gortchakov, The new results on the Lambda peak width for data samples at different years and comparison with MC results, DIRAC-NOTE-2009-02, http://cds.cern.ch/record/1369633; O. Gortchakov, The Lambda peak width for data samples at different years, comparison with MC results, DIRAC-NOTE-2008-09, http://cds.cern.ch/record/1369636; B. Adeva, A. Romero, O. Vazquez Doce, Study of multiple scattering in upstream detectors in DIRAC, DIRAC-NOTE-2005-16, http://cds.cern.ch/record/1369675
[GOR10] O. Gortchakov, The momentum distribution of $K^+\pi^-$ and π^+K^- pairs (Coulomb and nonCoulomb), DIRAC-NOTE-2010-01, http://cds.cern.ch/record/1369624
[HOR08] S. Horikawa, Y. Allkofer, C. Amsler, V. Brekhovskikh, A. Kuptsov, M. Pentia, M. Zhabitsky, C4F10 cherenkov detector for DIRAC-II, Nucl. Instr. Meth. **A595** (2008) 212
[JED11] F. Jediny, J. Smolik and V. Yazkov, Efficiency of the horizontal hodoscope, DIRAC-NOTE-2011-01
[KAR03] V. Karpukhin, A. Kulikov, V. Olshevsky, and S. Trusov. Readout logic and its hardware implementation in the dirac experiment. Nucl. Instr. Meth. **A512** (2003), 578–584
[KUP08] A. Kuptsov, Design of C4F10 Cherenkov detectors, DIRAC-NOTE-2008-01
[KUP09] A. Kuptsov, DIRAC setup, DIRAC-NOTE-2009-06
[KUR96] I. A. Kurochkin, Preliminary calculations of neutron background in the DIRAC experiment, DIRAC-NOTE-1996-07
[LEC--] Model 3377, 32 channel TDC, operator manual. LeCroy corporation
[PEN09] M. Pentia, C. Ciocarlan, S. Constantinescu, M. Gugiu, G. Caragheorgheopol, Preshower detector for $\pi^+\pi^-$ hadronic atom studies, Nucl. Instrum. Meth. **A603** (2009) 309-318
[PEN11] M.Pentia, S.Constantinescu, M.Gugiu, The new preshower detector for DIRAC-II setup: characteristics and performances, DIRAC-NOTE-2011-03 (2011)
[VOR12] A. Vorozhtsov, Permanent magnet dipole for DIRAC, DIRAC-NOTE-2012-02
[YAZ13] V. Yazkov and M. Zhabitsky, Investigation of systematic errors and estimation of πK atom lifetime, DIRAC-NOTE-2013-06, http://cds.cern.ch/record/1628544
[ZHA08] M. Zhabitsky, Direct calculation of the probability of pionium ionization in the target, Phys. At. Nucl. **71** (2008) 1040 [hep-ph/0710.4416]